University of Trento
University of Brescia
University of Padova
University of Trieste
University of Udine
University IUAV of Venezia

Ph.D. Candidate
Fabrizio Zendri

DEVELOPMENT OF A RESEARCH VEHICLE ABLE TO PERFORM AUTONOMOUS MANOEUVRES

Advisor
Prof. F. Biral

2010

UNIVERSITY OF TRENTO
Graduate School in Structural Engineering
Modelling, Preservation and Controls of Materials and Structures
XXII Cycle

Ph.D. Program Head: prof. D. Bigoni

Final Examination: 19 April 2010

Board of Examiners:
Prof. Mauro Da Lio, Università di Trento
Prof. Alain Molinari, Universitè Paul Verlaine - Metz
Prof. Rosario Ceravolo, Politecnico di Torino

Summary

Autonomous driving is an important research field and presents several problems with different nature and complexity. The goal of this work is describing such problems and the concerning solutions adopted while developing an experimental vehicle designed to autonomously perform some manoeuvres and/or to be remotely driven: the vehicle RUMBy.

The problem has been faced from its beginning, *i.e.* from the hardware and software design: the requisites the system should satisfy are discussed, such as the vehicle and the sensors chosen, and the adopted hardware and software architectures are then described. Some mathematical models representing the vehicle dynamics are also presented, that have been employed in several applications, from the dynamic behaviour simulation up to the control system synthesis. Each model besides presents characteristic parameters that should be evaluated: therefore the problem of identification is discussed in detail, accompanied by the results obtained during an experimental activity carried out in collaboration with a Japanese research institute. Also the vehicle state estimation constitutes a key point in autonomous driving field: about this, the experimental results yielded by an estimation algorithm, based on a Kalman filter, are presented and discussed. Finally, the yaw rate control problem is examined, which is fundamental for both the motion stabilization (during remote driving) and for the following of yaw rate reference profiles (while performing autonomous manoeuvres). Two control architectures, based on a disturbance observer, have been developed and compared in a simulation campaign, that has been carried out by means of a static simulator which reproduces the driving of RUMBy in a virtual environment.

This work aims then at marking a milestone within a work in progress, as well as at representing a potential guideline for researchers that would coping with projects concerning autonomous driving.

Sommario

La guida autonoma costituisce un importante campo di ricerca e presenta numerose problematiche, di differente natura e complessità. L'obiettivo di questo lavoro è descrivere tali problematiche, e le relative soluzioni adottate durante lo sviluppo di un veicolo sperimentale progettato per svolgere autonomamente delle manovre e/o essere guidato in remoto: il veicolo RUMBy.

Il problema è stato affrontato dall'inizio, cioè dalla progettazione hardware e software del veicolo: sono discussi i requisiti che il sistema doveva soddisfare, il veicolo e i sensori scelti e sono quindi descritte le architetture hardware e software progettate. Sono inoltre presentati alcuni modelli matematici rappresentativi della dinamica del veicolo, che hanno trovato impiego in varie applicazioni, dalla simulazione della dinamica del veicolo alla sintesi del controllo. Ogni modello è tuttavia caratterizzato da parametri di cui è indispensabile conoscere il valore: il problema dell'identificazione è quindi discusso in dettaglio, accompagnato dai risultati di un'attività sperimentale svolta in collaborazione con un istituto di ricerca giapponese. Anche la stima dello stato del veicolo costituisce un punto chiave nella guida autonoma: a tal proposito sono riportati i risultati sperimentali ottenuti mediante un algoritmo di stima basato su un filtro di Kalman. Infine è affrontato il problema del controllo della velocità di imbardata, fondamentale sia per la stabilizzazione del moto (durante la guida in remoto) che per l'inseguimento di profili di velocità di imbardata di riferimento (nell'esecuzione di manovre autonome). Due architetture di controllo, basate su un osservatore del disturbo, sono state progettate e confrontate durante una campagna di simulazione, svolta mediante un simulatore statico che riproduce la guida di RUMBy in ambiente virtuale.

Questa tesi ambisce quindi a costituire una pietra miliare all'interno di un lavoro tuttora in corso, nonchè a rappresentare una possibile linea guida per quanti volessero affrontare un progetto inerente la guida autonoma.

A Martina

Acknowledgements

I gratefully thank all the people who helped me directly or indirectly in the last three years. In particular, my thank to Francesco Biral for being my advisor and giving me the opportunity to face this challenge.
I am grateful to all members of the Mechatronics Research Group of the University of Trento and of the Fujimoto's Laboratory of the Yokohama National University, comprising professors, researchers and students.
Finally, I am especially indebted to all my family and, above all, to my mother Rosanna. Thank you.

Trento, April 2010

Fabrizio Zendri

Published papers

The main results presented in this thesis have been summarized in the following papers:

1) Bertolazzi, E., Biral, F., Bosetti, P., De Cecco, M., Oboe, R. and Zendri, F. (2008) Development of a Reduced Size Unmanned Car. In proceedings of AMC '08. 10th IEEE International Workshop. Trento, Italy - March 2008.

2) Bortoluzzi, D., Biral, F., Bertolazzi, E., Bosetti, P. and Zendri, F. (2008). Influence of Vehicle Model Complexity in Autonomous Emergency Manoeuvre Planning. Proceedings of IMECE 2008, 2008 ASME International Mechanical Engineering Congress and Exposition. Boston, Massachusetts, USA - November 2008.

3) Zendri, F. and Biral, F. (2009). Influence of Vehicle Dynamic Models on Stability Control Startegy Development. MULTIBODY DYNAMICS 2009, ECCOMAS Thematic Conference. Warsaw, Polland - June 2009.

4) Zendri, F., Antonello, R., Biral, F. and Fujimoto, H. (2009). Modeling, identification and validation of an Electric Vehicle for model-based control design. To be published on the Proc. of the Advanced Motion Control, 2010. AMC '10. 11th IEEE International Workshop. Nagaoka, Japan - March 2010.

Contents

Chapter 1

Introduction

1.1 Background and Motivation

Autonomous driving is a very active research field, both in universities and laboratories, and also competitions have been performed: the most famous one is the DARPA (Defense Advanced Research Projects Agency) Challenge, launched by the US Department of Defense in 2003 to spur innovation in unmanned ground vehicle navigation (Thrun et al., 2006). Autonomous vehicles find employment in situations that are dangerous and hazardous to humans, as in toxic environments, in mining industry and in military operations (Schmidt and Freyberg , 1996, Roberts et al., 2002). Recently, intelligent service robots are becoming popular to assist people in daily tasks (*e.g.* hospital services, museums, shops, etc.), and the cost decline of computers and electronic systems is allowing the commercialization on large scale of autonomous vehicles in agriculture and other industries. Moreover vehicle automation concerns the development of driving assistance systems oriented at increasing the driving safety supporting the driver in critical situations; examples about that kind of employment are the Adaptive Cruise Control (ACC) (Bengtsson , 2001), the Frontal Collision Warning (FCW) (Vahidi and Eskandarian , 2003), the Intelligent Speed Adaptation (ISA) systems (Carsten and Tate , 2005) and, recently, the SASPENCE (SAfe SPEed and safe distaNCE) system (Saroldi , 2008).

The Mechatronics Research Group of the University of Trento has been involved in autonomous driving projects for a decade. In particular, the path planning algorithm present in the SASPENCE system exploits the Optimal

Manoeuvre Method (OMM[1]) developed in Trento (Bertolazzi et al., 2005, Bertolazzi et al., 2006, Bertolazzi et al., 2007). The experience gained on the field has highlighted a gap in previous autonomous/assisted driving studies. In DARPA's full-autonomous systems, large-sized vehicles are used, with expensive sensors and hardware (investments on the order of M$) and without any kind of human interaction. Moreover remote-control driving is only in supervision-mode, *i.e.* giving some finite state macro-instructions to the robot. On the contrary, European research projects (like SASPENCE and others) have human-in-the-loop architectures, but they cover just an informative role and do not execute autonomous manoeuvres. The cited researches have radical approaches to the vehicle-human interaction, and suggested an innovative method. The basic idea is to exploit the possible "optimal manoeuvres" and the commands applied by the driver in order to interpret his intention/purpose. Once such an intention is known, the system can act in two ways:

- leave the driving task to the driver,
- semi- or full-autonomously execute the optimal manoeuvre, if the driver intention is held as dangerous.

The first version of such a kind of system could be for instance an intelligent stability program, that estimates the forward road geometry, plans an optimal manoeuvre that maximises a safety criteria and exploits such a manoeuvre to apply a correction to the driver's actions.

These researches on autonomous driving have consequently disclosed the need of an experimental platform for the verification of the proposed algorithms. The Reduced-size UnManned Buggy (RUMBy) Project has then been started in 2006, aiming at produce an experimental platform that allows to check the efficiency of path planning algorithms, sensor fusion systems and control strategies. In other words, the goal of the RUMBy project was the creation of an experimental vehicle able to autonomously perform some specific manoeuvres. Moreover, in parallel to the RUMBy Project, the need of an intensive multibody analysis of the vehicle has shown itself. Both for the construction of a vehicle static simulator and for the synthesis of control algorithms, vehicle mathematical models are necessary. At the same time,

[1]The OMM is based on Optimal Control theory, and can be used to real-time compute the reference manoeuvre of a vehicle based on its state and the information about the surrounding scenario.

multibody representations can be used for path planning and for the study of state estimation algorithms.

The present document collects and discusses the main analysis and results achieved about the above cited topics. In particular, the present work focuses on vehicle modelling, parameter/system identification, state estimation and control algorithm development carried out in range of the RUMBy Project. Part of the work has been done at Fujimoto's Laboratory[2] of the Yokohama National University Japan, since there was available a research vehicle (named "FPEV2-Kanon") equipped with what is necessary for identification and control validation. Experiences done on the full-scale vehicle can be transferred to RUMBy, therefore links with the Japanese experimental activity are also presented.

1.2 Structure of the work

The design, from the beginning, of an autonomous experimental vehicle undoubtedly constitutes a very challenging activity. Many problems of different nature have to be faced, from the choice of the hardware up to the test of the control strategies. Generally speaking, an autonomous vehicle is composed by five main systems (see Fig. 1.1):

1. the vehicle itself, which should be large enough in order to carry the needed equipment and that must provide a by-wire interface to all the driving subsystems (steering, throttle, brakes);

2. the sensors, which have to provide a description of the vehicle state and of the environment as complete as possible;

3. the algorithms for data fusion and state estimation, that have to observe the vehicle state (*e.g.* position, velocity, etc.) at any step time;

4. the algorithms for manoeuvre planning and vehicle control, that have respectively to compute and follow the reference profile of a certain set of variables;

5. the algorithms for scenario reconstruction (road limits, still and dynamic obstacle recognition, etc.) and navigation (that has to decide the best route to be done).

[2] http://www.dnj.ynu.ac.jp/hflab/hfl_e.html

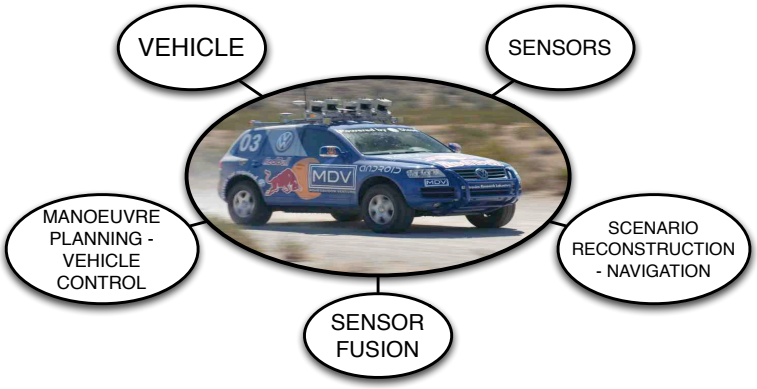

Figure 1.1: Layout of an autonomous vehicle. The five main subsystems constituting an autonomous vehicle are highlighted: four of these subsystems are present on the RUMBy platform, since scenario reconstruction only deals with long-range navigation and has no effect on short-range manoeuvre planning.

As one can expect, the above cited subsystems can be combined in different architectures, even depending on the desired level of automation. Excellent examples of full-automation-oriented architectures can be found in the vehicles that participated to the DARPA Challenge (Thrun et al., 2006, Behringer et al., 2004, Touchton et al., 2006). Even if such vehicles differ on several details, mainly concerning the adopted algorithms, they have a point in common: the whole set of subsystems are combined in a single structure - the vehicle is equipped with a large number of sensors and with computing platforms that carry out the tasks of subsystems 3, 4 and 5. By means of a literature review, other example of this kind of architectures can be found (Albus , 2002), even for aquatic (Kim and Yuh , 2004) or flying vehicles (Frazzoli et al., 2000). Moreover, partial-automation-oriented systems exist, that combine just some of the subsystems of Fig. 1.1. The same driving assistance systems, cited in the previous section, are evident examples of this kind of architecture. Some of them, like the Frontal Collision Warning (Vahidi and Eskandarian , 2003, Svenson et al., 2005), combine together sensors and data fusion algorithm - more or less integrated in the vehicle- to transmit additional information to the driver. Other systems, like the Intelligent Speed Adaptation (Carsten and Tate , 2005) or the well-known Electronic Stability Program (Liebermann , 2004), even incorporate simple control algorithm to aid the driver in critical conditions.

With the sole exception of the last subsystem, which only deals with long-range navigation and which has no effect on short-range manoeuvre planning, all the subsystems 1-4 are present on the RUMBy platform and have been developed following a modularity approach.

More specifically, it can be said that subsystems 1 and 2 constitute the hardware part of the vehicle. Designing the architecture of this kind of systems constitutes itself a remarkably complex task: it is necessary to define project requirements, to choose the on-board sensors, to define hardware and software interfaces, to devise the software framework and so on. This phase of RUMBy Project has required strong efforts and has witnessed several reviews: while the project gone on, different problems have been met that have forced the definition of new hardware and software requirements and new designs. The resulting RUMBy Project architecture is discussed in Chapter 2. Moreover, since some of the proposed studies are referred to the Japanese activity, a brief description of the vehicle Kanon is given in § 2.2.

Subsystems 3 and 4 constitute instead the software part of the project, and require additional comments. Either for the state estimation and the out-and-out control of the vehicle, it becomes necessary to produce mathematical models that describe the system evolution and this justifies the structure of the work. Chapter 3 describes indeed the main mathematical models describing the vehicle dynamics and its mechanical subsystems. Nevertheless, in order that a model efficiently represents a system, it is necessary to measure or estimate the parameters that characterize the system (*e.g.* inertial and geometrical parameters, friction coefficients, etc.). The set of activities oriented at measuring/estimating such parameters is termed "identification", and constitutes the topic of Chapter 4. Once efficient mathematical models are at disposal, they can be exploited for the creation of state estimation and control algorithms. Both these topics constitute extremely active and wide research fields and have required a long and intensive analysis. In detail, Chapter 5 describes the state estimation architecture developed for RUMBy: it will be shown that a modularity approach has been chosen even for this system, with notable advantages both in terms of efficiency and flexibility. Finally, the last subsystem -control algorithms- is discussed in Chapter 6. The vastness of this topic is immediately evident from literature review: various approaches and architectures can be adopted, depending also on the variable to control. More specifically, two approaches for the yaw rate control are discussed in Chapter 6, comprising a comparison activity carried out by means of a purpose-made static driving simulator and oriented at evaluate the effect

of controllers on disturbance rejection and vehicle manoeuvrability.

Chapter 2

Experimental Vehicles and Instrumentation

The first two systems composing an autonomous vehicle are the vehicle itself and the sensors. Since the present work is mainly based on the RUMBy project, the chosen vehicle and instrumentation are described, focusing on the requisites that were used for their selection. Moreover the software architecture is presented, because it is an integral part of the autonomous vehicle. Anyway, a second vehicle belonging to an external institute has been used for some of the activities discussed in Chapter 4. Even if its design is not part of the present work, a brief description of its main characteristics is given at the end of the chapter to ease the explanation of the identification activity.

As explained in the introducing chapter, a project concerning autonomous driving involves a large number of complex activities. The most complex one is probably the outline of the structure of the system, comprising the selection of the hardware (*i.e.* the vehicle, the sensor, the instrumentation, etc.) and the development of the software. The availability of a well-designed system makes all the other activities easier.

Since the present work is mainly based on the RUMBy project, this chapter is focused on the description of the adopted vehicle and instrumentation. At the beginning of the project a strong effort has been made to define a set of requisites that the vehicle and the instrumentation should satisfy. The following pages give then an accurate explanation of the whole set of activities dealing with the definition of the project requirements and the choice of the RUMBy hardware. Moreover the RUMBy's software architecture is presented

and discussed, since it represents a fundamental part of the system. A set of requirements has been defined also for the software, thus a section of the present chapter is dedicated to explain the chosen solution.

Anyway RUMBy is not the only vehicle involved in the research described in this work. Some of the activities discussed in Chapter 4 have been indeed conduced with a second vehicle: the "FPEV2-Kanon". The Mechatronics Research Group has started a collaboration with the Fujimoto's Laboratory of the Yokohama National University (Japan), that disposes of an electric vehicle named "FPEV2-Kanon". In range of such a collaboration, an identification and validation work of a model of Kanon has brought to very interesting results, presented in § 4.1.2 and 4.2. Obviously the design of Kanon is not part of the present work, and its architecture can not be explained as well as the RUMBy's one. Nevertheless a brief description of the vehicle and its instrumentation is given in the last section of this chapter.

2.1 RUMBy

In the last years the Mechatronics Research Group has been involved in several projects concerning autonomous and assisted driving (Bertolazzi et al., 2008b). In particular, a strong effort has been made to develop the Optimal Manoeuvre Method (Bertolazzi et al., 2005, Bertolazzi et al., 2006), which uses the Optimal Control theory to compute the reference manoeuvre a vehicle should follow to achieve a certain purpose (*e.g.* minimum time, maximum safety, etc.). The experience gained in the automotive field has highlighted a gap in previous researches on autonomous driving, concerning the concept of "collaboration" between vehicle and driver. It has been indeed seen that an interesting investigation field could focus on intelligent driving assistance systems, based on the interpretation of the driver's intention. Such a study has brought to the need of an experimental platform that allowed for test such a king of algorithms. For these reasons a project has been started in 2006 to develop a Reduced-size UnManned BuggY (RUMBy), which is a platform to test the proposed decision and autonomous driving algorithms. The project has been presented for the first time in (Bertolazzi et al., 2008a): this section collects the main results about the whole system architecture (hardware and software).

2.1.1 Hardware: Vehicle and Instrumentation

The hardware part of an autonomous vehicle consists of the vehicle itself and of the instrumentation. About the RUMBy project, the vehicle has been selected on the basis of the following main requisites:

1. **Dynamics:** vehicle dynamics should be similar to real car dynamics.
2. **Representativeness:** attention is paid to on-cars system specifications (use of CAN interfaces).
3. **Safety:** it should be possible to test emergency conditions such as obstacle avoidance or critical scenarios at a low risk level for people and instrumentation.
4. **Flexibility:** the system should be cheap, rapid prototyping oriented, and with less constraints w.r.t. real cars.
5. **Scalability:** it should be easy to investigate co-operative and platooning technologies, coupling the vehicle with other platforms.
6. **Lightness:** compact and low power consumption systems are preferred.

Consequently, a radio-controlled (R/C), 1:6 scale model of H2 Hummer has been chosen as experimental platform (see Fig. 2.1). The chosen solution conforms with all the requirements, especially with requirements 1, 4, 5 and 6.

The vehicle is 680 mm long and 510 mm wide and is equipped with a 26 cm^3 two-strokes engine and 4 disk brakes. The power train is connected to the engine through a centrifugal clutch. The vehicle model has been customized with stiffer shock absorbers and with an aluminium frame, in order to mount on the necessary on-board instrumentation. Anyway, due to the limited load capacity of the vehicle, only the sensing and the sensor fusion instrumentation have been installed on-board. The heavy and energy-consuming computer needed for the control and actuation, and for the high level automation (system manager and path planning), is instead remotely connected to the vehicle via radio communication channels. This solution also makes it possible to test remote control strategies as explained in the introduction.

The sensing instrumentation has been designed with the target of providing an on-board sensor fusion procedure with the measurement required to reconstruct the whole vehicle state, namely: position, velocity and acceleration vectors, angular positions and velocities, and angular velocity of wheels.

Figure 2.1: The experimental platform RUMBy. The project requirements forced the choice of a radio-controlled, 1:6 scale model of H2 Hummer, equipped with a 26 cm^3 two-strokes engine, centrifugal clutch and 4 disk brakes. The vehicle has been customized with an aluminium frame, in order to mount on the sensors, the PC104 embedded computer and the wireless router.

The sensor fusion system runs on an on-board PC104[1] embedded computer and collects measurement data from the following devices:

1. a differential Global Positioning System (GPS) receiver running at 20-100 Hz (Racelogic VBox III), connected via CAN to PC104;

2. an Attitude and Heading Reference System (AHRS) providing 3 accelerometers, 3 gyroscopes and 3 magnetometers (MicroStrain 3DM-GX1), connected via serial port to PC104;

3. two rear-wheel speed sensors (odometers) based on Hall-effect sensors, custom designed and manufactured, connected via serial port to PC104.

Both the raw measurements and the fused data that describe the vehicle state are sent to the manager computer via a custom UDP protocol by means

[1]PC104 is an embedded computer standard controlled by the PC/104 Consortium, which defines both a form factor and computer bus (http://www.pc104.org/).

of a Linksys 802.11n wireless router (effective line-of-sight range exceeding 150 m). Regarding the actuation part, the throttle and steering servomotors can be driven manually (by means of a standard R/C joystick) or can be switched in closed loop control (for autonomous drive). Moreover, also intermediate solution are possible such as "intelligently" correct the operator commands with additional optimal feedback or feedforward signals. An Arduino[2] programmable microcontroller, that is in serial communication with the PC104, takes care of the mode switching, which can be toggled either by pushing a button on R/C joystick or by way of the on-board PC104. In case of autonomous drive mode, the steering and throttle commands are routed by the manager computer through the PC104 and through the microcontroller to the servomotors.

With the adopted architecture the PC104 has a direct access -through the microcontroller- to the servos. This allows the investigation of on-board control techniques and emergency-management manoeuvres. Moreover, an immediate mode-switching function can be easily implemented, which could be helpful in testing driver assistance algorithms and makes the solution suitable for testing advanced configurations. The resulting architecture is schematised in Fig. 2.2, which shows the on-board sensing devices on the top and the base station (path-planning dedicated PC and R/C joystick) on the bottom.

2.1.2 Software Architecture

As for the choice of the hardware, also the software architecture should satisfy some requisites, that are:

1. **Safety:** emergency manoeuvre must always be available.
2. **Modularity:** functions available as black boxes with flexible interfaces.
3. **Concurrency:** re-configurability and parallelization.
4. **Neutrality:** interoperability of different softwares, programming languages and pre-existing packages.

Dealing with autonomous vehicles means continuously prevent and avoid potential crashes, and this is the reason why safety is the first and most important requirement. The other main requisites -which are almost self explaining-

[2]Arduino is an open-source electronics prototyping platform based on flexible, easy-to-use hardware and software (http://www.arduino.cc/).

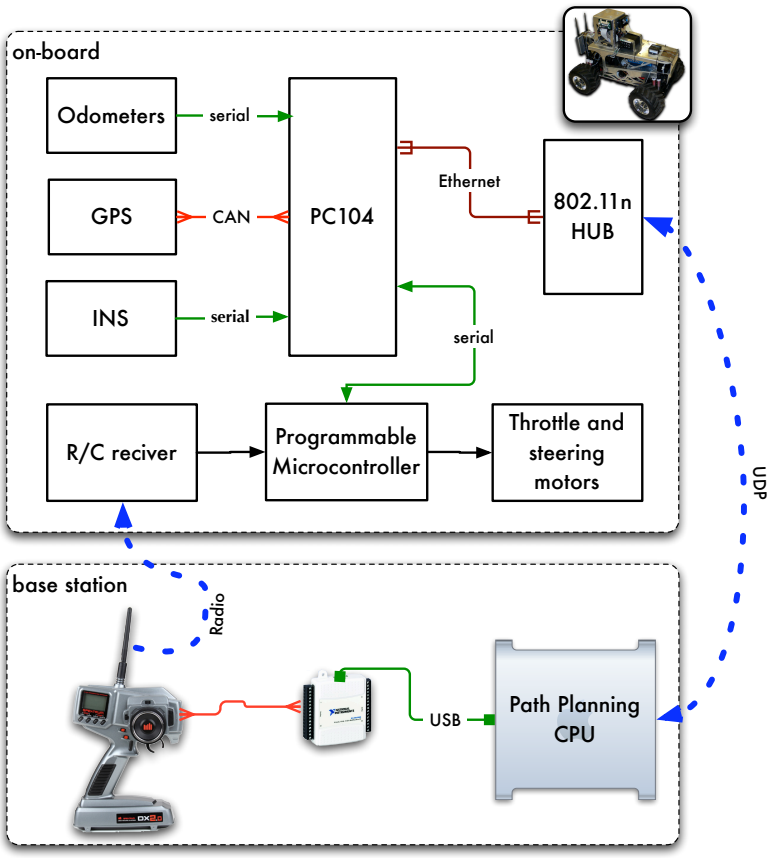

Figure 2.2: System Architecture. Because of the limited load capacity, the heavy and energy-consuming computer for the path planning (manager) is remotely connected via radio-communication channels. The architecture is thus split in two main parts: on-board instrumentation and base-station.

are of additional relevance if one considers that the software should be easily extendable, especially during the development phase.

As a consequence of the requirement 2, the software has been designed on a multi-process architecture as shown in Fig. 2.3. The main process - **Manager Unit**- is a multi-threaded process that receives commands by a custom graphical user interface (GUI). It holds the manoeuvre planner and the interface with vehicle systems, which, in turn, is made of the driver for the vehicle on-board inertial navigation system (labelled "Telemetry"), the con-

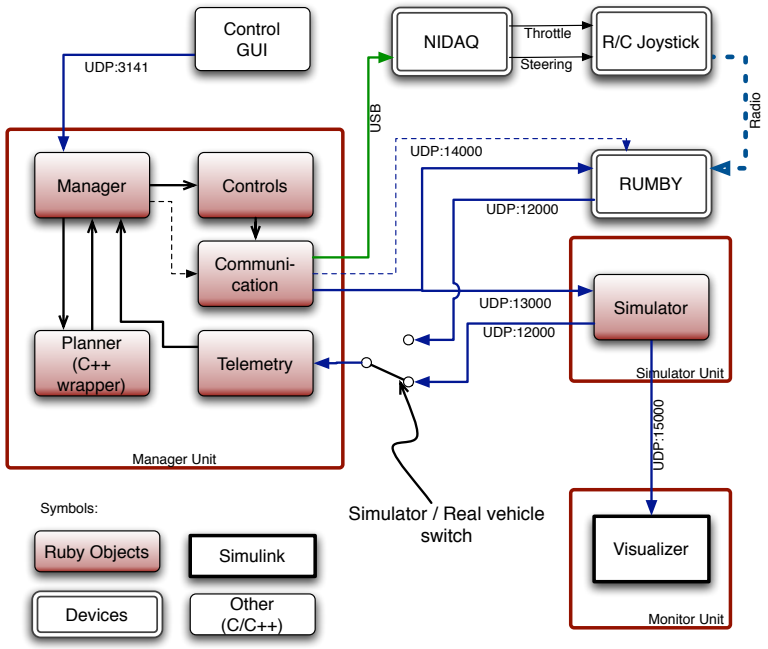

Figure 2.3: Software and hardware architecture with switchable connection between simulator and real vehicle. Dashed lines represent an alternative connection.

trol system (labelled "Controls"), and the commands communication system (labelled "Communication").

The Communication and the Telemetry objects are abstraction layers that provide a neutral, high level access to the vehicle commands and to the vehicle state, respectively. The Planner object is a wrapper for libraries that implement manoeuvre planning, control strategies and so on.

In order to comply with the requirements 2 and 3, the Manager Unit has been implemented as a finite state machine. The state machine runs a main loop with a constant time step. Within this main loop, the state machine can change state either by receiving a command from the GUI or as a consequence of a change in vehicle state variables (*e.g.* trespassing a threshold).

For example, at the beginning the system is in the "idle state" (all commands in neutral state, telemetry enabled). When the GUI sends the command to switch in "accelerate state", the vehicle accelerates at full throttle until it reaches a threshold speed (*e.g.* 1 m/s), then the controller sponta-

neously switches to the "planning state" performing the requested manoeuvre. In planning state, the main loop follows the strategy depicted in Fig. 2.4. It is worth noting that the main loop requests the Planner to interpolate at the present time the latest available planned trajectory. If the error position between planned and actual position exceeds a threshold value, then the planner is requested to compute a new optimal trajectory, which will be used as reference as soon as it will be available. Finally when the distance to the target position is less than the braking distance at the current speed the state machine switches to the "halt state", which disables the planning and performs a full stop of the vehicle.

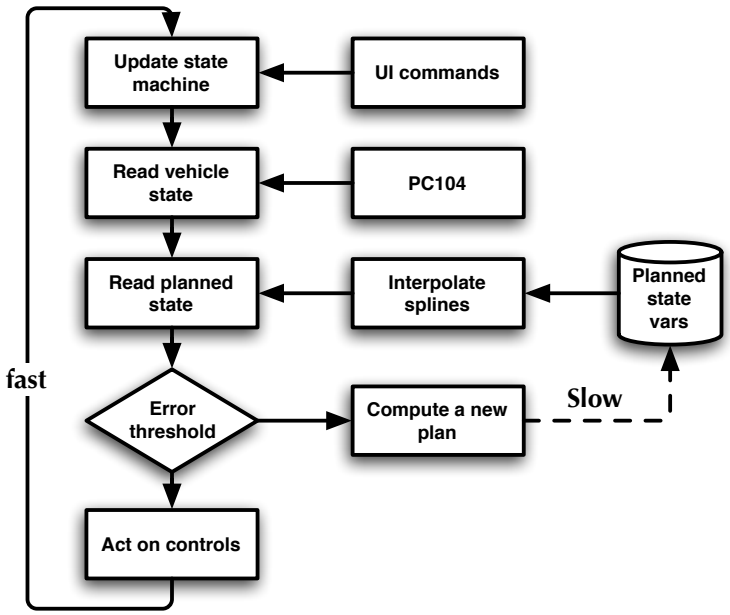

Figure 2.4: Manager Unit main loop flow chart. Once the Manager Unit has assumed a certain state, the actual and desired vehicle states are compared: if the difference is small the system acts to follow the planned state, otherwise a new path is planned and interpolated with the previous one.

It is worth noting that, until the software is correctly tested and calibrated, a direct interface with the vehicle involves some risks. For example, an uncaught software bug or a sudden connection failure could cause the vehicle to become unresponsive and therefore dangerous while travelling at high

velocity. Consequently, in order to comply with the safety requisite, the **Simulator Unit** is introduced, which is a UDP server that listen for throttle and steering commands, updates the state of the vehicle mathematical model it implements, and gives back to the Manager Unit the updated state of the simulated vehicle. Note that the vehicle model implemented within the Simulator Unit is based on the same reference vehicle models described in Chapter 3. Finally, the Simulator Unit can eventually pass the vehicle state information to a remote **Monitor Unit** that shows the vehicle state as a 3-D car in a virtual environment created with the Simulink Virtual Reality toolbox.

Fig. 2.3 makes evident the system modularity (requirement 2). The Manager Unit, in fact, can indifferently drive the real vehicle or the simulated one, and the choice simply requires a switch of IP addresses. Moreover, as already pointed out in Fig. 2.2, the Manager Unit can be alternatively configured in order to calculate control commands and directly act on the vehicle servos (the loop routed through the R/C joystick), or to send references to the on-board PC104, which directly acts on servos (dashed route in Fig. 2.2).

2.2 Kanon

The activities described in this work mainly concern the vehicle RUMBy. Anyway, a second vehicle has been object of some studies: the Future Personal Electric Vehicle "FPEV2-Kanon" shown in Fig. 2.5. Kanon is an experimental electric vehicle, constructed in the Fujimoto's Laboratory of the Department of Electrical and Computer Engineering, Yokohama National University - Japan. In range of a collaboration activity between the Mechatronics Research Group of the University of Trento and the Fujimoto's Laboratory, some research projects are active at the present time. In particular, an identification activity carried out on such a vehicle represents the topic of a recent publication (Zendri et al., 2010). A multibody model of the vehicle has been identified and validated, and such an activity represents also the topic of two sections of the present work (see. § 4.1.2 and 4.2).

Kanon is a single-seater and 4-wheel-steering electric vehicle, fitted with double wishbone suspension struts both at front and rear axles. The vehicle is equipped with outer rotor type in-wheel motors installed in the rear wheels as driving power (maximum torque is ±340Nm per wheel). The steering wheel mechanism adopts Steer-by-Wire and active front and rear steering system, using two 250W DC motors. A Li-ion battery able to charge in a short time is used for the energy storage.

Figure 2.5: Experimental Vehicle "FPEV2-Kanon". The vehicle is property of the Fujimoto's Laboratory of the Yokohama National University - Dept. of Electrical and Computer Engineering.

As well as RUMBy, Kanon is fitted with sensing instrumentation providing the measurement required to re-construct the vehicle state. Sensors installed on-board to measure main kinematic variables are:

- two accelerometers (fixed with the sprung mass), for the measurement of longitudinal and lateral accelerations;
- two gyros (fixed with the sprung mass), for the measurements of roll and yaw rates;
- two encoders, measuring the rear wheels spin rates;
- the optical sensor DATRON CORREVIT S-400, that measures the longitudinal and lateral velocities and the sideslip angle located in front of the vehicle.

Moreover, a dSpace AUTOBOX-DS1103[3] running at 500 Hz is used to log all available sensor signals and to execute real time vehicle control algorithms. Thanks to the large number of available inputs and to the powerful control platform, Kanon represents an extremely useful tool for the development and investigation of vehicle control strategies.

[3]dSpace is an hardware-software platform for development and implementation of control strategies (http://www.dspaceinc.com)

Chapter 3

Vehicle Modelling

A mathematical model of the studied dynamic system represents a powerful tool for several activities, like system behaviour prediction, state estimation and control design. The vehicle is a complex system, with a large number of degrees of freedom and subject to several phenomena and inputs, and the modelling of its dynamics is a challenging activity. Moreover it could be interesting to separately study some of its numerous subsystems, like tyres, suspensions and so on. The present chapter gives a panorama of the most important mathematical models, from the tyre-ground interaction through the whole vehicle dynamics up to its mechanical subsystem.

Both for the state estimation of a dynamic system and for the synthesis and verification of control algorithms, representative mathematical models are necessary. It is indeed mandatory to derive the equations that allow representing and/or predicting the system behaviour.

From a multibody point of view 5 main bodies constitute the vehicle: the sprung mass (passenger compartment, engine and the whole portion of vehicle supported by the suspensions) and the 4 unsprung masses (everyone comprising tyre, wheel, brake and a part of the suspension). Therefore a common vehicle is characterised by 16 Degrees of Freedom (DOF):

- 3 DOF for the sprung mass positions (X, Y, Z),
- 3 DOF for the sprung mass attitude (roll, pitch, yaw - ϕ, θ, ψ),
- 4 DOF representing the struts deflections (l_{rf}, l_{lf}, l_{rr}, l_{lr}),

- 4 DOF for the wheels spinning velocities (ω_{rf}, ω_{lf}, ω_{rr}, ω_{lr}),
- 2 DOF for the front wheels orientations due to the steering system (δ_{rf}, δ_{lf} - usually considered as a single input to the system).

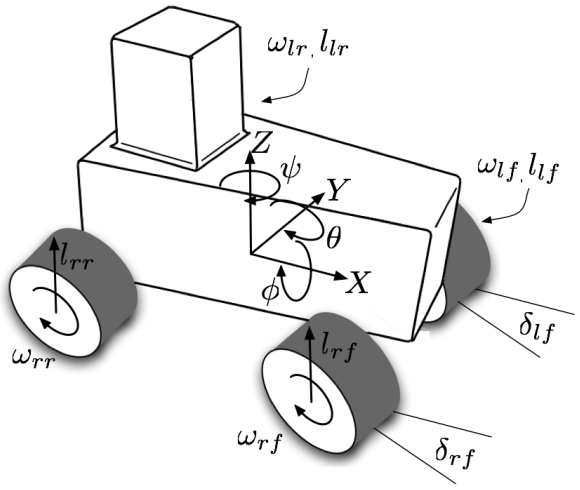

Figure 3.1: Vehicle's Degrees of Freedom. Ordinary vehicles present 16 Degrees of Freedom, that are reduced to 14 because the steering angles are considered as inputs.

Obviously different DOF have different influence on the whole system behaviour and larger is the number of surveyed aspects better the representation is, to the detriment of the understanding simplicity. It is thus allowed, under certain assumptions, to apply simplifications during a specific modelling activity in order to find the best compromise between the mathematical complexity and the representation fidelity.

Moreover it could be advantageous to isolate some subsystems (*e.g.* tyres, suspensions, steering chain, clutch, etc.) and study them separately, in order to consider their contributions on the whole system evolution as black boxes.

The present chapter describes all the most important mathematical models representing the vehicle and its subsystems. It is worth noting that the models should respect the requisites of being real-time integrable, both for simulation and for the development of identification, state estimation and control algorithms. In particular, § 3.1 accurately describes the tyre-ground interaction, from the definition of the tyre slips up to some force models: tyres play the

important role of transmission of the forces between the road and the vehicle, representing thus the most important vehicle subsystem. In § 3.2 three main models describing the whole vehicle are instead discussed. Because of its complexity, the vehicle dynamics can be naturally represented in several ways, depending on the assumed simplification and the contemplated variables and phenomena: three main models, differing on complexity and application, are presented and discussed. Closing, § 3.3 discusses the models created for the analysis of three vehicle subsystems: the suspensions, the steering chain and the power train. In fact these systems can be studied separately, in order to consider their contribution on the whole vehicle dynamics as black boxes.

3.1 Tyre Models

Tyre characteristics are of crucial importance for the dynamic behaviour of the road vehicle: they play the important role of transmission of the forces between the ground and the vehicle itself. The mathematical description of the tyre-ground interaction (in terms of forces) is rather complex and involves many variables: normal load acting at the tyre-ground contact patch, longitudinal and lateral tyre slips, wheel spin about the vertical axis and camber.

The tyre-ground interaction represents a very active research field, with a huge amount of publication. A very accurate description of the problem has been treated in (Pacejka , 2005), in which the author makes a deep analysis of the whole set of included phenomena and of their possible mathematical representations. Based on such a work, several models for the description of the tyres behaviour of both the vehicles RUMBy and Kanon have been developed.

As introduced, every variable has a specific effect on the phenomenon. Consequently some simplifications have been assumed, in order to clarify the problem and make the models suitable for practical uses. First of all, the effect of the wheel spin about the vertical axis and of the camber have been neglected. The contribution of the spin about the vertical axis is relatively small. The effect of camber has a sine-like dependance on the angle (Abe, 2009), hence it can be neglected for small cambers: this choice makes the identification of other tyre parameters much easier, with a reduced loss of generality since camber effect could be introduced later. Moreover, the dependance of the forces from the normal load is considered linear. Therefore, calling $F_{x,y}$ the generic force model and N the normal load, it is allowed to

study the normalized forces:

$$F^0_{x,y} = \frac{F_{x,y}}{N} \tag{3.1}$$

Since the remaining variables affecting the tyre-ground interaction are the slips, attention has been paid to their mathematical representation. The next section gives an accurate description of the models used to represent the slips, focusing on both the steady-state and the dynamic condition. Furthermore three models used to represent the forces are described in § 3.1.2, with emphasis on their advantages/limitations and on their suitability for practical use.

3.1.1 Slip Modelling

As explained, most important variables for the formulation of the contact forces are the slips. It has been experimentally demonstrated (Pacejka , 1958, Pacejka and Radt , 1963, Zegelaar , 1998) that the forces between tyre and ground are generated mainly in presence of slip. The following sections will give a panorama about the mathematical formulation for the definition of the slips, including some mathematical skills introduced to avoid numerical singularities.

Steady-State Slips

For the definition of the relations between the tyre slips and the tyre-ground forces, it is necessary to define two indexes that quantify the longitudinal and lateral slips. For the longitudinal case, the best choice concerns the definition of an index that a) considers the differences between the tyre longitudinal and angular velocities, b) is independent on the tyre absolute velocity and c) models the case of driving/braking full slip as a limit behaviour.

At braking or driving the slip point (denoted as S in Fig. 3.2) moves with a longitudinal speed v_{sx} which differs from zero. Thus obviously it can be written that:

$$v_{sx} = u - \omega R \tag{3.2}$$

where ω is the wheel angular velocity and R is the rolling radius. The longitudinal slip κ, also known as slip ratio, may be tentatively defined as the ratio of the longitudinal slip velocity $-v_{sx}$ of the point S and the forward speed of the wheel centre u:

$$\kappa = -\frac{v_{sx}}{u} \tag{3.3}$$

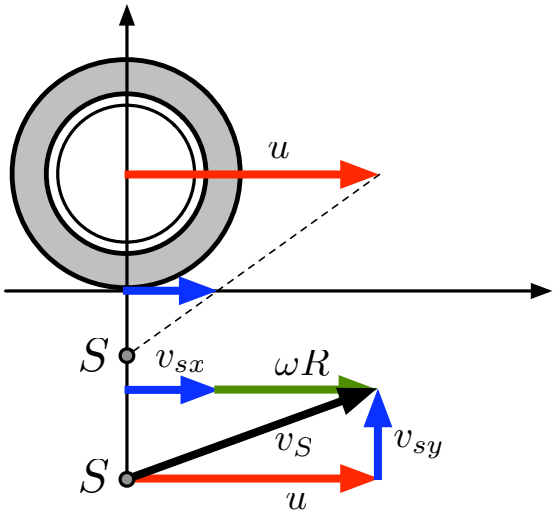

Figure 3.2: Velocities components of tyre-ground contact point. v_S is the contact point absolute speed, which can be divided in two components, while ω is the wheel spin velocity. The comparison of these velocity components allow the definition of the slips.

or with (3.2):

$$\kappa = \frac{\omega R - u}{u} \tag{3.4}$$

In this way a normalized index is defined in the range [-1,1], where the boundary limits represent the full slip conditions. Nevertheless such a definition presents two limitations:

- it is valid just for the braking manoeuvre ($\omega R > u$) - Supposing, for instance, the driving case in which $\omega R = 2u$, the slip ratio becomes

  $$\kappa = \frac{2u - u}{u} = 1$$

  but such a value of κ should be obtained just in the case that $u = 0$ and $\omega R \neq 0$ (completely slipping tyre).

- it is not valid for the inversion of the motion ($u < \omega R < 0$) - Supposing the braking case during a straight backward manoeuvre in which $\omega R = -1$ and $u = -2$, the force and thus the slip should be positive, but (3.4)

gives:

$$\kappa = \frac{-1-(-2)}{-2} = -0.5$$

In order to solve the presented singularities, the chosen formulation of the longitudinal slip ratio becomes

$$\kappa = \frac{\omega R - u}{\max(|u|, |\omega R|)} \tag{3.5}$$

that models both the driving and braking manoeuvres, in both forward and backward directions.

The definition of an index of the lateral slip has to a) take into account the lateral velocities of the contact point and b) model the case of pure lateral motion as a limit behaviour. The lateral slip is defined as the ratio of the lateral velocity v_{sy} of the contact point and longitudinal running speed. In terms of the sideslip angle λ it becomes:

$$\tan(\lambda) = \frac{v_{sy}}{u} \tag{3.6}$$

In this way the index respects both the requirements, considering the lateral velocity of the contact point and assuming the limit values [-π/2,π/2] in case of pure lateral slip ($v_{sy} \neq 0$ and $u = 0$).

As for the longitudinal slip, this formulation presents a limitation in the case of the inversion of the motion ($u < 0$). In such a case the slip angle assumes absolute values larger than $\pi/2$, that are not allowed for definition. The problem can be easily solved as for the previous case using the absolute value of the longitudinal speed, and the sideslip angle becomes:

$$\tan(\lambda) = \frac{v_{sy}}{|u|} \tag{3.7}$$

Steady-State Slip Combination

The definitions given above regard the case of a pure lateral or longitudinal motion, but they cannot be used for the combination of the phenomena. If one separately treats the motions, the adherence region (*i.e* the area in which the tyre-ground force must fall) becomes rectangular, which is in contrast with the well known adherence ellipse or Kamm's circle concept (Kiencke and Nielsen , 2000). (Pacejka , 2005) discusses some modelling approaches to take into account this phenomenon: for the present work the problem has been solved by means of the so-called "slips combination".

In order to describe the deflection of the tyre in the adherence region, the theoretical slip quantities σ_x, σ_y are introduced, that can be computed as:

$$\sigma_x = -\frac{\kappa}{1+\kappa} \tag{3.8}$$

$$\sigma_y = -\frac{\tan(\lambda)}{1+\kappa} \tag{3.9}$$

and the absolute magnitude of the deflection becomes the following:

$$\sigma_{eq} = \sqrt{\sigma_x^2 + \sigma_y^2} \tag{3.10}$$

It is worth noting that the theoretical slips σ_x and σ_y are subject to the same singularities due to the motion inversion that are present in the pure slips κ and λ. The problem can be solved again by exploiting the absolute value and the corrected formulations for the theoretical slips become the following:

$$\sigma_x = -\frac{\kappa}{1+|\kappa|} \tag{3.11}$$

$$\sigma_y = -\frac{\tan(\lambda)}{1+|\kappa|} \tag{3.12}$$

With these quantities, the introduction of the adherence ellipse concept is quite intuitive. It has been shown that, under the described assumptions, the normalized forces are functions of the slips as:

$$F_x^0 = F_x^0(\kappa) \tag{3.13}$$

$$F_y^0 = F_y^0(\lambda) \tag{3.14}$$

and that this formulation brings to have a rectangular adherence region. The slips combination presents instead the following formulation, which respects the Kamm's circle concept:

$$F_x^0 = \frac{\sigma_x}{\sigma_{eq}} F_x^0(\sigma_{eq})\,, \qquad F_y^0 = \frac{\sigma_y}{\sigma_{eq}} F_y^0(\sigma_{eq}) \tag{3.15}$$

In other words, the forces are computed applying the force models to the deflection magnitude σ_{eq}, and then normalizing the values. This formulation introduces an interaction between lateral and longitudinal motions, respecting the slip definitions and constraining the forces to fall into the adherence ellipse.

First Order Lag Model

The models treated in the previous sections describe the slip phenomenon in steady-state condition, but the tyre is a mechanical system and a mathematical representation of its dynamics is then necessary. In (Pacejka , 2005) the author presents an empirical description of the tyre behaviour (*i.e.* the "brush model") and of its dynamic response. It is shown that the transfer functions between the slips and the forces obtained with that model are quite complex (with a second order denominator and a delay), but that a good matching can be achieved using an approximate model.

Precisely, it is demonstrated that the slips approach the steady-state values as first order systems, with a characteristic period that depends on the longitudinal contact speed. The differential equations that govern the transient slip response of the contact patch and, through that the longitudinal force responses, become for the approximate system:

$$l_x \frac{d\kappa}{dt} + u\,\kappa = \frac{\omega R - u}{u} \tag{3.16}$$

$$l_y \frac{d\lambda}{dt} + u\,\lambda = \arctan\left(\frac{v_{sy}}{u}\right) \tag{3.17}$$

where l_x and l_y are respectively the lateral and longitudinal relaxation lengths, that quantify the portion of the tyre subjected to deflection because of the slips.

As one can see, this representation is subjected to the same singularities described for the steady-state slips. The solution to this problem is the same introduced before, and the formulation of the slips dynamics becomes as follows:

$$l_x \frac{d\kappa}{dt} + \max(|u|, |\omega R|)\kappa - (\omega R - u) = 0 \tag{3.18}$$

$$l_y \frac{d\lambda}{dt} + \max(|u|, |\omega R|)\left[\lambda - \arctan\left(\frac{v_{sy}}{u}\right)\right] = 0 \tag{3.19}$$

Low velocity condition

The previous model is straightforward and is often used in transient or low frequency vehicle motion simulation applications. Starting from zero speed or stopping to standstill is possible. However at u equal or close to zero ($u < V_{low}$) the equations (3.18),(3.19) act as integrators of the slip speed components $v_{sx,y}$, which may give rise to possibly very large deflections.

Therefore at zero forward speed a virtually undamped vibration is expected to occur. To artificially introduce some damping at very low speed, which with the actual tyre is established through material damping, one might employ the following expression for the transient slip κ' as suggested by (Besselink , 2000):

$$\kappa' = \kappa - k_{V,low} v_{sx} \tag{3.20}$$

The gradual reduction to zero at $u = V_{low}$ is realised by using the formula:

$$\begin{array}{ll} k_{V,low} = \frac{1}{2} k_{V,low0} \left\{ 1 + \cos(\pi \frac{|u|}{V_{low}}) \right\} & \text{if } |u| \leq V_{low} \\ k_{V,low} = 0 & \text{if } |u| > V_{low} \end{array} \tag{3.21}$$

With such a formulation, the undamped vibration is avoided, maintaining the continuity of the slip definition at low or zero speed condition. $k_{V,low0}$ and the threshold V_{low} depend both on the tyre carcass and the vehicle dynamics, and they should be experimentally identified. Nevertheless precautionary values that can be assumed for a large set of vehicles and tyres are $k_{V,low0} = 50$ s/m and $V_{low} = 1$ m/s.

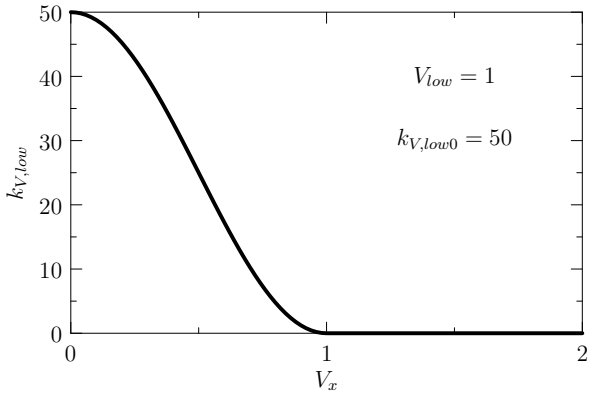

Figure 3.3: Profile of the transitory function $k_{V,low}$ for $V_{low} = 1$ m/s and $k_{V,low0} = 50$ s/m. The function allows to introduce a virtual damping at low velocities, adding a small virtual slip when $u < V_{low}$.

3.1.2 Force Models

As described at the beginning of this section, the tyre-ground interaction mainly depends on the slips. Several mathematical representation of the re-

lation between the slips and the forces can be found in literature: the next sections describe three models studied fot the present research.

First of all, the well known "Magic Formula" introduced by Pacejka is discussed. The main advantages of such a model are that it matches very well with the experimental data and maintains some peculiar behaviours of the system. Therefore it is not a mere data approximation. Nonetheless its construction requires a huge set of experimental data and parameters depending on the tyre and the soil and that are difficult to be identified. For this reason two other models are presented, that are characterized by a smaller set of parameters and, thus, directly suitable for the description of the tyre forces.

The Magic Formula

A widely used semi-empirical tyre model to calculate steady-state tyre force characteristics for use in vehicle dynamics studies is based on the so-called "Magic Formula". The development of the model was started in the mid-eighties (Bakker et al., 1987) and has been modified and improved up to the final version proposed in (Pacejka , 1996).

The general form of the formula that holds for given values of vertical load reads:

$$y = D \sin\{C \arctan\left[Bx - E(Bx - \arctan(Bx))\right]\} \tag{3.22}$$

with

$$Y(X) = y(x) + S_V \tag{3.23}$$

$$x = X + S_H \tag{3.24}$$

where

Y: output variable F_x, F_y or possibly M_z
X: input variable $\tan(\lambda)$ or κ

and

B: stiffness factor
C: shape factor
D: peak value
E: curvature factor
S_H: horizontal shift
S_V: vertical shift

The "Magic Formula" $y(x)$ typically produces a curve that passes through the origin $x = y = 0$, reaches a maximum and subsequently tends to a horizontal asymptote. For given values of the coefficients B, C, D and E the curve shows an anti-symmetric shape with respect to the origin. To allow the

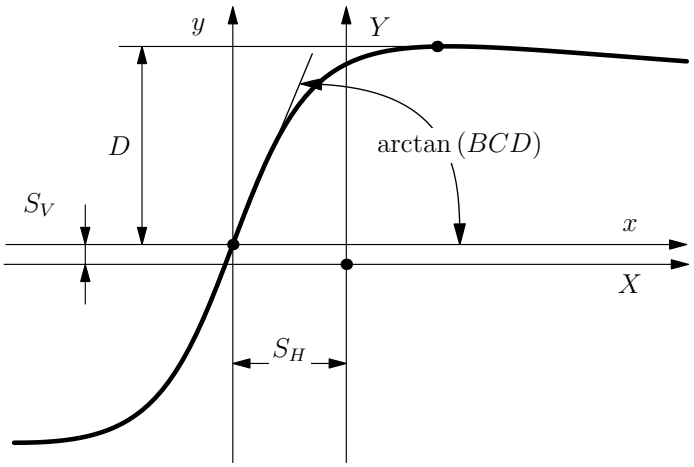

Figure 3.4: Curve produced by the Magic Formula: the meaning of curve parameters have been indicated. The Magic Formula accurately represents the force profile, including all the non-linear effects. Nevertheless it presents a large set of parameters and factors hard to identify.

curve to have an offset with respect to the origin, two shifts S_H and S_V have been introduced.

The formula is capable of producing characteristics that closely match measured curves for the side force F_y and for the fore and aft force F_x as functions of their respective slip quantities.

Fig. 3.4 illustrates the meaning of some of the factors by means of a typical side force characteristic. Obviously, coefficient D represents the peak value (with respect to the central x-axis and for $C \geq 1$) and the product BCD corresponds to the slope at the origin ($x = y = 0$). The shape factor C controls the limits of the range of the sine function appearing in (3.22) and thereby determines the shape of the resulting curve. The factor B is left to determine the slope at the origin and is called the stiffness factor. The factor E is introduced to control the curvature at the peak and at the same time the horizontal position of the peak.

As shown, the "Magic Formula" presents a large set of parameters that makes its employment difficult for practical uses. Therefore the models described below have been preferred for the simulations.

The Linear Model

This representation comes from the linearization of the "Magic Formula" for small slips. It can be shown that the product BCD corresponds to the slope at the origin ($x = y = 0$). This product is called driving stiffness k_κ, for the longitudinal force, and cornering stiffness k_λ for the side force. Hence, applying these definitions to the linearization of (3.22), the forces models become:

$$F_x^0 = -k_\kappa \kappa \tag{3.25}$$
$$F_y^0 = -k_\lambda \lambda \tag{3.26}$$

Obviously, the application of such a representation is limited to small slip values, since it does not represent the saturation that characterizes the forces in high-slip condition.

The Dugoff Model

In order to fill the gaps of the previous models, the non-linear model proposed in (Dugoff et al., 1970) has been used for several simulations, since it describes the main tyre behaviour characteristics (i.e. linearity for small slip values, saturation for high slip values and longitudinal and lateral force combined behaviour) with a limited number of parameters. The main advantage of this model is its suitability for on-line identification process, by means of Recursive Least Square methods as in (Hsu and Gerdes , 2006), even if the tyre force description for high slip condition is not very accurate, as shown in Fig. 3.5. Let's notice that the model is extremely useful for real-time identification and control design activities, while for control algorithms validation it should be replaced with a more representative one (*e.g.* the "Magic Formula"). In fact it neglects the adherence decrease after saturation, and the different behaviour in lateral and longitudinal high slip conditions is not contemplated.

The essence of the model is given by the following equation:

$$F_{x,y}^0 = -k_\alpha \alpha f(\gamma) \tag{3.27}$$

where

$$f(\gamma) = \begin{cases} (2-\gamma)\gamma & \text{if} \quad \gamma < 1 \\ 1 & \text{if} \quad \gamma \geq 1 \end{cases} \tag{3.28}$$
$$\gamma = \frac{\mu}{2k_\alpha |\alpha|} \tag{3.29}$$

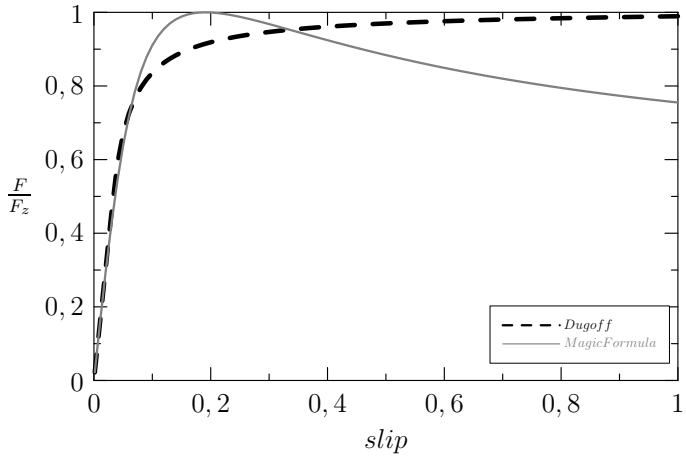

Figure 3.5: Comparison between Dugoff model and typical tyre force profile (obtained with the Pacejka's "Magic Formula"). In spite of its reduced number of parameters, the Dugoff model represents the force saturation. Nevertheless its monotonic profile neglects the typical slope change in high-slip condition.

α represents the generic slip (*i.e.* κ for the longitudinal case, $\tan(\lambda)$ for the lateral one) and k_α the generic stiffness (*i.e.* k_κ for the longitudinal case, k_λ for the lateral one).

3.2 Vehicle Dynamics

A mathematical model can be considered as an abstraction of the reality or, in other words, of the investigated phenomenon. In the vehicle case a dynamic model is represented by a set of Differential Algebraic Equations (DAE), where the differential subset describes the equations of motions and the algebraic one describes the kinematic constraints. The model has to be obviously representative, *i.e.* it has to capture the salient aspects that characterise the studied phenomenon. Larger the number of considered aspects better the representation is, to the detriment of the understanding simplicity. For these reasons a relevant part of the modelling activity has been focused on the study of multibody models representing the vehicle dynamics. Multibody models have been studied for both the analysis of specific motions (*e.g.* roll motion, pitch motion, etc.) and for the representation of the whole vehicle dynamics.

Despite the fact that the study of subsets of motions gives very useful

results, the most interesting observations can be done representing the whole vehicle. Such models can differ for the considered phenomena, and for the number of bodies, Degrees of Freedom and inputs taken into account: it is then obvious that a large set of models could be defined. The next sections discuss three main models, each one oriented to perform a specific task.

- The single-track or "bicycle" model, presenting 5 Degrees of Freedom - It gives a good description of the vehicle longitudinal dynamics. Moreover, thanks to its simplified formulation, it can be linearized and used to design control strategies (as discussed in Chapter 6).

- The 8 Degrees of Freedom Model - It represents also the sprung mass roll dynamics, and accurately describes both the longitudinal and lateral dynamics, comprising the load transfers and the rollover. Such a model is the main subject of the off-line identification activity carried out for Kanon and discussed in § 4.1.2.

- The 14 Degrees of Freedom Model - This model presents all the vehicle DOFs and accurately describes much of the vehicle behaviour. Because of its complexity, it is used just in simulation activity, and in particular to represent the vehicle dynamics in the static simulator used to test the control strategies discussed in Chapter 6.

3.2.1 5 DOF: Bicycle Model

The simplest model used is the well known single track or "bicycle" model, which is used to synthesize the yaw moment control algorithms. Fig. 3.6 indicates the main state variables. The vehicle model is controlled by means of three inputs: the steering angle δ (measured on the road plane) and the driving/braking torques T_r and T_f at rear and front axle respectively. Traction torque is only acting on the rear axle and the global braking torque is distributed between front and rear axle. The wheel dynamics is included as average behaviour of each vehicle axle therefore the lateral load transfer is neglected.

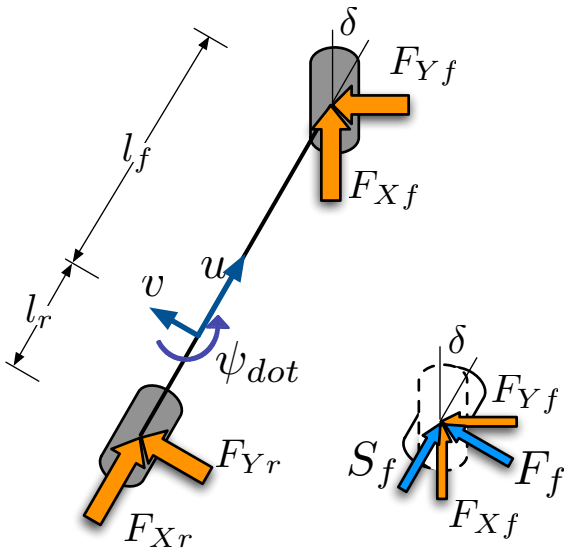

Figure 3.6: Main states and variables of the 5DOF model. In spite of the large set of introduced simplifications, the model gives a good description of the vehicle dynamics, especially in longitudinal direction. Moreover it can be easily linearized and used for control strategies design, as discussed in Chapter 6.

The equations of motion expressed in time domain are as follows:

$$M\left(\frac{du}{dt} - \psi_{dot} v\right) = S_r + S_f - F_{aero} \tag{3.30}$$

$$M\left(\frac{dv}{dt} + \psi_{dot} u\right) = F_r + F_f \tag{3.31}$$

$$I_Z \frac{d\psi_{dot}}{dt} = F_f l_f - F_r l_r \tag{3.32}$$

$$I_{Wr} \frac{d\omega_r}{dt} = T_r - F_{xr} R \tag{3.33}$$

$$I_{Wf} \frac{d\omega_f}{dt} = T_f - F_{xf} R \tag{3.34}$$

where the front axle tyre forces are projected in vehicle coordinate frame by means of the rotation through the steering angle:

$$S_r = F_{xr} \quad , \quad S_f = F_{xf}\cos(\delta) + F_{yf}\sin(\delta) \tag{3.35}$$

$$F_r = F_{yr} \quad , \quad F_f = -F_{xf}\sin(\delta) + F_{yf}\cos(\delta) \tag{3.36}$$

F_{aero} is instead the longitudinal effect of the drag force, due to air resistance, which can be modelled as:

$$F_{aero} = k_D u^2 \tag{3.37}$$

where k_D is the vehicle drag coefficient.

The longitudinal load transfer is included with the following algebraic equations that respectively define the rear and front axle vertical loads:

$$N_r = \frac{Mgl_f}{L} + \frac{h_D k_D u^2 + h_{CoM}\left(S_r + S_f\right)}{L} \tag{3.38}$$

$$N_f = \frac{Mgl_r}{L} - \frac{h_D k_D u^2 + h_{CoM}\left(S_r + S_f\right)}{L} \tag{3.39}$$

where h_{CoM} is the distance between the ground and the vehicle Centre of Mass (CoM), and h_D is the distance between the CoM and the drag force point of application.

In order to implement the control strategies it is necessary to estimate the longitudinal forces therefore the wheel dynamics (as average behaviour for rear and front axles) is considered. Consequently, the longitudinal and lateral pure slips of wheels on the front and rear axles, respectively, can be written as follows:

$$\kappa_r = \frac{\omega_r R - u}{\max(|u|, |\omega_r R|)} \tag{3.40}$$

$$\kappa_f = \frac{\omega_f R - (u\cos(\delta) - (v + \psi_{dot} l_f)\sin(\delta))}{\max(|u\cos(\delta) - (v + \psi_{dot} l_f)\sin(\delta)|, |\omega_f R|)} \tag{3.41}$$

$$\lambda_r = -\arctan\left(\frac{v - \psi_{dot} l_r}{u}\right) \tag{3.42}$$

$$\lambda_f = \delta - \arctan\left(\frac{v + \psi_{dot} l_f}{u}\right) \tag{3.43}$$

3.2.2 8 DOF Model Assuming Sprung Mass Roll Dynamics

The second model includes the non-linear sprung mass roll dynamics. It is assumed that the sprung mass rotates about the roll axis, which is kept fixed at a distance h_0 from the ground during the whole vehicle motion. Such an assumption is based on the hypothesis of perfectly flat road, *i.e.* when the sprung mass bounce dynamics can be neglected. Three main coordinate frames have been defined for this model:

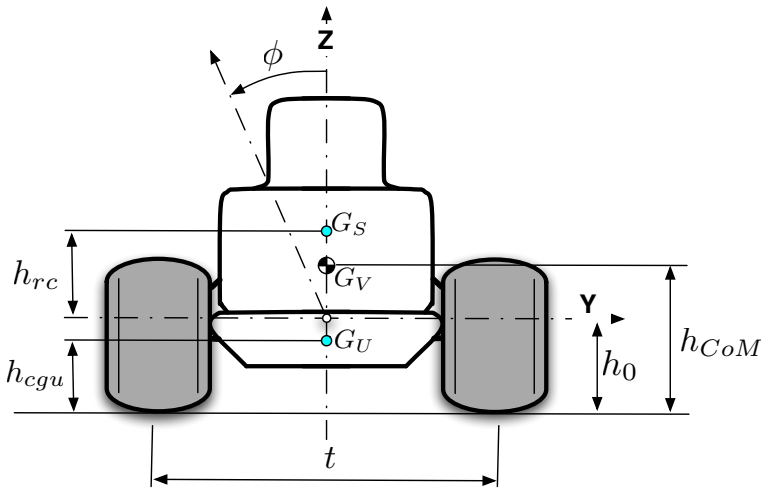

Figure 3.7: Main states and variables of the 8DOF model including the sprung mass roll dynamics. The roll motion is considered as a rigid rotation about the rolling axis, kept fixed at a distance h_0 from the ground. The distance h_{CoM} of the total CoM from the ground depends instead on the roll angle ϕ.

- the inertial frame XYZ,
- the body fixed coordinate frame (xyz) attached at the sprung mass CoM and aligned in principal directions (coordinate frame 1),
- coordinate frame 2, placed on the ground at the x-y positions of the CoM and aligned with the vehicle.

Fig. 3.7 shows the CoM positions for the unsprung mass G_U, for the sprung mass G_S, and the positions of the total CoM G_V. The equation of motions for the state variables u, v, ψ_{dot}, ϕ_{dot}, ω_{ij} are the following:

$$\begin{aligned} & M\left(\frac{du}{dt} - \psi_{dot} v\right) + 2M_s h_{rc}\cos(\phi)\psi_{dot}\phi_{dot} \\ & + M_s h_{rc}\sin(\phi)\frac{d\psi_{dot}}{dt} + 2(m_{ur}l_r - m_{uf}l_f)\psi_{dot}^2 \quad = \quad \sum F_{xij} + F_{aero} \end{aligned} \tag{3.44}$$

$$
\begin{aligned}
M\left(\frac{dv}{dt}+\psi_{dot}u\right)-M_s h_{rc}\cos(\phi)\frac{d\phi_{dot}}{dt}& \\
+M_s h_{rc}\sin(\phi)\left(\psi_{dot}^2+\phi_{dot}^2\right)& \\
+2(m_{ur}l_r-m_{uf}l_f)\frac{d\psi_{dot}}{dt} &= \sum F_{yij} \qquad (3.45)\\
\left[m_{ur}\left(2l_r^2+\frac{t_r^2}{2}\right)+m_{uf}\left(2l_f^2+\frac{t_f^2}{2}\right)\right]\frac{d\psi_{dot}}{dt}& \\
+\left[I_z\cos(\phi)^2+(I_y+M_s h_{rc}^2)\sin(\phi)^2\right]\frac{d\psi_{dot}}{dt}& \\
+(2m_{uf}l_f-2m_{ur}l_r)\left(\frac{dv}{dt}+\psi_{dot}u\right)& \\
+M_s h_{rc}\sin(\phi)\left(\frac{du}{dt}-\psi_{dot}v\right)& \\
+2(I_y-I_z+M_s h_{rc}^2)\sin(\phi)\cos(\phi)\psi_{dot}\phi_{dot}& \\
-M_s g h_{rc} &= \sum F_{ij}b_{ij} \qquad (3.46)\\
(I_x+M_s h_{rc}^2)\frac{d\phi_{dot}}{dt}& \\
-M_s h_{rc}\cos(\phi)\left(\frac{dv}{dt}+\psi_{dot}u\right)& \\
+(I_z-I_y-M_s h_r c^2)\sin(\phi)\cos(\phi)\psi_{dot}^2 &= T_s-M_s g\sin(\phi) \qquad (3.47)\\
I_{Wij}\frac{d\omega_{ij}}{dt} &= T_{ij}-S_{ij}R \qquad (3.48)
\end{aligned}
$$

where $T_s=-(K_{\phi f}+K_{\phi r})\phi-(B_{\phi f}+B_{\phi r})\phi_{dot}$ accounts for the equivalent elastic-damping torque of the suspensions and the subscript 'ij' denotes left front (lf), right front (rf), left rear (lr) and right rear (rr). b_{ij} represents instead the distance between the CoM and the ij-th tyre ground force.

As an example, the slips of tyre-ground contact point for the front-right wheel are as follows:

$$\kappa_{rf} = \frac{R\omega_{rf}-(u_{grf}\cos(\delta)+v_{grf}\sin(\delta))}{\max(|u_{grf}\cos(\delta)+v_{grf}\sin(\delta)|,|R\omega_{rf}|)} \qquad (3.49)$$

$$\lambda_{rf} = \arctan\left(\frac{v_{grf}}{u_{grf}}\right)-\delta \qquad (3.50)$$

where the velocities u_{grf} and v_{grf} can be expressed as

$$u_{grf} = u + \frac{t_f}{2}\psi_{dot} \tag{3.51}$$
$$v_{grf} = v + l_f\psi_{dot} \tag{3.52}$$

The model includes both lateral and longitudinal load transfers which is mainly due to three phenomena. The longitudinal accelerations produce a load transfer between front and rear axles, while the lateral accelerations are responsible for lateral load transfer between left and right wheels. The roll dynamics -third phenomenon- contributes to both longitudinal and lateral load transfers. Based on the above assumption the vertical load acting at each tyre can be written as follows:

$$N_{rf} = \frac{M_s g l_r}{2L} + \frac{M_s g h_{rc}\sin(\phi)}{2t_f} - \Delta N_\phi \frac{l_r}{2L} - \frac{\Delta N_x}{2L} + \frac{\Delta N_y}{2t_f} \tag{3.53}$$
$$N_{lf} = \frac{M_s g l_r}{2L} - \frac{M_s g h_{rc}\sin(\phi)}{2t_f} - \Delta N_\phi \frac{l_r}{2L} - \frac{\Delta N_x}{2L} - \frac{\Delta N_y}{2t_f} \tag{3.54}$$
$$N_{rr} = \frac{M_s g l_f}{2L} + \frac{M_s g h_{rc}\sin(\phi)}{2t_r} - \Delta N_\phi \frac{l_f}{2L} + \frac{\Delta N_x}{2L} + \frac{\Delta N_y}{2t_r} \tag{3.55}$$
$$N_{lr} = \frac{M_s g l_f}{2L} - \frac{M_s g h_{rc}\sin(\phi)}{2t_r} - \Delta N_\phi \frac{l_f}{2L} + \frac{\Delta N_x}{2L} - \frac{\Delta N_y}{2t_r} \tag{3.56}$$

In the previous equations, the term ΔN_ϕ represents the load variation due to roll accelerations, which is defined as:

$$\Delta N_\phi = M_s h_{rc}\left(\cos(\phi)\phi_{dot}^2 + \sin(\phi)\frac{d\phi_{dot}}{dt}\right) \tag{3.57}$$

The longitudinal and lateral load transfers can be written as:

$$\begin{aligned}
\Delta N_x &= Mh_{CoM}\left(\frac{du}{dt} - \psi_{dot}v\right) \\
&\quad + M_s h_0 h_{rc}\left(\frac{1}{2}\sin(\phi)\frac{d\psi_{dot}}{dt} + \cos(\phi)\psi_{dot}\phi_{dot}\right) \\
&\quad + \cos(\phi)\left(I_y + M_s h_{rc}^2 - I_z\right)\left(\frac{1}{2}\sin(\phi)\frac{d\psi_{dot}}{dt} + \cos(\phi)\psi_{dot}\phi_{dot}\right) \\
&\quad + (I_x + I_z - I_y)\frac{\psi_{dot}\phi_{dot}}{2} \\
&\quad + (m_{ur}l_r - m_{uf}l_f)r_0\psi_{dot}^2 - \frac{h_D k_D u^2}{2} \qquad (3.58) \\
\Delta N_y &= Mh_{CoM}\left(\frac{dv}{dt} + \psi_{dot}u\right) \\
&\quad - (I_x + M_s h_{rc}^2 + M_s h_0 h_{rc}\cos(\phi))\frac{d\phi_{dot}}{dt} \\
&\quad + (m_{ur}l_r - m_{uf}l_f)r_0\frac{d\psi_{dot}}{dt} \\
&\quad + (I_y - I_z + M_s h_{rc}^2)\sin(\phi)\cos(\phi)\psi_{dot}^2 \\
&\quad + M_s h_0 h_{rc}\sin\phi(\psi_{dot}^2 + \phi_{dot}^2) \qquad (3.59)
\end{aligned}$$

3.2.3 14DOF Model Assuming Sprung Mass and Unsprung Masses Dynamics

The most complex model, based on the one proposed by (Shim and Ghike , 2007), is the two axle, 14DOF model shown in Fig. 3.8. This schematic includes 6DOF at the vehicle CoM and 2DOF at each of the four wheels, namely, suspension deflection and wheel spin. Three main coordinate frames have been defined as for the 8DOF model. The sprung mass is a rigid body where u, v, and w respectively indicate its forward, lateral, and vertical velocities. To complete the degrees of freedom of the chassis the following roll angular velocity, ω_x, pitch angular velocity, ω_y, and yaw angular velocity, ω_z are defined. The attitude and position of body w.r.t. the inertial frame (XYZ) can be determined through successive coordinate transformations about the Cardan angles (*i.e.* the roll angle ϕ, the pitch angle θ, and the yaw angle ψ) as shown in Fig. 3.8. The coordinate frame 2 is obtained by rotating the inertial coordinate frame through the yaw angle ψ.

Fig. 3.9 shows the force and velocity components in the right front wheel.

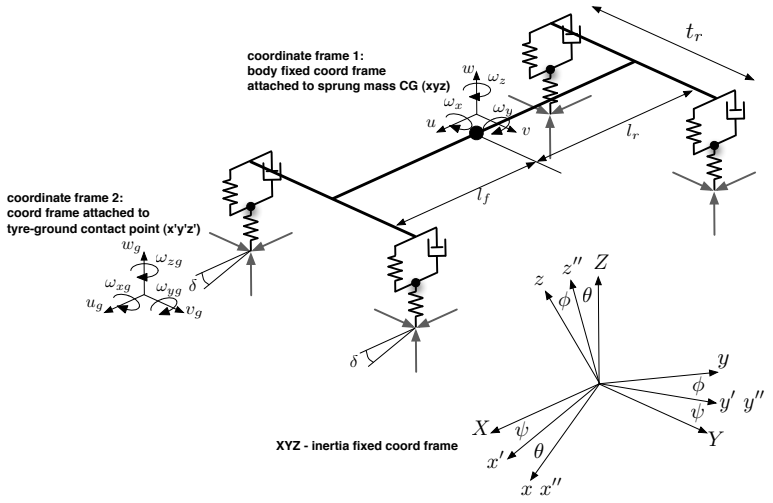

Figure 3.8: Schematic of 14DOF full vehicle model with one-dimensional suspension and coordinate frames. The model includes the whole set of Degrees of Freedom characteristic of normal vehicles, comprising the tyres and struts deflections. Two main coordinate frames have been defined for the whole vehicle, while a specific frame has been defined for each sprung mass system.

The velocities u_{srf}, v_{srf}, and w_{srf} are the velocities of the right front strut mounting point in the longitudinal, lateral, and vertical directions, respectively, in the coordinate frame 1. These velocities can be obtained by transforming the CoM velocities as:

$$\begin{Bmatrix} u_{srf} \\ v_{srf} \\ w_{srf} \end{Bmatrix} = \begin{bmatrix} 0 & 0 & \frac{t_f}{2} \\ 0 & 0 & l_f \\ -\frac{t_f}{2} & -l_f & 0 \end{bmatrix} \begin{Bmatrix} \omega_x \\ \omega_y \\ \omega_z \end{Bmatrix} + \begin{Bmatrix} u \\ v \\ w \end{Bmatrix}. \tag{3.60}$$

The velocities u_{urf}, v_{urf}, and w_{urf} represent the velocities of the unsprung mass m_u in the body-fixed coordinate frame 1, and u_{grf}, v_{grf}, and w_{grf} are the lateral, longitudinal, and vertical velocities at the tyre-ground contact patch in coordinate frame 2. The forces F_{xsrf}, F_{ysrf}, and F_{zsrf} are the forces transmitted to the sprung mass along the longitudinal, lateral, and vertical directions, respectively, of coordinate frame 1. The forces F_{xgsrf}, F_{ygsrf}, and F_{zgsrf} are the forces acting at the tyre-ground contact patch in the same frame. These forces can be written in terms of the tyre forces F_{xgrf}, F_{ygrf},

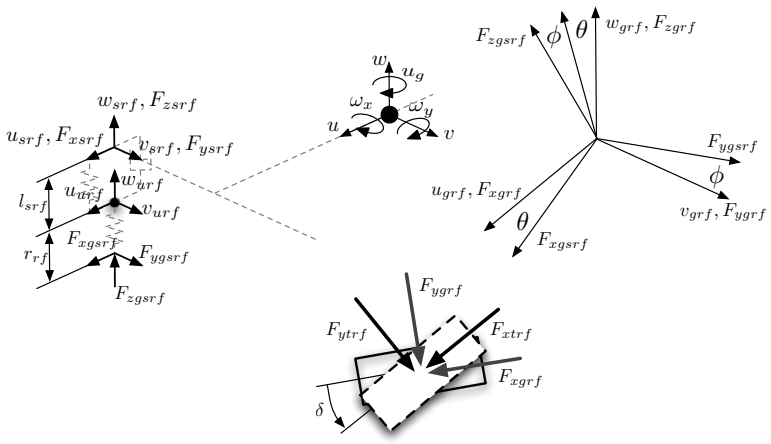

Figure 3.9: Description of forces and velocities at the right front wheel. The forces and velocities at front (steered) wheels can be projected on unsprung mass coordinate frame through the steering angles. The forces and velocities of each unsprung mass can instead be projected on the vehicle frame through the Cardan angles.

and F_{zgrf} by projecting its components along coordinate frame 2 as:

$$\left\{ \begin{array}{c} F_{xgsrf} \\ F_{ygsrf} \\ F_{zgsrf} \end{array} \right\} = \left[\begin{array}{ccc} 1 & 0 & 0 \\ 0 & \cos(\phi) & \sin(\phi) \\ 0 & -\sin(\phi) & \cos(\phi) \end{array} \right] \left[\begin{array}{ccc} \cos(\theta) & 0 & -\sin(\theta) \\ 0 & 1 & 0 \\ \sin(\theta) & 0 & \cos(\theta) \end{array} \right] \left\{ \begin{array}{c} F_{xgrf} \\ F_{ygrf} \\ F_{zgrf} \end{array} \right\}. \tag{3.61}$$

The forces F_{xgrf} and F_{ygrf} are obtained by resolving the longitudinal (F_{xtrf}) and cornering (F_{ytrf}) forces at the tyre-ground contact patch as:

$$F_{xgrf} = F_{xtrf}\cos(\delta) - F_{ytrf}\sin(\delta) \tag{3.62}$$

$$F_{ygrf} = F_{ytrf}\cos(\delta) + F_{xtrf}\sin(\delta) \tag{3.63}$$

where δ is the steering angle measured on the road plane.

The pure slips necessary to model the forces are computed as follows:

$$\kappa_{rf} = \frac{r_{rf}\omega_{rf} - (u_{grf}\cos(\delta) + v_{grf}\sin(\delta))}{\max(|u_{grf}\cos(\delta) + v_{grf}\sin(\delta)|, |r_{rf}\omega_{rf}|)} \tag{3.64}$$

$$\lambda_{rf} = \arctan\left(\frac{v_{grf}}{u_{grf}}\right) - \delta \tag{3.65}$$

where r_{rf} is the instantaneous tyre radius.

The longitudinal and lateral velocities at the tyre contact patch, u_{grf} and v_{grf}, can be determined as:

$$\begin{aligned} u_{grf} &= \cos(\theta)(u_{urf} - \omega_y r_{rf}) \\ &\quad + \sin(\theta)\left[\cos(\phi)(w_{urf} - \dot{r}_{rf}) + \sin(\phi)(\omega_x r_{rf} + v_{urf})\right] \quad (3.66) \\ v_{grf} &= \cos(\phi)(v_{urf} + \omega_x r_{rf}) - \sin(\phi)(w_{urf} - \dot{r}_{rf}) \quad (3.67) \end{aligned}$$

Nevertheless with this formulation the ODE becomes very complicated, then the tyre deformation rate $\dot{r}_{rf}$ is neglected obtaining a good simplification to the detriment of a minimal approximation.

The longitudinal (u_{urf}) and lateral (v_{urf}) velocities of the unsprung mass in the body-fixed coordinate frame used in the earlier equations are simply written as:

$$\begin{aligned} u_{urf} &= u_{srf} - l_{srf}\omega_y \quad (3.68) \\ v_{urf} &= v_{srf} + l_{srf}\omega_x \quad (3.69) \end{aligned}$$

where l_{srf} is the instantaneous length of the strut as indicated in Fig. 3.9. The unsprung mass vertical velocity w_{urf} represents the DOF corresponding to the suspension deflection, then the instantaneous suspension spring deflection x_{srf} is given as

$$\dot{x}_{srf} = -w_{srf} + w_{urf} \quad (3.70)$$

The instantaneous tyre deflection x_{trf} is instead given as

$$\begin{aligned} \dot{x}_{trf} &= w_{grf} - w_{uirf} \\ &= w_{grf} - (w_{urf}\cos(\phi) + v_{urf}\sin(\phi))\cos(\theta) - u_{urf}\sin(\theta) \quad (3.71) \end{aligned}$$

where w_{uirf} is the vertical velocity of the wheel centre in the inertial coordinate frame. For the simulations in this paper, it is assumed that the vertical velocity w_{grf} at the tyre-ground contact patch is zero (smooth road). It should be noted that even though the tyre is assumed to remain at a fixed angle with the strut, the vertical stiffness of the tyre, k_{tf}, is always considered to be normal to the ground, between the ground and the wheel centre. The instantaneous tyre radius is then determined as

$$r_{rf} = \frac{R - x_{trf}}{\cos(\theta)\cos(\phi)} \quad (3.72)$$

The instantaneous length of the strut l_{srf} used in (3.68)-(3.69) is given as

$$l_{srf} = l_{sif} - (x_{srf} - x_{sif}) \tag{3.73}$$

where l_{sif} is the initial length of strut and x_{sif} is the initial suspension spring deflection. The initial length of the strut l_{sif} is taken such that

$$l_{sif} = h - (r_0 - x_{tif}) \tag{3.74}$$

where x_{tif} is the initial tyre compression and h is the distance of the vehicle CoM from the ground with extended suspensions and undeformed tyres.

The initial spring compression x_{sif} and the initial tyre compression x_{tif} are determined from the static conditions as

$$x_{sif} = \frac{mgl_r}{2Lk_{sf}} \tag{3.75}$$

$$x_{tif} = \frac{mgl_r}{2Lk_{tf}} + \frac{m_{uf}g}{k_{tf}} \tag{3.76}$$

Supposing a linear spring tyre model, the vertical force F_{zgrf}, acting at tyre-ground contact point, can be written w.r.t. the frame 2 as

$$F_{zgrf} = F_{ztrf} = k_{tf}x_{trf} \tag{3.77}$$

where k_{tf} is the tyre vertical stiffness.

The forces F_{xsrf} and F_{ysrf} transmitted to the sprung mass along the u- and v-axes of the body-fixed coordinate frame are obtained after subtracting the components of the unsprung mass weight and inertia forces from the corresponding forces F_{xgsrf} and F_{ygsrf} acting at the tyre-ground contact patch as

$$F_{xsrf} = F_{xgsrf} + m_u(g\sin(\theta) - \dot{u}_{urf} + \omega_z v_{urf} - \omega_y w_{urf}) \tag{3.78}$$

$$F_{ysrf} = F_{ygsrf} - m_u(g\sin(\phi)\cos(\theta) + \dot{v}_{urf} - \omega_x w_{urf} + \omega_z u_{urf}) \tag{3.79}$$

The vertical force F_{srf} transmitted to the sprung mass through the strut is given as

$$F_{zsrf} = k_{srf}x_{srf} + b_{srf}\dot{x}_{srf} \tag{3.80}$$

Fig. 3.10 shows the forces and velocities in the roll plane of, for example, the front suspension. Generally, the roll centre height is defined with reference to the ground. However, for this model the front and rear roll centres are assumed to be fixed at distances h_{rcf} and h_{rcr}, respectively, below the sprung

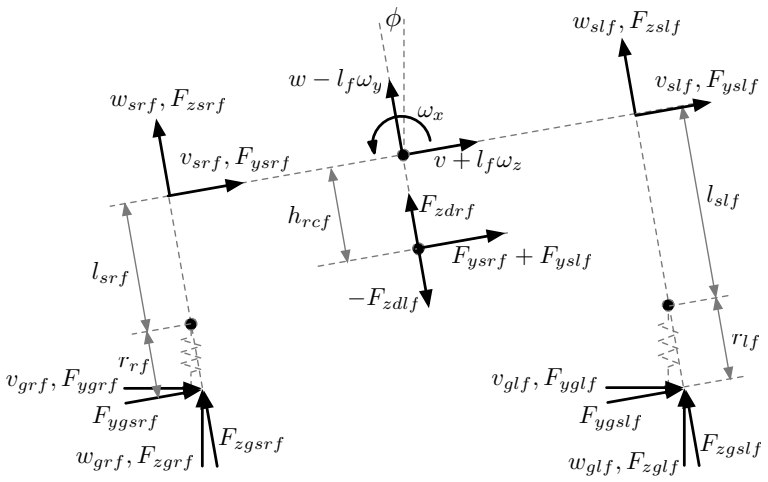

Figure 3.10: Forces and velocities in the front suspension roll plane. The roll centre is considered to be the point of application of the forces. The inclusion of a roll centre moderately reduces the total roll moment transmitted to the sprung mass through the suspensions, but strongly simplifies the system of equations.

mass CoM along the negative w-axis of the coordinate frame 1. Moreover, the roll centre is simply considered to be a point of application of the forces transmitted to the sprung mass through the suspension links and not as a kinematic constraint.

In Fig. 3.10, F_{zslf} and F_{zsrf} are the forces transmitted to the sprung mass through the struts. F_{yslf} and F_{ysrf} represent the lateral forces transmitted to the sprung mass through the suspension links. The roll moment M_{xrf} transmitted to the sprung mass by the right front corner suspension is given as

$$M_{xrf} = F_{ysrf} h_{rcf} \tag{3.81}$$

The difference between the roll moments in the absence of the roll centre and when the roll centre is considered acts directly on the unsprung mass and is responsible for the link load transfer forces (jacking forces), F_{dzlf} and F_{dzrf}.

These forces can be estimated as

$$\begin{aligned} F_{zdrf} &= -F_{zdlf} \\ &= \frac{F_{ygsrf} r_{rf} + F_{ysrf} l_{srf} + F_{ygslf} r_{lf} + F_{yslf} l_{slf}}{t_f} \\ &\quad - \frac{(F_{ysrf} + F_{yslf}) h_{rcf}}{t_f} \end{aligned} \tag{3.82}$$

As example, the moments M_{yrf} and M_{zrf} transmitted to the sprung mass at the right front wheel by the suspension along the ω_y and ω_z directions can be given as:

$$\begin{aligned} M_{yrf} &= -F_{xgsrf}(l_{srf} + r_{rf}) \\ &\quad -m_u l_{srf}(-g\sin(\theta) + \dot{u}_{urf} - \omega_z v_{urf} + \omega_y w_{urf}) \\ &= -F_{xgsrf} r_{rf} - F_{xsrf} l_{srf} \end{aligned} \tag{3.83}$$

$$M_{zrf} = 0 \tag{3.84}$$

The equations of motion for the 6DOF of the sprung mass model can now be derived from the direct application of Newton-Euler method as follows:

$$M_s(\dot{u} + \omega_y w - \omega_z v) = \sum(F_{xij}) + M_s g \sin(\theta) \tag{3.85}$$

$$M_s(\dot{v} + \omega_z u - \omega_x w) = \sum(F_{yij}) - M_s g \sin(\phi)\cos(\theta) \tag{3.86}$$

$$M_s(\dot{w} + \omega_x v - \omega_y u) = \sum(F_{zsij} + F_{zdij}) - M_s g \cos(\phi)\cos(\theta) \tag{3.87}$$

$$\begin{aligned} I_x\dot{\omega}_x + (I_y - I_z)\omega_y\omega_z &= \sum(M_{xij}) + \frac{(F_{zslf} - F_{zsrf})t_f}{2} \\ &\quad + \frac{(F_{zslr} - F_{zsrr})t_r}{2} \end{aligned} \tag{3.88}$$

$$\begin{aligned} I_y\dot{\omega}_y + (I_z - I_x)\omega_z\omega_x &= \sum(M_{yij}) + (F_{zsrr} + F_{zslr})l_r \\ &\quad -(F_{zsrf} + F_{zslf})l_f \end{aligned} \tag{3.89}$$

$$\begin{aligned} I_z\dot{\omega}_z + (I_x - I_y)\omega_x\omega_y &= \sum(M_{zij}) + (F_{ylf} + F_{yrf})l_f \\ &\quad -(F_{ylr} + F_{yrr})l_r + \frac{(F_{xrf} - F_{xlf})t_f}{2} \\ &\quad + \frac{(F_{xrr} - F_{xlr})t_r}{2} \end{aligned} \tag{3.90}$$

The equation of motion relative to w_{uij}, representing the degree of freedom due to suspension deflection, can be expressed by applying Newton's law for

the vertical motion of the sprung mass as:

$$\begin{aligned} m_u \frac{dw_{urf}}{dt} &= \cos(\phi)(\cos(\theta)(F_{zgrf} - m_u g) + \sin(\theta)F_{xgrf}) - \sin(\phi)F_{ygrf} \\ &\quad -F_{zdrf} - F_{zsrf} - m_u(\omega_x v_{urf} - \omega_y u_{urf}) \end{aligned} \tag{3.91}$$

Finally, the equation of motion for the degree of freedom relative to the wheel spinning rate can be expressed by applying the Euler's law as follows:

$$I_w \dot{\omega}_{ij} = T_{ij} - F_{xtij} r_{ij} \tag{3.92}$$

In all equations of motion, the subscript ij denotes left front (lf), right front (rf), left rear (lr), and right rear (rr).

The Cardan angles θ, ψ, ϕ needed in the afore mentioned equations are obtained by performing the integration of the following equations:

$$\dot{\theta} = \omega_y \cos(\phi) - \omega_z \sin(\phi) \tag{3.93}$$

$$\dot{\psi} = \frac{\omega_y \sin(\phi) + \omega_z \cos(\phi)}{\cos(\theta)} \tag{3.94}$$

$$\dot{\phi} = \omega_x + \tan(\theta)(\omega_y \sin(\phi) + \omega_z \cos(\phi)) \tag{3.95}$$

3.3 Vehicle Subsystems

As already introduced, it could be advantageous to study separately some vehicle subsystems, in order to treat their effects on the whole vehicle dynamics as black boxes. In the present research activity three main subsystems of RUMBy (suspensions, steering chain and power train) and one of the vehicle Kanon (suspensions) have been studied. The reason of such a difference is due to the fact that, for the vehicle Kanon, no data where available about the steering chain and to the fact that it is equipped with in-wheel electric motors previously identified.

3.3.1 Suspensions

The suspensions play the important role of transmitting the forces from the tyres to the sprung mass. Their geometry and the characteristics of the struts have thus a strong effect on the vehicle manoeuvrability, specially concerning the lateral dynamics.

Both RUMBy and Kanon are equipped with double-wishbone suspension, and the first stage in their representation regarded the kinematics analysis.

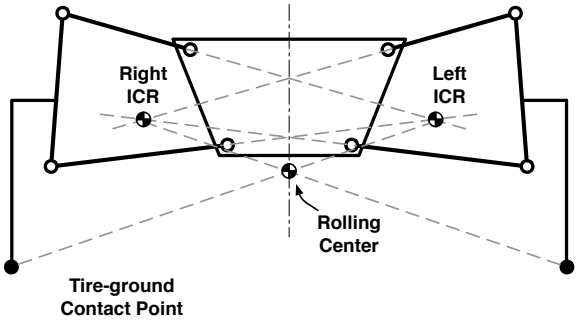

Figure 3.11: Geometrical evaluation of the RC on a double wishbone suspension. The analysis allows to estimate the positions of the rolling centre as a function of the suspensions configuration. Nevertheless the RC motions are very small, thus the goal of the analysis is normally to determine its average position, kept fixed w.r.t to the vehicle sprung mass.

Such an activity consists in the identification of the relations between the chosen DOF (*e.g.* the shock-absorber extension) and some variables as the tyre configuration (positions and orientations) or the rolling centre (RC) positions. For instance, Fig. 3.11 represents schematically the geometrical analysis done for the RC position evaluation (Dixon , 1996).

After the kinematic analysis, the struts effect on the sprung mass has to be studied. Another difference is there between the activities carried out for RUMBy and Kanon. While for RUMBy the struts has been taken down and identified separately, such an operation was not allowed for Kanon and the struts effect has been identified by means of their effect on the vehicle lateral dynamics: such an activity is described in detail in Chapter 4.

3.3.2 Steering Chain

The most important input of the vehicle system is doubtless the wheels steering angle. The lateral dynamics is predominated by the forces acting at the tyre-ground contact point, which are mainly due to the presence of a certain steering angle. Anyway in RUMBy the input signal controls the rotation of a servo-system, linked to the wheel rotation by means of a complex kinematic chain that comprises also the suspensions. For the control of the vehicle is therefore necessary to study such a kinematic chain, in order to know the relation between the control signal and the wheels orientation, depending on the suspensions configuration.

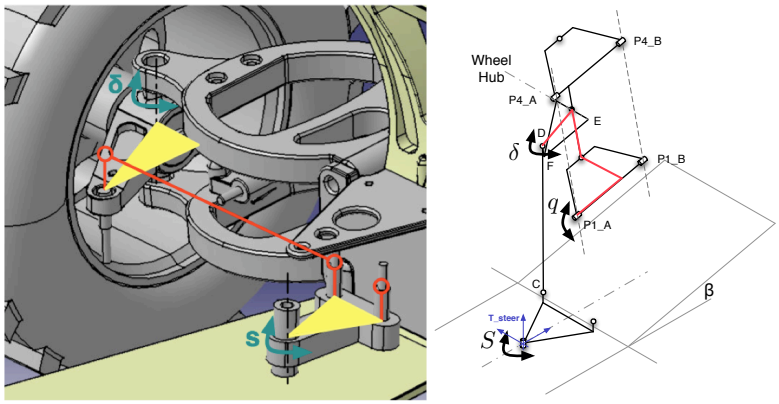

Figure 3.12: CAD (*left*) and schematic (*right*) representation of the RUMBy steering chain. The servo-motor rotates the central triangle of an angle S and the rotation is then transmitted to the wheels by means of the lateral arms: the final rotation δ of the wheel clearly depends on both the steering command S and the suspension configuration q.

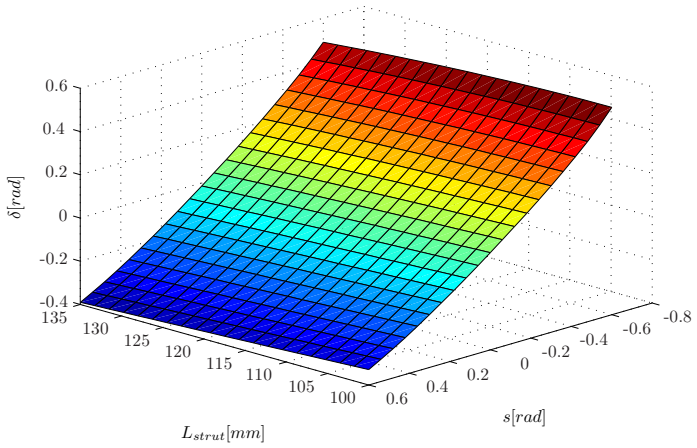

Figure 3.13: Characteristic curve "Steer angle VS Steer command and Strut extension". A trigonometric relation defines the profile: these non linear effects must be considered in case that large steering angles are required, for instance, during autonomous or assisted drive.

A mathematical model of the whole steering chain has been developed for the vehicle RUMBy, from the servo-system rotation up to the ground projection of the wheel steering angle. In Fig. 3.13 the trend of such an angle

depending on the strut extension and servomotor rotation is represented.

Such an analysis has highlighted two main characteristics of the RUMBy steering chain:

- a non-negligible effect of the suspension configuration, that represents a non-linear effect on the actual steering angle;
- a relevant asymmetry of the wheel rotation, *i.e.* with a certain input signal the right and left wheels rotate of different angles.

The present analysis allows to precisely know the effect of the steering control on the wheels rotations and thus on the vehicle dynamics, and the yielded non-linear relation must be taken into account in steering control strategies.

3.3.3 Power Train

Another important variable in control strategy synthesis is the driving torque, in terms of the force necessary to achieve a desired acceleration. While for Kanon the torque generated by the in-wheel motors is easily measurable from the electric motor current, in RUMBy such a torque is generated by a 2-stroke

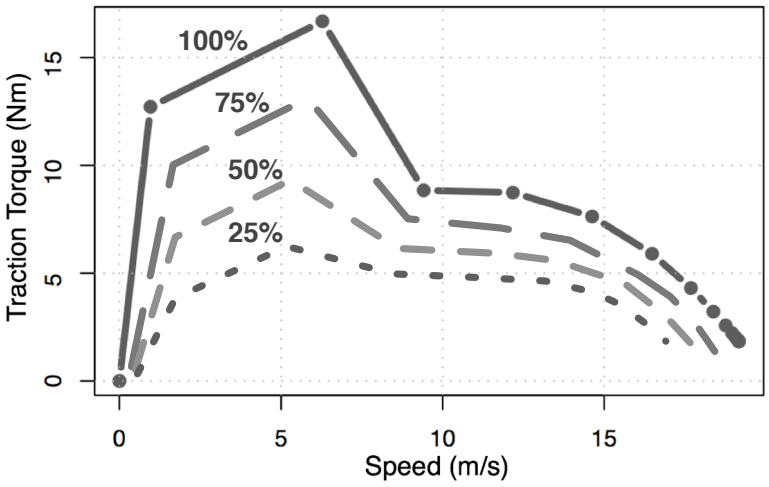

Figure 3.14: Profile of the traction torque at rear wheels as a function of forward speed and throttle percentage. Once the velocity is known, the maximum torque available is known: it is thus enough to act on the throttle percentage to control the actual driving torque.

engine (thus depending on the engine rpm) and transmitted to the wheels through a centrifugal clutch and a train of gear wheels (power train). It is therefore necessary a model which represents the whole power train behaviour, in order to know the available torque at every operating rate.

RUMBy is equipped with:

- a 2-stroke 26 cc engine, with known characteristics (no load max speed, idling speed, max power and max power speed, max torque and max torque speed);
- a centrifugal clutch with known geometry;
- a set of gear wheels with known geometry.

Using these information and a set of empirical formulation available in literature, a model of the whole power train has been written. From such a model some points "Torque VS speed" have been obtained as shown in Fig. 3.14: the continuous line represents the maximum traction torque available at every velocity. Similar curves can be identified for throttle in the range of [0% - 100%]: such a curve is necessary for the development of control strategies since throttle is the primary input for longitudinal dynamics.

3.4 Models comparison

In order to further clarify the differences between the models above described a simulation campaign has been done. Both the tyre representations and the multibody model influence the vehicle response to a certain set of inputs: the target of this section is to evidence the way the models affect such a response. In particular, in § 3.4.1 the effect of tyre models are compared and discussed, while § 3.4.2 aims at clarifying the differences between the multibody models concerning longitudinal and lateral dynamic responses.

3.4.1 Tyre models comparison

The effects of tyre models has been compared by means of a simulated straightforward manoeuvre. The RUMBy vehicle dynamics is described by the 5DOF multibody model, the steering angle is fixed at zero during the whole manoeuvre and the driving torque acting at the rear wheels has the ramp-like profile shown in Fig. 3.15. Such a torque profile is not really feasible on RUMBy

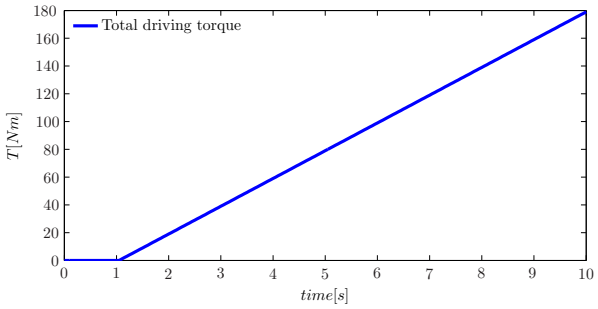

Figure 3.15: Tyre models comparison - Driving torque. A ramp-like profile has been chosen for the driving torque: even if it is not feasible, it allows to excite the whole slip ratio range and evidence the differences between the models.

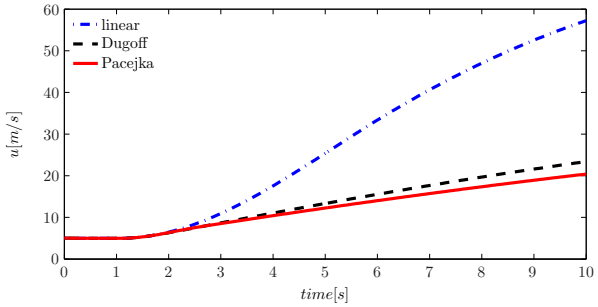

Figure 3.16: Tyre models comparison - Model longitudinal velocity. The models generate similar responses for small torques (and slips), while the differences are evident when the torque increases because of the force applicable by each model.

(a maximum total torque of 180 Nm is achieved!), but it has been chosen in simulation campaign in order to explore the whole range of longitudinal slips.

Fig. 3.16 shows the longitudinal velocities recorded during the tests with the three different tyre models: linear, Dugoff and Pacejka (Magic Formula). A different behaviour is evident from such a graph: the models present similar profiles in the first seconds (until about 2 seconds), while clear differences occur when the torque increases. The reason of such a mismatch is quite simple: while the driving torque is small the slips are small too and thus the tyre models have similar (linear) profiles. When the torque (and the slips) increases the linear model generates an increasing force (see Fig. 3.17) and the velocity grows as well, while Dugoff and Pacejka models reach the saturation.

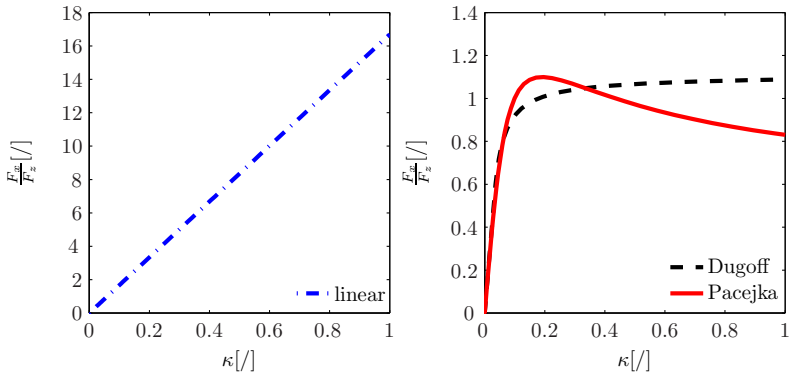

Figure 3.17: Tyre models comparison - "Normalized driving force VS Slip ratio". The slips and the forces generated by the linear (*left*), Dugoff and Pacejka models (*right*) have been recorded in order to evidence the different profiles.

As a consequence, the force generated by the linear representation is much larger than the one obtained with the other two models and this justifies the large dissimilarity between its velocity profile and the others.

Moreover, the difference between Dugoff and Pacejka is also evident. It has been explained in § 3.1.2 that Dugoff allows for the description of the force saturation, but also that it has a monotonic profile that is different from the Pacejka's one (see Fig. 3.17). Consequently, the forces generated by the models in presence of large slip ratios are different, and this generates the mismatch between the longitudinal velocity profiles.

3.4.2 Multibody models comparison

To evidence the differences between the multibody models is a bit more difficult than the previous case, since the number of aspects to consider is larger. Because of this, the problem has been solved by making three different tests: the first aims at studying the longitudinal dynamics, the second analyses the lateral dynamics characteristics and the third combines the effect of the previous two. It is worth noting that all the three models are coupled with the non-linear Dugoff tyre model, in order to evidence the dynamics effects.

Multibody models comparison: longitudinal dynamics

In order to compare the models responses in longitudinal direction, a straightforward acceleration manoeuvre has been applied, with a step-like driving torque of amplitude 16 Nm (about the maximum torque given by RUMBy) applied after 1 second.

Even if a small mismatch can be seen between the velocity profiles of Fig. 3.18, the differences between the models are evident by observing the accelerations of Fig. 3.19. As one can expect, the 5DOF and the 8DOF models have identical behaviours along x-axis, which is instead different from the one of the 14DOF model.

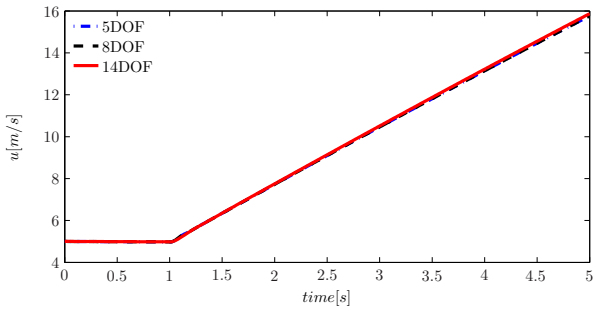

Figure 3.18: Longitudinal dynamics comparison - Velocities. The 5DOF and 8DOF present identical velocity profiles, that lightly differ from the 14DOF's one. The mismatch is more evident by analysing the acceleration profiles.

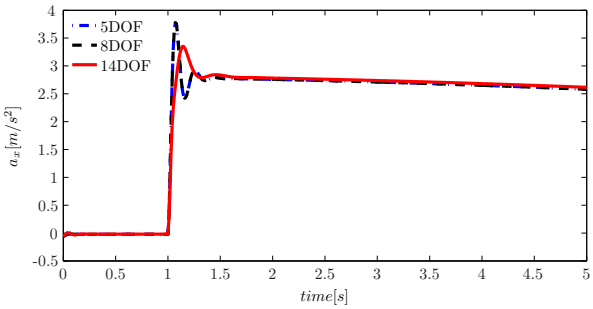

Figure 3.19: Longitudinal dynamics comparison - Accelerations. The 5DOF and 8DOF present identical acceleration profiles, that differ from the 14DOF.

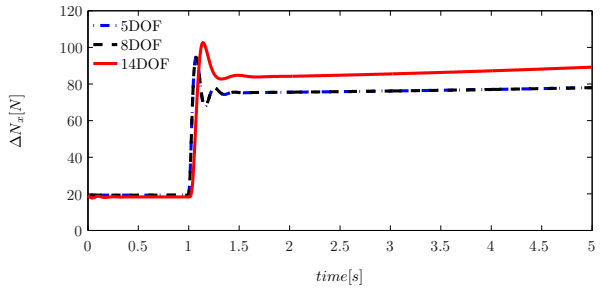

Figure 3.20: Longitudinal dynamics comparison - Load transfers. The CoM positions are still in 5DOF and 8DOF models, while change during the motion in 14DOF model because of pitch motion and tyres deflection: this introduces an additional load transfer that affect the whole longitudinal dynamics.

This distinction can be explained as follows. The 14DOF model presents also pitching motion and tyres vertical deflection, that change the Centre of Mass position when longitudinal acceleration occurs: consequently, the CoM motion introduces an additional load transfer -from the front to the rear axles- that is not present in the other two models. Fig. 3.20 shows the load transfers along x-axis computed for the three models. Because of the previous cited reasons, the 14DOF model presents a larger load transfer w.r.t. the one of the 5DOF and 8DOF models, allowing the transmission to the road of larger forces that justifies the differences in acceleration and velocity profiles.

Multibody models comparison: lateral dynamics

In order to compare the models lateral responses a step-like steering angle with amplitude 0.05 rads is applied after 1 seconds, while the longitudinal velocity is maintained constant at 5 m/s during the whole manoeuvre.

Fig. 3.21 shows the trajectories covered by the Centres of Mass of the three multibody models: a large mismatch is evident between the 5DOF and the other two models, which anyway present differing behaviours. The characteristic behaviour of the bicycle model is due to the fact that the tyres are collapsed in the vehicle middle line: firstly, it does not present lateral load transfers and, moreover, some components of velocity of the contact points are neglected, remarkably affecting the slips.

The small differences between the trajectories of the 8DOF and the 14DOF models are due to the 14DOF pitch motion and tyre deflection. Because of these motions, the CoM position change w.r.t. the chassis and this explains

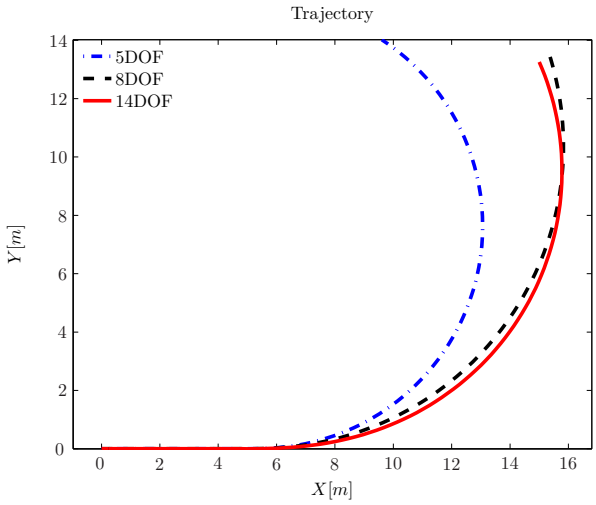

Figure 3.21: Lateral dynamics comparison - Trajectories. The bicycle model does not present lateral load transfer and has different slips, therefore its CoM assumes a trajectory completely different w.r.t. the other two models.

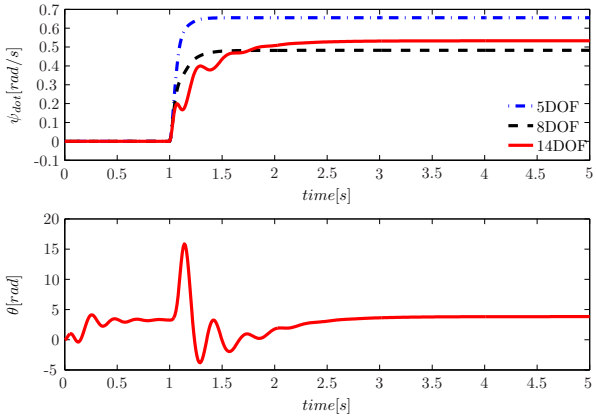

Figure 3.22: Lateral dynamics comparison - Yaw rates. The differing behaviours of 8DOF and 14DOF models are due the pitch motion of the latter model (*bottom plot*), that affects the yaw rate, the lateral load transfers and, consequently, the trajectory.

the mismatch in the trajectories. This statement is further demonstrated by Fig. 3.22, that shows the yaw rate profiles (*top*) and the 14DOF pitch angle (*bottom*). By focusing on the 14DOF model, it is evident that the

oscillations in the yaw rate coincide with those of the pitch angle (when the turn manoeuvre starts), causing the differences between the trajectories.

Multibody models comparison: combined dynamics

The differences between the models are even more evident if both longitudinal and lateral dynamics are excited. This goal is achieved by applying step-like profiles to both steering angle (amplitude 0.1 rads) and torque (amplitude 16 Nm), starting after 1 second.

Fig. 3.23 shows the trajectories covered by the Centres of Mass of the three models: as expected, the combined effect of longitudinal and lateral dynamics contributes to have three different paths. This is evident also by observing the yaw rate profiles of Fig. 3.24: the introduction of roll and pitch motions affect the lateral dynamics, decreasing the yaw rate that the model can assume. Also the velocity profiles of Fig. 3.25 present a combination of the previously discussed effects: the 14DOF is subject to an additional longitudinal load transfer (due to pitch motion) that increases the efficiency of the tyre-ground longitudinal forces transmission, explaining then the different slope of its velocity profile.

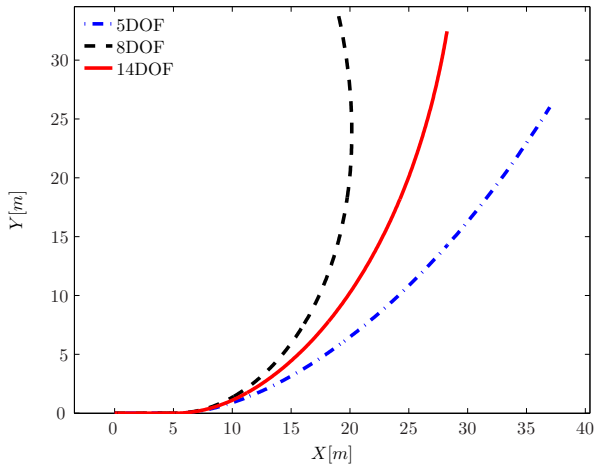

Figure 3.23: Combined dynamics comparison - Trajectories.

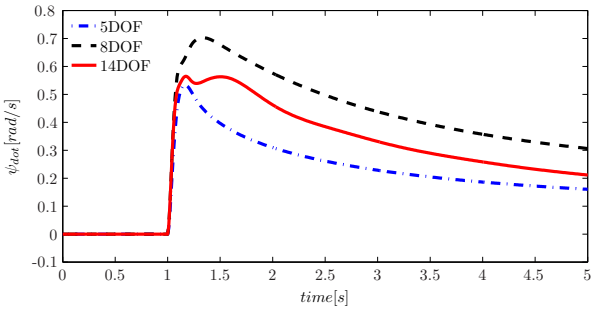

Figure 3.24: Combined dynamics comparison - Yaw rates.

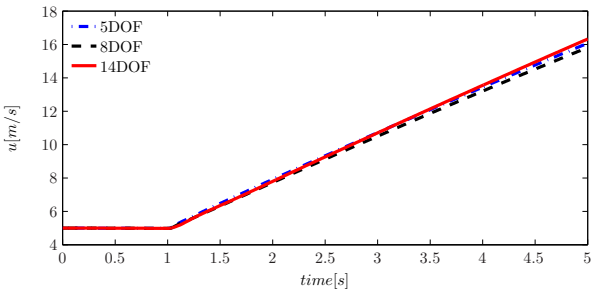

Figure 3.25: Combined dynamics comparison - Longitudinal velocities.

Chapter 4

Identification and Validation

Several models representing the vehicle and its subsystems have been presented in Chapter 3. A model becomes useful just if it is well identified, i.e. if the values of the parameters appearing in the model are known with a sufficient precision. Two methods can be used to know the parameters values: measurement and estimation. In § 4.1 both the approaches are presented and discussed, with examples about RUMBy and Kanon. Moreover, once a model has been identified, it must be validated, in order to verify if it accurately represents the actual system. § 4.2 presents a couple of approaches for the validation, in both time and frequency domains, of a model representing the Kanon roll motion.

The models described in Chapter 3 are very powerful tools for the investigation of a system. A mathematical representation of the system allows the estimation of its variables, the prediction of its behaviour or the synthesis of specific control strategies. Nevertheless, in order to have a mathematical model that correctly represents a dynamic system, it is necessary to know the values of the parameters appearing in the model itself. In mechanical systems, like vehicles, there are inertial and geometric variables, elastic constants, friction coefficients and so on.

The word "identification" collects all those activities oriented at the evaluation of such parameters. Two ways are available for the identification of a system: the direct **measurement** and the **estimation**. Several system parameters can commonly be measured in laboratory by means of purpose-made test benches (*e.g.* geometric parameters, mass, inertia, suspension data, etc.),

but some parameters cannot be directly measured (*e.g.* the tyres data): in such a case it is necessary to estimate them. The estimation activity consists in the computation -using recursive methods if the identification has to be done in real-time- of the parameters values that give the best match between the behaviours of the system and of a simplified mathematical model. Indeed the behaviour of the system is usually defined based on a subset of its state variables. Both the approaches have been studied, and some examples are discussed in § 4.1. In particular, four test-benches for the measurement of RUMBy's parameters are presented in § 4.1.1, while § 4.1.2 discusses a parameter estimation campaign done for Kanon.

Once the model is available and its parameters have been identified, it must be verified with information from the real system: this process is known as "validation". The necessary information can consist of a-priori knowledge of the system, measured data and experience of the user with the model (Ljung , 1999). In general terms, a model can be considered validated when it satisfies the requirements for which it was developed. The most common method of validation consists of the comparison of the model and system responses, subject to the same measured inputs, and the responses can be compared with different methods (qualitative or quantitative) and criteria (time and frequency domains). The validation campaign of a roll dynamics model representing the Kanon dynamics is discussed in § 4.2, carried out in both time and frequency domains.

4.1 Parameters Identification

The models described in Chapter 3 are so-called "parametric models", that give the relationship between the physical data of the system and its parameters. In order to achieve a good matching between the actual system and its model, the value of the parameters must be derived. The word "identification" collects all those activities aiming at the evaluation of such parameters, and can be achieved in two ways:

- **Measurement** - Several system static parameters can be measured in laboratory, by means of purpose-made test benches (*e.g.* geometric parameters, mass, inertia, suspension data, etc.).

- **Estimation** - Some parameters however cannot be directly measured, and their derivation is carried out using measured inputs and outputs signals together with suitable parameters estimation methods.

Both the approaches have been applied to identify the parameters of the vehicles RUMBy and Kanon. In particular, four test benches have been designed and built for the vehicle RUMBy, in order to respectively measure:

1. the mass and the Centre of Mass positions;
2. the principal moments of inertia w.r.t. a body fixed frame;
3. the suspensions stiffness and damping coefficient;
4. the relation between the steering signal and the front wheel steering angle.

An accurate description of each test bench is given in § 4.1.1, focusing on the working principles and the adopted instrumentation.

For vehicle Kanon the main parameters (mass, inertia, etc.) were instead known a-priori, while no information were available about some data as rolling resistance, tyres parameters and roll dynamics. Since the construction of custom test benches was not possible, a large set of standard manoeuvres oriented to the estimation of the vehicle parameters have been executed and processed. This work constitutes the main topic of a recent publication (Zendri et al., 2010) and is discussed in detail in § 4.1.2.

4.1.1 Parameters Measurement

In the last years the development of test benches for the measurement of vehicles characteristic parameters has been the subject of several studies. Strong efforts have been made, for instance, to produce facilities that allow the measurement of the moment of inertia tensor (Heydinger et al., 1995, Doniselli et al., 2003) or the tyre-ground interaction (Schmeitz et al., 2005, Potts , 2007). This approach often presents a challenge due to the need of handle an object (the vehicle) weighting even some tones. Fortunately the reduced size of RUMBy has facilitated the design and set up of the following test benches.

Centre of Mass positions

During the vehicle modelling, very important parameters are the mass and Centre of Mass positions. The reason of such significance is easily recognizable: the equations of motions mostly depend on those parameters and is then fundamental to know their values. Therefore the test bench represented in Fig. 4.1 has been designed for their measurement.

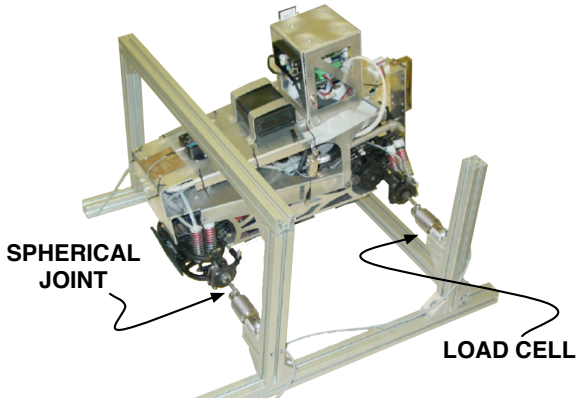

Figure 4.1: Bench for the measurement of the CoM positions. The hubs are linked to 4 load cells by means of spherical joints: measuring the weight acting at each cell, the total mass and the position of the CoM can be derived.

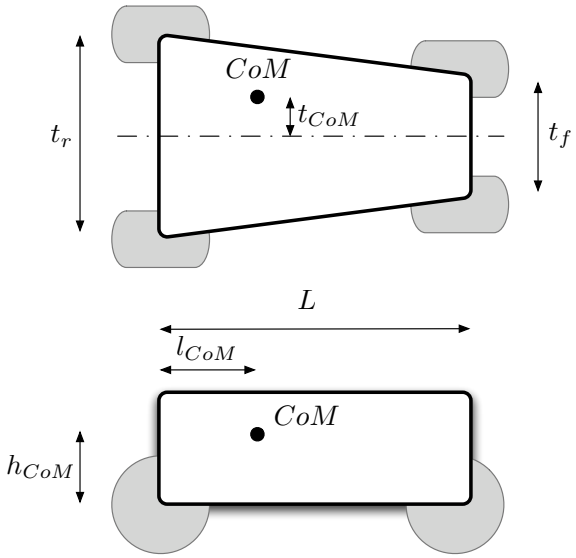

Figure 4.2: Schematics of the CoM positions. The positions of the sprung mass CoM are computed w.r.t. a chassis-fixed frame of reference: the computation of the whole vehicle Centre of Mass becomes consequently immediate.

By means of four load cells the weight F_{ij} acting on each wheel hub is measured. The sum of the measured loads gives the vehicle total mass

$$mg = F_{rf} + F_{lf} + F_{rr} + F_{lr} \tag{4.1}$$

while the load distribution depends on the CoM positions, which can be easily derived. In particular, by measuring the loads with the vehicle in horizontal configuration it is possible to compute the CoM positions l_{CoM} and t_{CoM} in the plane (Fig. 4.2). By forward tilting the vehicle of an angle α a longitudinal load transfer occurs depending on the CoM height h_{CoM}, which can be then computed by (4.4).

$$l_{CoM} = \frac{(F_{rf} + F_{lf})\, L}{mg} \tag{4.2}$$

$$t_{CoM} = \frac{t_f\,(F_{lf} - F_{rf}) + t_r\,(F_{lr} - F_{rr})}{2mg} \tag{4.3}$$

$$h_{CoM} = \left(\frac{L\,(F_{lf} + F_{rf})}{mg} - l_{CoM}\right)\frac{1}{\tan\alpha} \tag{4.4}$$

Moments of inertia

Another set of relevant parameters is constituted by the moments of inertia. In the Mechatronics laboratory, the three-wire torsion pendulum represented in Fig. 4.3 has been built, for the evaluation of the RUMBy moments of inertia. The working concept of the test bench is very simple: by perturbing the pendulum around the vertical axis, a harmonic oscillation is introduced, with natural frequency that depends on the moment of inertia w.r.t. that axis. For the vehicle RUMBy, a mechanical support has been designed in order to simplify the vehicle positioning, so that to study the inertia w.r.t. each desired axis. The oscillation frequency has been instead measured using a wireless accelerometer installed on the vehicle.

In order to derive the equation that links the oscillation frequency to the moment of inertia, the Lagrange approach can used. The following hypothesis are assumed:

- symmetry of the system about the vertical axis;
- infinite stiffness and equal length for each wire;
- Centre of Mass of the system coinciding with the spin axis.

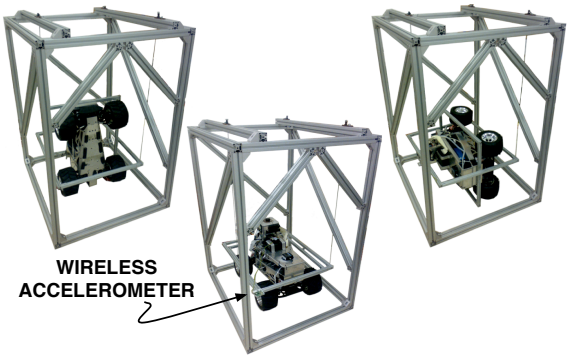

Figure 4.3: The 3-wires torsion pendulum. The frequency of oscillation around the vertical axis depends on the moment of inertia w.r.t. the same axis. By opportunely placing the vehicle on the pendulum and measuring the oscillation frequency, the moment of inertia tensor can be derived.

By referring to the schematics of Fig. 4.4, it can be written that the plate height h depends on its rotation as follows

$$h = L\,(1 - \cos\theta) \tag{4.5}$$

that, by assuming the small oscillation hypothesis, can be linearized as

$$h = L\frac{\theta^2}{2} \tag{4.6}$$

From Fig. 4.4 it is evident that the rotation can be formulated as

$$\varphi\ r = L\ \theta \tag{4.7}$$

which can be substituted in (4.6) to obtain the following formulation for the vertical motion:

$$h = \frac{r^2}{2L}\ \varphi^2 \tag{4.8}$$

Consequently it is possible to compute the potential energy due to the height

$$U = mg\frac{r^2}{2L}\ \varphi^2 \tag{4.9}$$

and the kinetic energy due to the rotation

$$T = \frac{1}{2}I\dot{\varphi}^2 \tag{4.10}$$

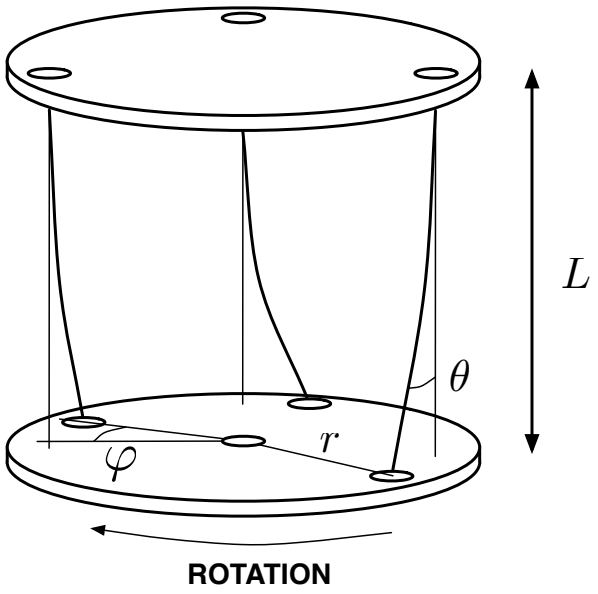

Figure 4.4: Schematics of the 3-wires torsion pendulum. The derivation of the equation is based on the linearization of the equation of motion, computed by means of the Lagrange method.

It is then possible to compute the Lagrangian polynomial and derive it, in order to obtain the system equation of motion

$$I\ddot{\varphi} = \frac{mgr^2}{L}\varphi \tag{4.11}$$

It is evident that (4.11) coincides with the equation of a harmonic oscillator with the following natural frequency

$$\omega_n = \sqrt{\frac{mgr^2}{I\ L}} \tag{4.12}$$

which can be inverted in order to compute the moment of inertia once the oscillation frequency is measured. It is worth noting that some of the hypothesis above described can be relaxed, and in particular the one concerning the system CoM position. It has to be said that a position outside the spin axis introduces additional vibration modes. Nevertheless the small oscillation assumption allows to neglect such undesired motions, and the moment of inertia

can be computed as follows:

$$I = \frac{mg\left(r^2 - d^2\right)}{L\omega_n^2} \tag{4.13}$$

where d is the distance between the spin axis and the system Centre of Mass.

Suspension parameters

RUMBy is equipped with four independent suspensions, each one with two oil shock-absorbers. Obviously the characteristics of those suspensions are very influent on the sprung mass motion, specially in models that include roll motion. Therefore a custom test bench has been designed for the evaluation of the suspensions parameters (Fig. 4.5). An aluminium frame constitutes the system, on which are fixed the electric motor that moves the crank gear (for the suspension solicitation) and the instruments for the measurement of the load F_s (a load cell) and of the displacement x (a laser triangulation system).

With such a system several kinds of tests can be done in order to identify the suspension parameters, even depending on the model adopted for their representation. By assuming a spring-damper linear model like the following

$$F_s = Kx + C\dot{x} \tag{4.14}$$

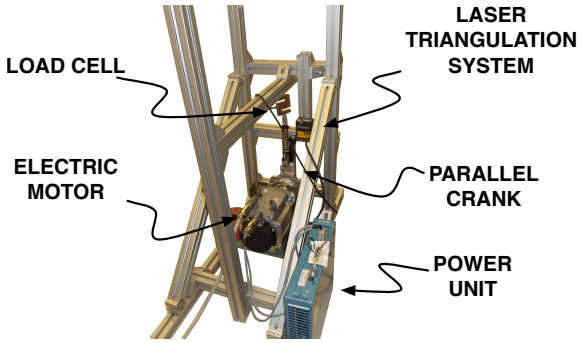

Figure 4.5: Bench for the suspensions parameters identification. The motor (actuator) moves the parallel crank, which forces the deflection of the suspension. Measuring the suspension resistance (with the load cell) and deflection (with the laser triangulation system) at different excitation frequencies, the suspension stiffness and damping coefficient can be estimated.

two tests are particularly interesting: static analysis and frequency sweep. The first one consists in applying quasi-static displacements, in order to evaluate the stiffness of the spring, and the hysteresis due to the damper. The second test aims instead at imposing a sinusoidal displacement, with a linearly increasing frequency, in order to cover the interesting range of frequencies (about 0-10 Hz) the suspension works on. This tests allows to determine the damping coefficient and the mismatch between the actual and the modelled (linear) behaviour of the suspension.

Steering system

As explained in § 3.3.2, the RUMBy steering servomotor is linked to the wheels by means of a complex kinematic chain that comprises also the suspensions, thus an accurate study of the system is necessary. Consequently, the test bench shown in Fig. 4.6 has been designed, which allows to evaluate the relation between the servo-control signal and the projection on the ground of the steering angle, depending on the suspensions configuration.

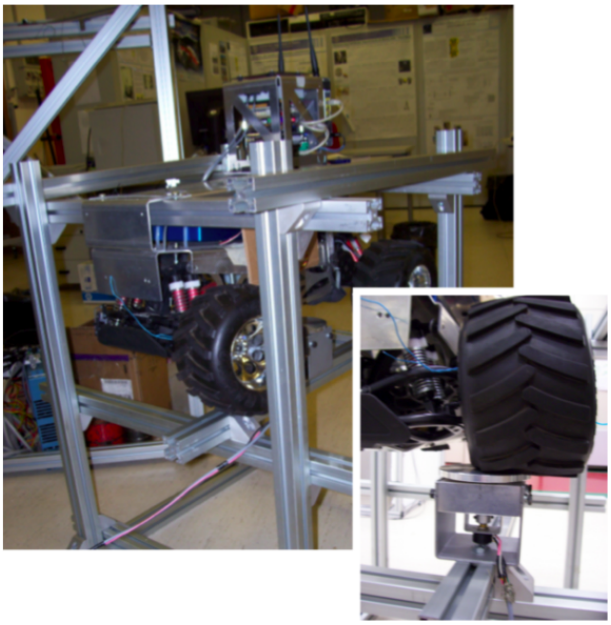

Figure 4.6: Bench for the identification of the steering chain. The projection on the ground of the steering angle is measured with a potentiometer for different suspension configurations, in order to experimentally verify the kinematic model described in § 3.3.2.

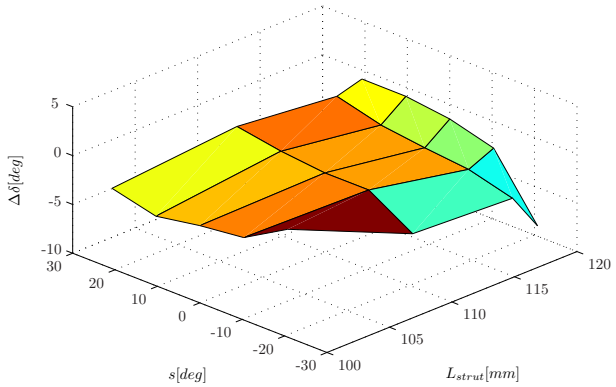

Figure 4.7: Steering angle error. Difference between the theoretical steering angle, computed with the model of § 3.3.2, and the experimental values measured with the purpose-made test bench.

In such a system, the tyre leans against a rotating surface and the suspension can be fixed in a chosen configuration: in this way it is possible to apply a rotation to the servomotor and measure the rotation of the supporting surface (by means of a potentiometer), which coincides with the steering angle. The bench allowed to verify the efficiency of the model discussed in § 3.3.2, and a consistent mismatch has been identified: Fig. 4.7 shows the steering angle error, *i.e.* the difference between the measured angles and the values computed with the model. It has been seen that the differences are due to the tyre deflection, which was neglected in the mathematical model and affects the projection of the angle on the ground: such a difference constitutes then a relevant phenomena, which has been taken in to account in successive modelling activities.

4.1.2 Parameters Estimation

In case that a certain parameter (or set of parameters) can not be measured directly by means of a purpose-made test bench its value has to be estimated. The idea of such an approach is very simple: applying a certain set of known inputs to the actual vehicle (acceleration, deceleration, steering) the kinematic variables obtained in the manoeuvre are measured. Applying the same set of inputs to a simplified mathematical model, it is possible to simulate the same kinematic variables and, finally, use an optimisation method for the estimation of the model parameters that give the best match between real and simulated

variables.

Vehicle parameters identification is a very active research field, with several contributions proposed by both companies and research institutes, especially for what concerns the tyre-ground interaction. Both batch (*i.e.* off-line) and recursive (*i.e.* on-line) methods can be adopted. For example, recursive methods are used in (Russo et al., 2000) in form of an Extended Kalman Filter, or in (Wang et al., 2004) as a switching Recursive Least-Square (RLS) algorithm for tyre-ground friction estimation. In (Wesemeier and Isermann , 2008), the identification of the bicycle model is carried out with RLS; in (Arkan et al., 2008), the same problem is tackled by using batch methods based on prediction-error minimisation (PEM).

In this section, an identification activity carried out for the vehicle Kanon is discussed: the work aims at estimating the parameters of a representative 8DOF model like the one described in § 3.2.2. As explained, some vehicle parameters were known a-priori, thus the identification activity discusses the estimation of:

1. the tyre rolling resistance;
2. the tyre driving stiffness;
3. the tyre cornering stiffness;
4. the parameters appearing in the roll dynamics equation (inertia and equivalent stiffness and damping).

Even if the work concerns an off-line estimation, a recursive method has been adopted for the identification of driving and cornering stiffness'. Such parameters can change while driving, and their values could be of interest for the synthesis of anti-skid controls. The estimate of each of these parameters is discussed in the following sections, with emphasis on the adopted equations and the achieved results.

Experimental Setup

As already introduced, the parameters estimation activity discussed in this section is referred to the experimental vehicle Kanon, that has been described in § 2.2. Nonetheless, it is worth remind some crucial aspects of the experimental setup.

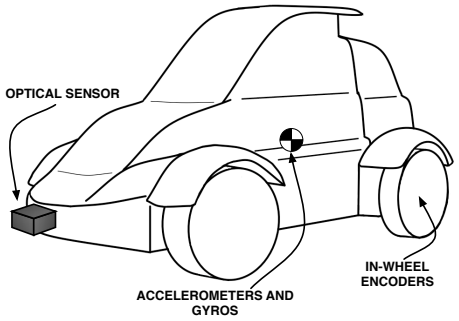

Figure 4.8: Sensors position on Kanon. The sensors on the vehicle measure some kinematic variables. The signals from the optical sensors are projected in the vehicle CoM in order to maintain the consistency with the signals from accelerometers and gyros.

First of all, the vehicle is equipped with some sensors as shown in Fig. 4.8, that measure kinematic variables. About such measures, some assumptions have been done, that are:

- accelerometers for the measurement of longitudinal and lateral accelerations (a_x, a_y) are fixed to the sprung mass and their positions coincide with the vehicle Centre of Mass;
- gyros that measure yaw rate (ψ_{dot}) and roll rate (ϕ_{dot}) are fixed to the sprung mass and their positions coincide with the vehicle CoM;
- DATRON optical sensor is fixed on the front of the vehicle and measures longitudinal and lateral velocities (u, v) and sideslip angle (λ), that are however projected in the vehicle CoM in order to maintain consistency with the other signals.

Moreover, also the input signals (torques and steering angle) are measured. The importance of this aspect will be clear in the next sections, since the identification activity of some parameters needs the knowledge of the input values.

Finally, the identification of some parameters requires the execution of manoeuvres with constant inputs or states (*e.g.* longitudinal velocity) in order to simplify the motion and, consequently, the adopted equations. For this reason, the dSpace controller installed on Kanon becomes particularly useful, since it allows to apply controlled inputs (either feedforward or feedback).

Rolling Resistance

During steady acceleration manoeuvres with known constant input torque, a difference between the acceleration expected from the equation of longitudinal dynamics and the real one generally occurs: such a behaviour is due to friction terms such as rolling resistance, drag force and other dissipative phenomena.

Applying a total driving torque T_{tot} to the wheels, the expected longitudinal acceleration a_x^* of the vehicle should be:

$$a_x^* = \frac{\sum F_x}{M} = \frac{T_{tot}}{rM} \tag{4.15}$$

where r is the tyre radius (supposed constant) and M is the vehicle total mass. However, the above does not consider the rolling resistance and drag force which largely affects the longitudinal acceleration as shown in Fig. 4.9.

To correctly identify these dissipative phenomena, the wheel dynamic equation (3.48) can be solved for longitudinal forces F, which are then substituted in longitudinal dynamics equation (3.44), simplified for straight motion. Therefore, the resistant torque T_{roll} can be evaluated as

$$T_{roll} = \frac{1}{4}\left(T_{tot} - Ma_x r - 4I_w\dot{\omega}\right) \tag{4.16}$$

where I_w is the generic wheel inertia.

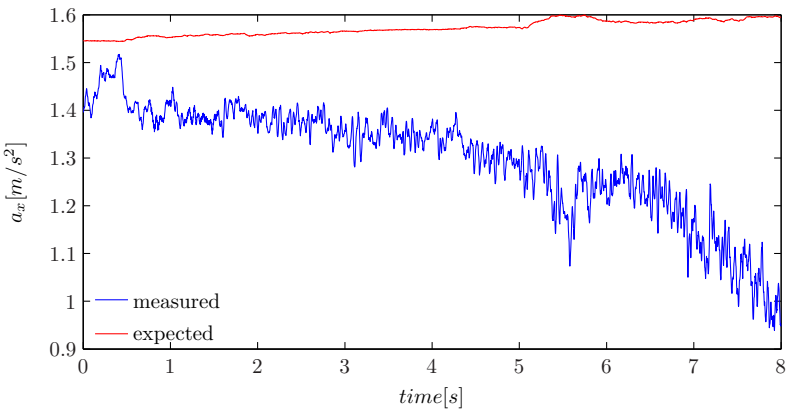

Figure 4.9: Expected and measured acceleration. Dissipative phenomena (*e.g.* drag force and tyre rolling resistance) are responsible of the mismatch between the expected and the actual behaviour.

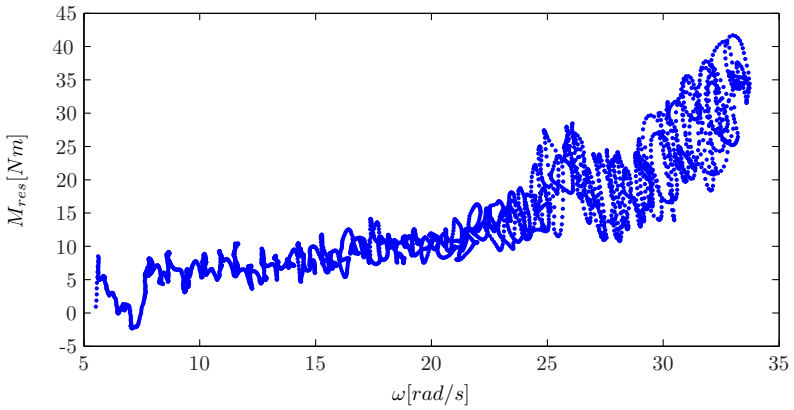

Figure 4.10: Resistant Torque vs Wheel velocity. In spite of the dispersion (due to measures noise) at high velocity, the quadratic dependance of the resistant torque from the velocity can be seen.

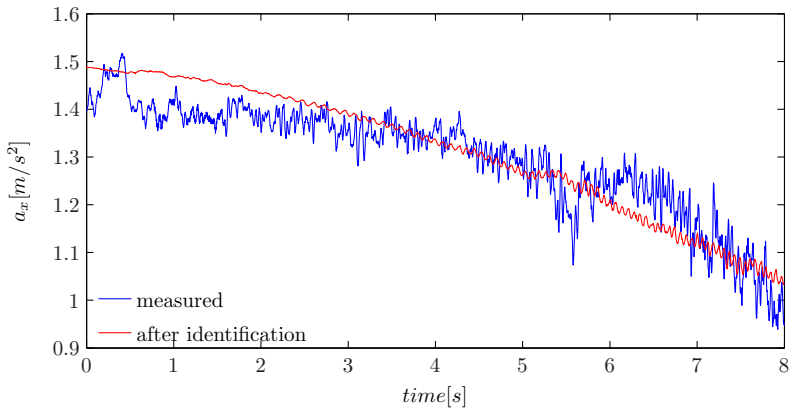

Figure 4.11: Measured and estimated acceleration after identification. After the identification of the parameters T_0 and k_r, the estimated acceleration matches very well with the measured one.

In Fig. 4.10 the estimated resistant torque versus the wheel spinning ratio is shown. It is evident that such a dependance can be written as a quadratic function of wheel spin

$$T_{roll} = T_0 + k_r\omega^2, \tag{4.17}$$

By applying a least square fitting method to the previous equation for a set

of straight line constant torque manoeuvres the parameters T_0 and k_r can be estimated. For the adopted data set, the estimated values are $T_0 = 12\text{Nm}$ and $k_r = 0.05\frac{\text{Nmsec}^2}{\text{rad}^2}$. Fig. 4.11 shows the good match of the estimated acceleration with identified parameters.

Driving Stiffness

It has been shown in Chapter 3 that for small slips the longitudinal force at the tyre ground contact point is linearly dependent on vertical load and slip:

$$F_x = k_\kappa N \kappa \tag{4.18}$$

where k_κ is the driving stiffness, N is the normal load acting at the tyre-ground contact point and κ is the longitudinal slip ratio.

Introducing (4.18) into (4.16) and neglecting the wheel inertia, the vehicle longitudinal dynamics becomes:

$$Ma_x + \frac{4T_{roll}}{r} = k_\kappa N_r \kappa_r \tag{4.19}$$

Applying the RLS method to (4.19) the driving stiffness can be estimated. The results for a steady acceleration is shown in the top plot of Fig. 4.12: the estimated value is $k_\kappa = 9.1$.

Cornering Stiffness

The cornering stiffness greatly affects the vehicle lateral response and it can be identified for a steady state cornering manoeuvre (at constant speed V), provided that the tyre lateral engagement is low (small side slip angles). The linearized lateral dynamics of a single track model is:

$$MV\left(\frac{d\lambda}{dt} + \psi_{dot}\right) = 2F_{y,f} + 2F_{y,r} \tag{4.20}$$

where λ is the sideslip angle referred to the vehicle CoM. Substituting the linear force model (3.26), the equation becomes:

$$\begin{aligned} u\left(\frac{d\lambda}{dt} + \psi_{dot}\right) &= \kappa_\lambda 2g\left[-\delta + \arctan\left(\frac{v + \psi_{dot} l_f}{u}\right)\right] \\ &\quad + \kappa_\lambda 2g \arctan\left(\frac{v - \psi_{dot} l_r}{u}\right) \end{aligned} \tag{4.21}$$

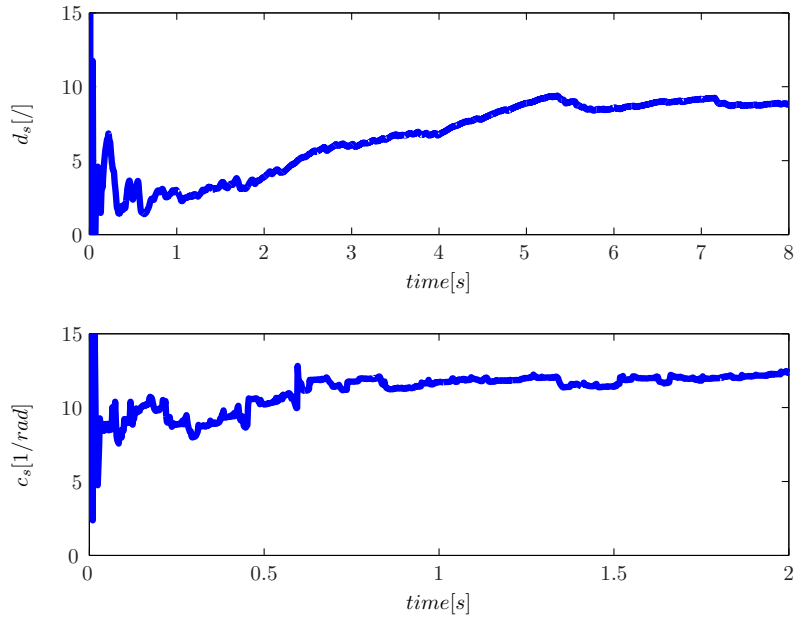

Figure 4.12: Driving (*top*) and cornering (*bottom*) stiffness' identified by RLS. A recursive approach has been preferred since the stiffness' depend on the soil properties, that could change during a manoeuvre. Nevertheless no variations are recognizable for the chosen dataset, and a good estimation is achieved in few iterations.

The RLS procedure can be applied to estimate the cornering stiffness k_λ, once the derivatives of the sideslip angles in (4.21) are numerically approximated. The RLS result is shown in the bottom plot of Fig. 4.12 and the estimated value for the cornering stiffness is $k_\lambda = 12\,\mathrm{rad}^{-1}$.

Roll Dynamics

The identification of the roll dynamics is based on a linear model of the roll motion obtained by rewriting (3.47) as follows:

$$I_x\ddot{\phi} + C_\phi\dot{\phi} + K_\phi\phi = Mh_{rc}a_{y,\mathrm{meas}} \tag{4.22}$$

with

$$C_\phi = \beta_f t_f^2 + \beta_r t_r^2\,, \qquad K_\phi = \kappa_f t_f^2 + \kappa_r t_r^2 \tag{4.23}$$

to represent the equivalent stiffness and damping coefficient, and where

$$a_{y,\mathrm{meas}} = -h_{rc}\ddot{\phi} + a_y\cos\phi + g\sin\phi + h_{rc}\sin\phi\cos\phi\psi_{dot}^2 \tag{4.24}$$

corresponds to the lateral acceleration measured by the onboard accelerometers. Note that (4.22) has been derived from (3.47) neglecting the additional forcing torque $-I_z \sin\phi \cos\phi \psi_{dot}^2$: the simplification is correct for small roll angles.

The unknown coefficients I_x, C_ϕ and K_ϕ in (4.22) are estimated with the simplified refined instrumental-variable method for continuous-time systems (Garnier and Liuping , 2008) applied to the experimental measurements of an automatic steer-sweep manoeuvre: a brief description of the procedure is discussed in Appendix C. The measured lateral acceleration $a_{y,\text{meas}}$ is adopted as input and the roll rate ϕ_{dot} as output variable. The identified parameters are: $I_x = 95$ kg m^2, $C_\phi = 1580$ N m s/rad and $K_\phi = 28600$ N m/rad. Fig. 4.13 shows the comparison between the measured and the simulated roll rate, with the data set adopted for the identification: a good matching is achieved, with a Root Mean Squared Error (RMSE) of about 0.02 rad/sec.

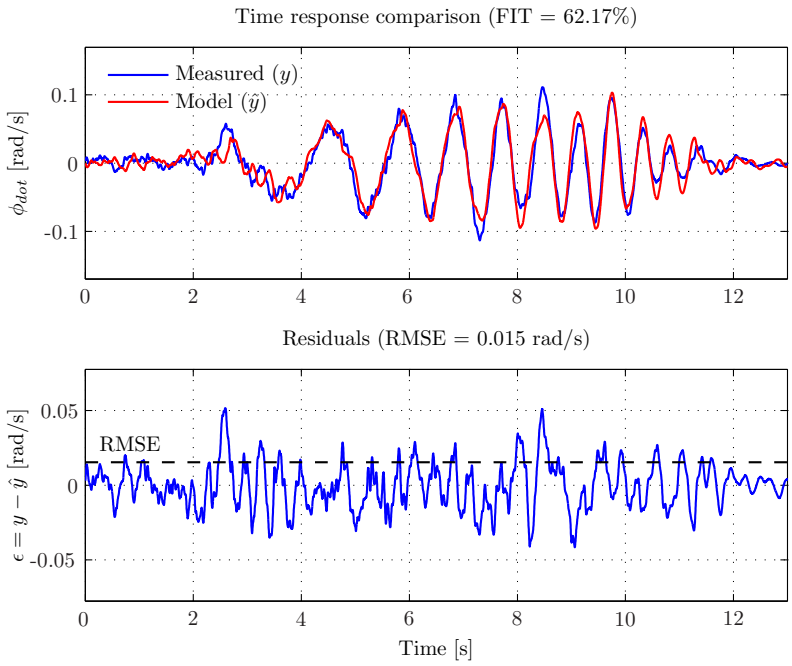

Figure 4.13: Roll rate comparison (*top*) and error (*bottom*). In spite of the introduced simplifications, the model matches the measured profile very well, with a RMSE of about 0.02rad/sec.

4.2 Validation

Once the parameters have been identified the model must be validated, *e.g.* it has to be verified with information from the actual system. Several methods are available for system validation (Ljung , 1999), concerning both time and frequency responses.

Likewise the estimate activity discussed in § 4.1.2, the validation presented in this section is referred to the work done for (Zendri et al., 2010). Two validation methods have been adopted: a qualitative method based on visual comparison of the model and experimental responses (in both time and frequency domains), and a quantitative method based on the statistical analysis of the model residuals (in frequency domain). The validation procedures have been applied on a different dataset from the one used for the model identification (cross-validation), thus overcoming the possible chance of "over-fitting" the measurements with an over-parameterized model.

4.2.1 Time Response Analysis

According to the dynamic variables to be validated, suitable driving manoeuvres have to be defined so that the variables are sufficiently excited (Kiencke and Nielsen , 2000). The measured variables are then compared with the corresponding outputs from the model, in order to determine if the model is sufficiently accurate for the purpose it has been developed for. For the validation discussed in this section, a lane-change manoeuvre has been used: such a manoeuvre excites all the interesting dynamics, allowing the comparison of both longitudinal and lateral dynamics variables.

Longitudinal acceleration and velocity profiles are reported in Fig. 4.14. A good matching can be observed especially for the acceleration trends except when braking occurs for (at about 13 seconds) since it was not simulated (dissipative braking is not included in the model). The remaining small mismatch is due to pitch dynamics, which was not modelled but affects the measured longitudinal acceleration by partially introducing the gravitational acceleration component.

Lateral dynamics (yaw rate and roll rate) is instead considered in Fig. 4.15. In general, the model responses are in good agreement with the measured ones (especially yaw rate plot on the top). The experimental roll rate shows a marked fluctuation, which is due to the road unevenness, not present in the simulation. In fact the road test ground was a quasi-flat off road ground with sandy and stony surface.

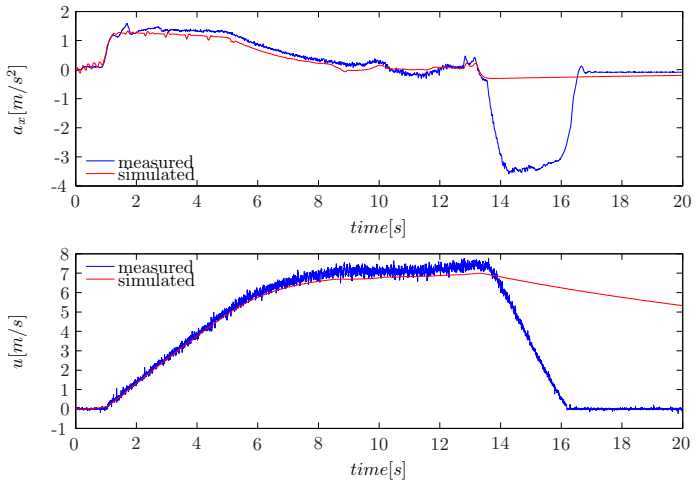

Figure 4.14: Time response comparison: longitudinal acceleration (*top*) and velocity (*bottom*). The model represents very well the vehicle longitudinal dynamics, except when braking occurs (about 13sec) since it is not simulated.

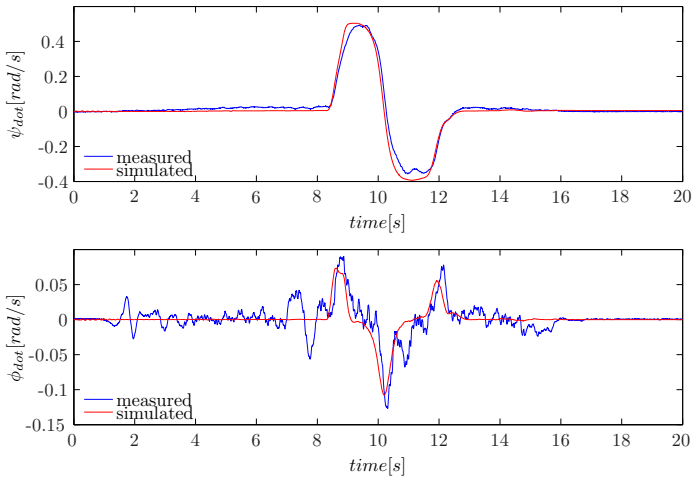

Figure 4.15: Time response comparison: yaw rate (*top*) and roll rate (*bottom*). Lateral dynamics is very well captured by the model, even if a mismatch due to neglected road unevenness can be seen in the roll rate profile.

4.2.2 Frequency Response Analysis

As for the time response analysis, the manoeuvres suitable for the frequency response analysis have to excite all the interesting variables. However, in this

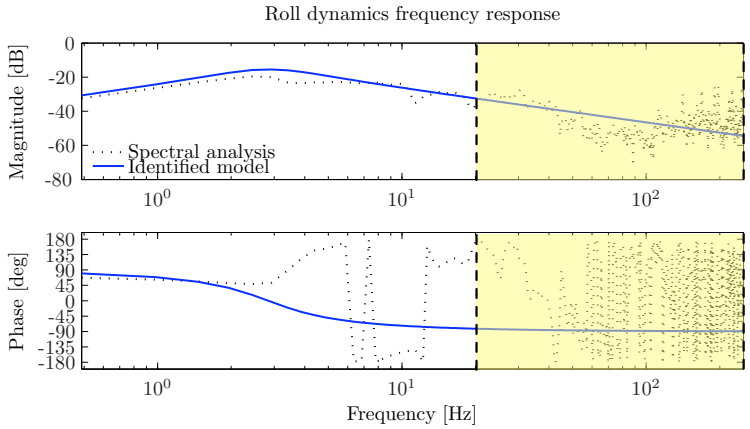

Figure 4.16: Roll dynamics frequency response. The system ETFE and the model transfer function are compared: the comparison is inconsistent over ≈ 20 Hz (highlighted spot), that is the upper frequency limit of the sweep-steer signal.

case the inputs applied to the system must also cover an enough wide range of frequencies. This section describes the validation in frequency domain of the vehicle roll dynamics, applied to the data measured during an automatic steer-sweep manoeuvre. Obviously, the validation procedures have been applied on a different dataset from the one used for the model identification.

As explained at the beginning of this section, two approaches have been used for the frequency response analysis: qualitative and quantitative method. The qualitative validation in frequency domain can be achieved by a visual comparison of the system and model frequency responses. Fig. 4.16 shows the frequency response of the roll dynamics (with input $a_{y,\text{meas}}$ and output ϕ_{dot}). The system response has been obtained by standard spectral analysis (Ljung , 1999), computing the Empirical Transfer Function Estimate (ETFE) of the measured data[1]. The model response profile has been instead drawn by directly using the identified model (4.22). Fig. 4.16 shows that the best matching is achieved in the very low frequency range, *i.e.* where the vehicle dynamics is most strongly excited. The high acquisition frequency (500 Hz)

[1]The ETFE is the ratio of the Fourier transforms of the output and input signals of a system. Since the measures are subject to a certain observation noise, the "true" input/output Fourier coefficient are not accessible and, then, only the "empirical" transfer function can be computed.

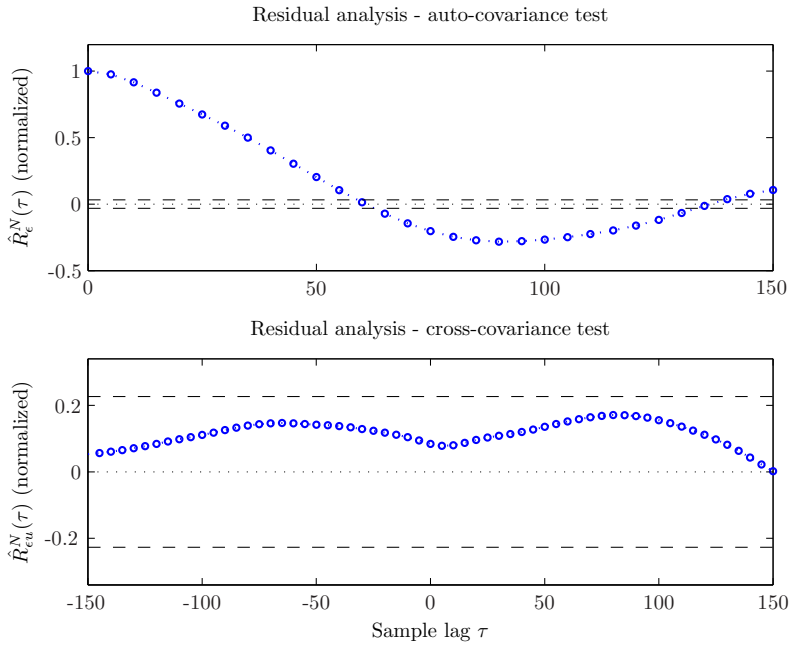

Figure 4.17: Residual analysis for the identified roll dynamics model - auto-correlation (*top*) and cross-correlation (*bottom*). The cross-correlation lies within the confidence interval, hence the model completely captures the system dynamics. On the contrary, the auto-correlation test is not passed, evidencing that the equivalent output disturbance in not accounted for in the model.

allows to draw the frequency response up to 250 Hz. Nevertheless the upper frequency limit of the sweep-steer signal is $\approx$ 20 Hz, then the frequency responses comparison is consistent up to such frequency.

As quantitative validation method, the residual analysis has been used (Ljung , 1999) - some details about residual analysis are discussed in Appendix D. Residuals $\epsilon(t)$ are differences between the predicted output from the model $\hat{y}(t)$ and the measured output $y(t)$ from the validation data set. In general, it is reasonable to assume that a model has been consistently estimated from measured data if it passes two tests:

1. Independence test - Demonstrates if the model is capable of reproducing the whole portion of the output $y(t)$ affected by the input $u(t)$ or, in other terms, if the residual error $\epsilon(t)$ is uncorrelated with $u(t)$.

2. Whiteness test - Shows if the model provides a correct prediction of the

equivalent disturbance affecting the output measurements, hence the residual error should be a white noise.

In residual analysis, the uncorrelation of ϵ with u and the whiteness of ϵ are checked by means of statistical hypothesis testings. When applied to the identified roll dynamics model, residual analysis yields the results shown in Fig. 4.17. Since the estimated cross-correlation function lies within the confidence interval, the independence test is passed, implying that the roll dynamics from $a_{y,\text{meas}}$ to ϕ has been completely captured by the model. On the contrary, the estimated auto-correlation function shows that the whiteness test is not passed: this result is not surprising, since the equivalent output disturbance is not accounted for in the proposed model.

Chapter 5

State Estimation

Control of a dynamic system requires reliable estimates of system state, in order to compute the best set of inputs that gives the desired response. Unfortunately, the complete state is not always measurable/observable. State estimation is based on the measurable quantities on-board acquired and determines the underlying behaviour of the system at any point in time. In this chapter the solutions adopted for the estimation of the RUMBy's state are discussed, from the measures analysis up to the sensor fusion.

From a mathematical point of view, a continuous dynamic system constitutes a mathematical model of a physical system, that interacts with the surrounding environment by means of two vectors of time-depending variables:

- the *input variables*, representing the external actions acting on the system, and
- the *output variables*, that describe the interesting behaviour of the system.

In other words, the system can be represented as shown in Fig. 5.1 and a cause-effect relation is there between the variables: the outputs evolution describes the system response to the applied set of inputs.

Nevertheless in the most cases this is not true, and the knowledge of the inputs at a certain time is not sufficient to know the outputs values at the same time. In these cases, a third vector of variables, termed *state variables*, is thus necessary in order to describe the internal system condition. The concept of *state* of a dynamic system refers to a minimum set of variables, known as *state*

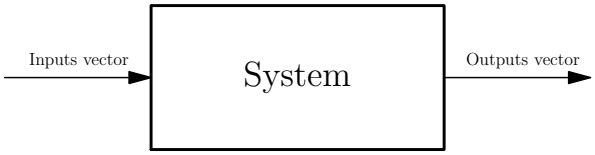

Figure 5.1: Schematics of a cause-effect system. The simplest way to represent a dynamical system is a cause-effect structure: no information are available about the internal situation of the system and it is treated as a black box.

variables, that fully describe the internal condition or status of the system at a given instant of time (Thaler and Brown , 1960).

Defining respectively $\boldsymbol{u}$, $\boldsymbol{x}$ and $\boldsymbol{y}$ the vectors of inputs, states and outputs, and with $\boldsymbol{f}(\cdot)$ and $\boldsymbol{g}(\cdot)$ two vectorial functions, a continuous dynamic system is constituted by the equations:

$$\dot{\boldsymbol{x}}(t) = \boldsymbol{f}(\boldsymbol{x}(t), \boldsymbol{u}(t), t) \tag{5.1}$$

$$\boldsymbol{y}(t) = \boldsymbol{g}(\boldsymbol{x}(t), \boldsymbol{u}(t), t) \tag{5.2}$$

The input-output link is thus divided in two parts, and described by two vectorial equations:

- a differential equation, termed *state equation*, that represents the relation between the inputs and the system internal condition;
- an algebraic equation, termed *output transformation*, that allows to determine the system output at a certain time based on the system input and internal condition.

Equations (5.1))-(5.2) constitute the so-called *state-space representation* of the system, which can be thus schematized as shown in Fig. 5.2.

The state-space representation given by (5.1)-(5.2) is the most generic one, valuable for any kind of continuous-time system. For the purpose of this work, it is advantageous to introduce a particular kind of dynamic systems: the linear discrete time-variant system.

$$\boldsymbol{x}_k = \boldsymbol{A}_k \boldsymbol{x}_{k-1} + \boldsymbol{B}_k \boldsymbol{u}_k + \boldsymbol{w}_k \tag{5.3}$$

$$\boldsymbol{y}_k = \boldsymbol{H}_k \boldsymbol{x}_k + \boldsymbol{v}_k \tag{5.4}$$

This formulation becomes particularly useful since it allows to describe linearized discretized systems, for which the state estimation algorithm has been designed.

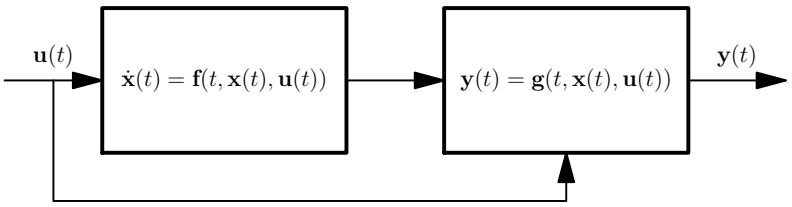

Figure 5.2: Schematics of a dynamic system in the state-space form. When the knowledge of the inputs at a certain time is not sufficient to know the outputs values at the same time, the system must be represented in the state-space form. The states represent the internal condition of the system, and the relation between inputs and output is divided in two parts: the state equation and the output transformation.

From an engineering point of view, knowledge about the system state could be interesting for at least two reasons:

- if it is necessary to know the state of a system in order to design a state-feedback controller (*e.g.* an electrical engineer needs to know the winding currents of a motor in order to control its position), and
- if it is necessary to know the states of a system because those states are interesting in their own right (*e.g.* an aerospace engineer might want to know the position of a satellite in order to more intelligently schedule future satellite works).

In order to know the state of a system it is convenient to equip the system with sensors that measure as many variables as possible. Unfortunately, the state of a system is not always measurable/observable: in such a case it becomes necessary to estimate it. State estimation aims at inferring the value of an interesting quantity from indirect, inaccurate and uncertain observations. State estimation theory was initially developed in the 1950s, and since then there have been a huge number of applications. Many state estimators can be found in literature, but the most known is undoubtedly the Kalman Filter (Kalman , 1960). The Kalman Filter is an efficient recursive procedure useful to combine noisy signals in order to estimate the behaviour of a system with uncertain dynamics. It is used in a wide range of engineering applications, from radar to computer vision, and is an important topic in control theory and control systems engineering.

This chapter describes the state estimation strategy created for the vehicle RUMBy. As explained in Chapter 2, the vehicle is equipped with several

sensors, of different nature, that measure kinematic variables. Anyone of the on-board sensors is nevertheless characterized by a set of problems, errors and operating limits: because of these constraints a particular strategy has been devised, that couples the Kalman Filter with another operation - the measures Preprocessing. In the following sections, the system architecture and its parts are described, focusing on the assumptions made and the equations formulated. The last section gives instead an example of vehicle state estimation, discussing the quality of the achieved experimental results.

5.1 System Architecture

RUMBy is fitted with some on-board sensors for the measurement of kinematic variables. Anyone of the vehicle sensors is subjected to a certain set of errors, depending on the nature of the sensor itself. Therefore, it becomes mandatory to develop strategies oriented to estimate the vehicle state based on the collected sensor signals.

Many strategies and approaches have been studied to estimate the state of the vehicle RUMBy, in terms of positions, attitude and velocities. The most interesting results have been achieved with the architecture shown in Fig. 5.3, which combines together the effects of Measures Preprocessing and Extended Kalman Filter.

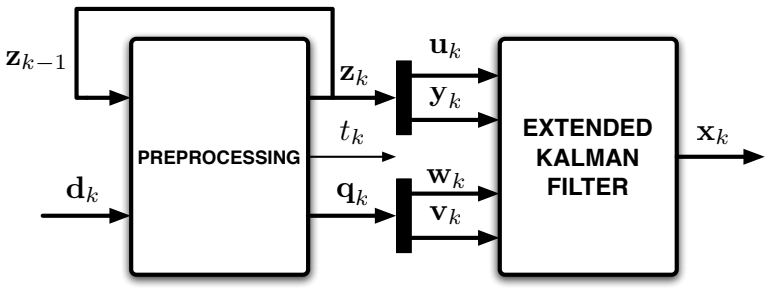

Figure 5.3: State estimation architecture. The state estimation is constituted by two main operations: the preprocessing and the Filter. The preprocessing aims at elaborating the measures in order to detect signal errors and improve the measures quality. The filter does instead the sensor fusion, necessary to estimate the state of the system.

As shown in Fig. 5.3, the architecture is split in two blocks, and the vectors represent respectively:

$\boldsymbol{d}_k$: raw data coming from sensors
$\boldsymbol{z}_k$: preprocessed data
t_k : current time
$\boldsymbol{q}_k$: reliability vector (standard deviations)
$\boldsymbol{u}_k$: filter inputs
$\boldsymbol{y}_k$: measures used by the filter
$\boldsymbol{w}_k$: process noise vector (standard deviations)
$\boldsymbol{v}_k$: measures noise vector (standard deviations)
$\boldsymbol{x}_k$: estimated states.

The system receives the raw data from the sensors and executes a first operation - **Preprocessing** - oriented to a re-computation of the measures and the evaluation of the measures reliability indexes. The reliability indexes are defined in terms of standard deviations, and constitute a vector collecting information about the quality of each measure. Once computed, these vector are divided in sub-vectors representing the **Kalman Filter** inputs, which fuses the data in order to estimate the interesting vehicle states.

A feedback architecture has been chosen for the Preprocessing for two reasons: a) the algorithm has to compare the data at a certain time-step with those of the previous time-step and b) some variables have to be numerically differentiated. The main advantage of this architecture is its flexibility: once the Preprocessing is designed, it can be coupled with different versions of the state estimator, depending on the set of measures and states of interest. The following sections discuss in detail the blocks of Preprocessing and Filtering.

5.2 Data Preprocessing

As introduced, the Preprocessing collects a set of operations oriented to:

1. the computation of the measures in terms of more significant variables;
2. the correction (if possible) of the errors affecting the measures;
3. the assignment of a reliability index, in terms of standard deviation, to each signal.

The goals of these operations may not not be so clear if described in this way, therefore let's discuss them in detail.

5.2.1 Measures re-computation

The first set of activities aims at re-computing the raw data in terms of more significant and understandable variables. The best example about this activity concerns the vehicle positions acquired from the GPS unit. The GPS VBOX measures geodetic latitude, longitude and altitude w.r.t. the WGS84 datum, a particular Conventional Terrain System that approximates the Earth as a rotational ellipsoid. Obviously, the raw information in terms of latitude-longitude-altitude are unusable. Therefore the Preprocessing re-computes the GPS information, in order to transform the measures in the trajectory computed w.r.t. a local frame of reference with the following characteristics:

- origin in the first acquired point:
- X-axis pointing to North;
- Z-axis pointing upward;
- Y-axis pointing consequently to West.

An example of this re-computation is shown in Fig. 5.4, referred to a repetitive manoeuvre along a triangular-like track. It is easy to see that latitude-longitude data are not immediately representative of vehicle position in space, while xyz trajectory is more understandable from a physical point of view and it is directly usable in digital maps.

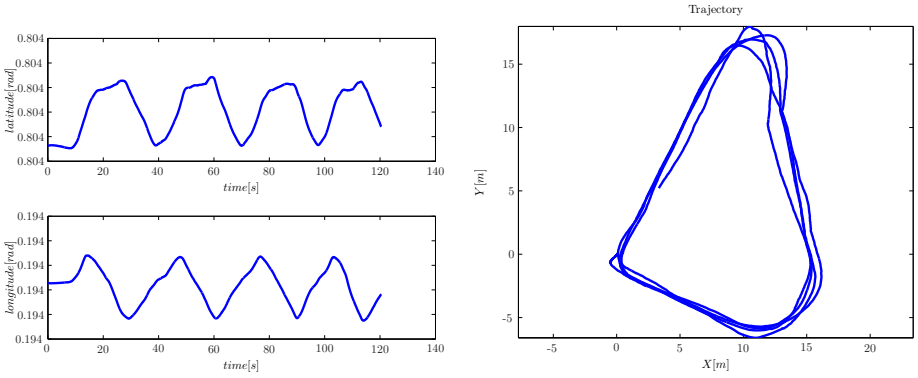

Figure 5.4: Example of measures re-computation - Acquisition referred to a repetitive manoeuvre along a triangular-like track. The latitude-longitude raw data (*left*) are hard to be interpreted, while the re-computed trajectory w.r.t. a local frame of reference (*right*) is immediately understandable.

Another example of measures re-computation concerns the data coming from the odometers, shown in Fig. 5.5. It has been explained that the on-board odometers are constituted by two gear wheels with 75 teeth, coupled with Hall effect sensors. The sensors send their signals to a counter board, which counts the number n of signal fronts any time it is queried. Obviously, since the counter board is queried with a fixed time-step, these signals are proportional to the wheels angular velocities. Naming Δt the counter board interrogation sample time, the equation for the computation of the angular velocities in [rad/s] becomes the following:

$$\omega_i = n_i \left(\frac{2\pi}{150}\right)\left(\frac{1}{\Delta t}\right) \tag{5.5}$$

where the subscript 'i' denotes the left or right wheel. For practical reasons, another computation is applied to these angular velocities, in order to evaluate their average value (*common-mode* value) and their half-difference (*differential-mode* value)

$$\omega_{CM} = \frac{\omega_r + \omega_l}{2}\,, \qquad \omega_{DM} = \frac{\omega_r - \omega_l}{2} \tag{5.6}$$

These new values are proportional, respectively, to the longitudinal velocity and the yaw rate, unless the slips, and thus more useful during the state estimation. Fig. 5.5 gives an example of this kind of re-computation.

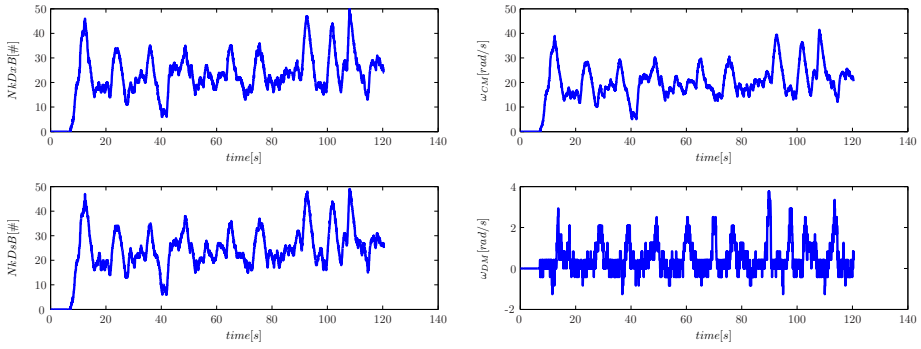

Figure 5.5: Example of measures re-computation - Acquisition referred to a repetitive manoeuvre along a triangular-like track. The odometers raw data (*left*) can be just qualitatively interpreted, while the re-computed angular velocities (*right*) are immediately understandable.

5.2.2 Errors correction

The purpose of this operation is to detect and (if possible) correct the errors that affect the measures and are due to the nature of the sensor. An example of errors correction is shown in Fig. 5.6. The figures refer to the yaw angle from the magnetometer and the heading angle from the GPS, acquired during a clockwise circular manoeuvre.

The first evident error concerns the sign of the measures. Since the vehicle moves in clockwise direction and the Z-axis points upward, the yaw and heading angles should decrease. Nevertheless, the heading angle (from GPS) increases: this phenomenon is due to an error in the VBOX firmware, that can be easily corrected by changing the sign of such a measure.

The second error is due to the periodic nature of the angular measures, that are defined w.r.t. the North and, respectively, in the range $[0,\ 2\pi]$ for the GPS and $[-\pi,\ \pi]$ for the magnetometers. Hence, when the vehicle crosses the North direction, jumps of amplitude 2π occur in both the angle measures. From a dynamic point of view, such jumps represent a singularity and have to be eliminated: this operation, termed "angles unwrap", represents an error correction and gives the results shown in Fig. 5.6(*right*).

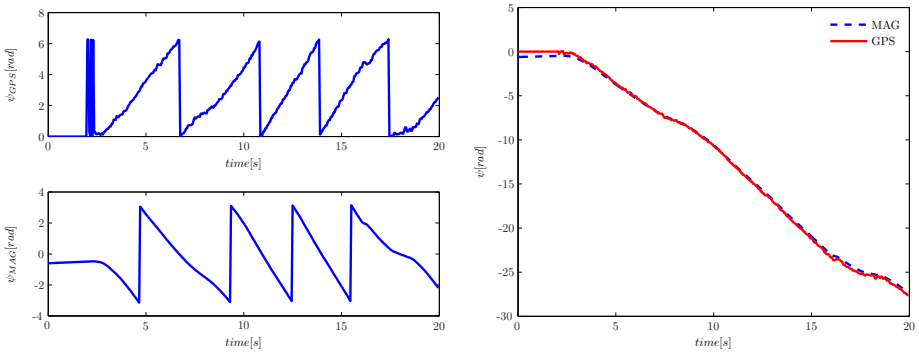

Figure 5.6: Example of measures re-computation - Acquisition referred to a repetitive manoeuvre along a triangular-like track. The raw yaw angles from magnetometers and GPS (*left*) present opposite profiles and jumps that have to be corrected (*right*) in order to make the measures mutually consistent and w.r.t. the vehicle dynamics.

5.2.3 Reliability index

Unfortunately only few errors affecting the measures can be directly corrected. In order to reduce their effect on the data fusion, the Preprocessing computes

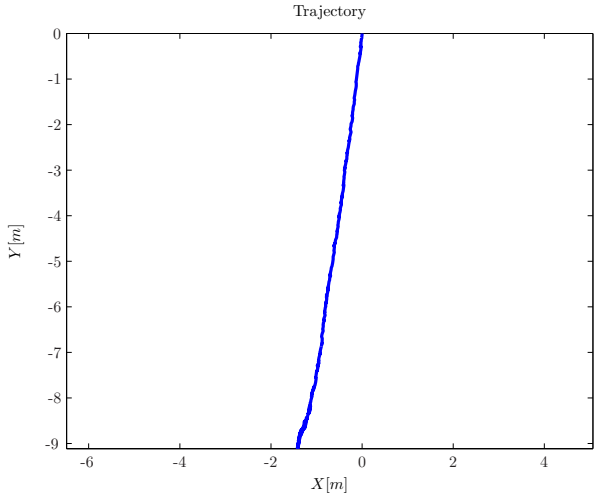

Figure 5.7: Example of uncorrectable error - Acquisition referred to a stand-still condition. During the whole acquisition the vehicle stood still and just 4 satellites were available: due to this reduced number, the data coming from the GPS measured a motion of about 9 meters.

the so-called "reliability vector". In case of optimal acquisition, the "reliability indexes" - *i.e.* the components of the reliability vector - are the standard deviations of the signals (identified in a previous sensor analysis campaign), while different values are them assigned at the verification of particular conditions.

The clearest example of this operation concerns the GPS system data. The quality of the data coming from such a system strictly depends on the number of available satellites ($sats$). An example of such a dependance can be seen in Fig. 5.7.

The GPS gives information if at least 4 satellites are available, and more satellites are visible and better the measures are. The GPS VBOX gives the number of visible satellites, thus an exponential weighting function has been designed for the standard deviations, that a) assigns a large standard deviation if $sats < 4$ and b) quickly decreases at the $sats$ increasing. Its formulation is

$$w_{SATS} = 1 + 1000e^{4-\frac{sats}{0.5}}; \tag{5.7}$$

and its profile is shown in Fig. 5.8. This approach allows to take in to account the effect of satellite constellation on the quality of the Global Positioning System measures.

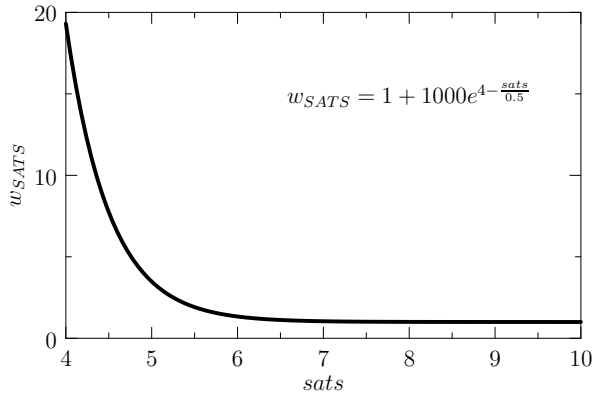

Figure 5.8: Satellites weighting function. The quality of the measures provided by the GPS strictly depends on the satellite constellation. Therefore a weighting function has been designed in order to consider such a dependance.

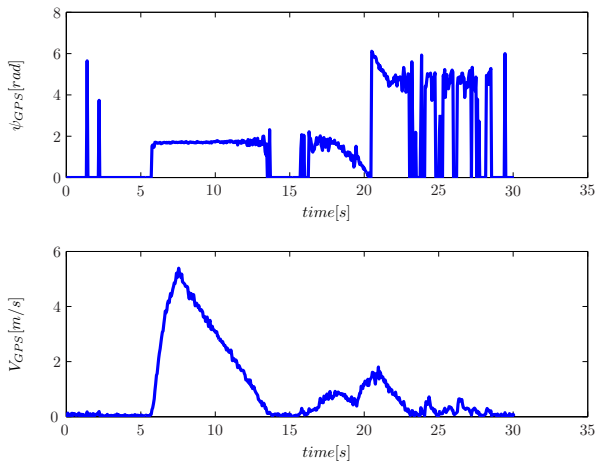

Figure 5.9: Effect of the velocity on the heading measure quality. Since the heading measure (*top*) is based on the Doppler effect, its quality depends on the vehicle velocity (*bottom*).

Another example of uncorrectable measure is about the heading angle, measured by the GPS unit. The measure of such an angle is in fact based on the Doppler effect, and is unreliable if the vehicle stands still even in presence of numerous visible satellies. Moreover the angle can not be corrected using

the last reliable value, since the error occurs also if the vehicle moves very slow (absolute velocity ≤ 1 m/s). The effect of velocity on the heading measure quality is shown in Fig. 5.9: the heading profile (*top*) presents a lot of jumps when the vehicle moves slow velocity (*bottom*). Anyway this condition of motion can be easily recognized combining the measures of velocity (from the GPS) and those of the odometers. In case that the velocity was $V \leq 1$ m/s and the odometers stood still, the value 2π is assigned to the standard deviation of the heading angle, labelling the measure as unreliable.

As will be shown in § 5.4, the assignment of the standard deviation is very efficient, since it allows to play with the weights given to the measures by the Kalman Filter, reducing the errors during the state estimation.

5.3 The Extended Kalman Filter

In Fig. 5.3 it is shown that the Extended Kalman Filter[1] has been chosen as state estimator. The information used by the filter for the state estimation are the measures $\boldsymbol{y}_k$ obtained by the sensors and the inputs $\boldsymbol{u}_k$ applied to the system. Moreover the knowledge of the uncertainty on these data allows an evaluation of the estimation accuracy.

The filter working principle is then quite simple: solving a statistical optimization problem, the filter combines the data coming from noisy sensors with those of a system's mathematical model, in order to estimate the set of states that gives the best matching between these information.

The Kalman filter is a *recursive* estimator, *i.e.* only the estimated state from the previous time-step and the current measurement are needed to compute the estimate for the current state. The state of the filter is represented by two variables:

- $\boldsymbol{x}_k$, the *a-posteriori* state estimate at time k, given observations up to and including at time k;
- $\boldsymbol{P}_k$, the *a-posteriori* error covariance matrix.

The Filter is divided in two distinct phases: Prediction and Correction. The prediction phase uses the state estimate from the previous time-step to

[1] Two main kinds of Kalman Filter can be found in literature: the Simple (SKF) and Extended Kalman Filter (EKF). The difference between the two configuration is very simple: the first one is applied to linear models, and the latter to non-linear models. Therefore the equations that govern the algorithms are identical, with the only difference that a model linearization is computed for the EKF.

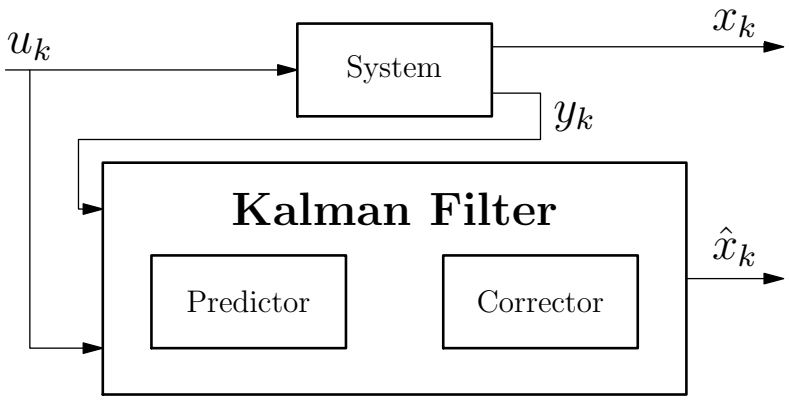

Figure 5.10: Kalman Filter architecture. Based on the system inputs, the filter predicts the system states. Such a prediction is then corrected by means of the measures, in order to estimate the internal state of the system.

produce an estimate of the state at the current time-step, based on a state-space representation of the system. This predicted state estimate is also known as the *a-priori* state estimate because, in spite of the fact that it is an estimate of the state at the current time-step, it does not include measures from the current time-step. In the correction phase, the *a-priori* prediction is combined with current measures to refine the state estimate. This improved estimate is called the *a-posteriori* state estimate. Understanding the meaning of this description is probably easier by analysing the procedure equations step-by-step.

Prediction: a-priori state estimate

Based on the system state-space model, the state at the time-step k can be predicted from the state estimate at the previous time-step and the system inputs. To do this estimate, one could feel prompt to use an equation like (5.3), nevertheless this is not necessary. For instance, considering a backward Euler discretization, the a-priori estimate could be achieved using the non-linear system model as follows:

$$\hat{\boldsymbol{x}}_k = \boldsymbol{x}_{k-1} + \boldsymbol{f}\left(\boldsymbol{x}_{k-1}, \boldsymbol{u}_{k-1}\right) dt \tag{5.8}$$

where dt is the time-step. Let's notice that the state estimate has to be assigned at the initial time-step ($k = 1$): this operation is termed "Kalman Filter Tuning".

Prediction: a-priori covariance matrix estimate

$$\hat{\boldsymbol{P}}_k = \boldsymbol{A}_k \boldsymbol{P}_{k-1} \boldsymbol{A}_k^T + \boldsymbol{Q} \tag{5.9}$$

This operation estimates the estimation accuracy, based on the previous estimate of the covariance and on the state transition matrix. $\boldsymbol{Q}$ is the covariance matrix of the state noise vector

$$\boldsymbol{Q} = E(\boldsymbol{w}\boldsymbol{w}^{\boldsymbol{T}})$$

As for the previous case, the covariance estimate has to be assigned at the initial time-step ($k = 1$), and this operation is part of the "Kalman Filter Tuning" too.

Correction: Optimal Kalman Gain

$$\boldsymbol{K}_k = \hat{\boldsymbol{P}}_k \boldsymbol{H}_k^T \left(\boldsymbol{H}_k \hat{\boldsymbol{P}}_k \boldsymbol{H}_k^T \right) \tag{5.10}$$

The Kalman Gain is the matrix that assigns the weights to the estimates and the measures, and its formulation comes from the solution of an optimization problem (a minimum mean-square error estimator). The matrix $\boldsymbol{R}$ is computed as

$$\boldsymbol{R} = E(\boldsymbol{v}\boldsymbol{v}^{\boldsymbol{T}})$$

and represents the covariance matrix of the measures vector.

Correction: a-posteriori state estimate update

$$\boldsymbol{x}_k = \hat{\boldsymbol{x}}_k + \boldsymbol{K}_k \left(\boldsymbol{x}_k - \boldsymbol{H}_k \hat{\boldsymbol{x}}_k \right) \tag{5.11}$$

This step concerns the estimate update, *i.e.* the comparison of the state estimate and the observation information. The meaning of this equation is simple: by means of the Kalman gain, it evaluates how good the estimate $\boldsymbol{x}_k$ is w.r.t. the observation information $\boldsymbol{y}_k$. It is important to notice that, as for the a-priori state estimate, even in this case the update could be computed by means of the measures non-linear equations:

$$\boldsymbol{x}_k = \hat{\boldsymbol{x}}_k + \boldsymbol{K}_k \left(\boldsymbol{x}_k - \boldsymbol{g} \left(\hat{\boldsymbol{x}}_k \right) \right) \tag{5.12}$$

Correction: a-posteriori covariance matrix estimate update

$$\boldsymbol{P}_k = \left(\boldsymbol{I} - \boldsymbol{K}_k \boldsymbol{H}_k \right) \hat{\boldsymbol{P}}_k \tag{5.13}$$

As done for the state, even the covariance matrix must be updated: $\boldsymbol{P}_k$ plays the fundamental role of estimate accuracy index. By observing its evolution is in fact possible to recognize if the problem is converging to the best estimate (or not, *e.g.* in presence of strong unmodeled phenomena) and which states are better estimated.

5.4 Example of state estimation

As described before, once the measures have been preprocessed the out-and-out state estimation can be performed. For the described case, an Extended Kalman Filter has been used, but different algorithms could be adopted. Moreover, once a strategy has been chosen, different version and approaches could be used, depending on the interesting states (*e.g.* for a certain control strategy) and the considered measures/observation (*e.g.* for the availability of a reduced set of sensors). In this section a representative version of Extended Kalman Filter is described: the system mathematical representation and the considered measures are explained, focusing on the simplifications assumed for the design of the algorithm.

The presented version of the filter aims at estimating some vehicle kinematic variables: the vehicle dynamics (forces, moments, etc.) is not considered, while just the relations between some kinematic variables are treated. For the formulation of the vehicle model some simplifications have been assumed:

- The vehicle is considered as a solid body moving on a flat road (vertical motion is neglected).
- The body-fixed frame has its origin in the middle of the rear axle, with x-axis pointing forward, y-axis pointing to the vehicle left-side and, consequently, the z-axis pointing upward.
- The AHRS and GPS units are considered coinciding and linked to the same frame of reference, which is oriented as the vehicle-fixed frame and translated of a distance l_{SEN} along the x-axis.
- All the sensors are in known positions w.r.t. the vehicle-fixed frame of reference.

A schematic representation of the vehicle and the main dimensions and variables is shown in Fig. 5.11. The available observations of the system are the following:

- from the GPS unit:
  - the X and Y positions w.r.t. a local frame of reference
  - the heading angle ψ_{GPS}
  - the module of the velocity V

- from the AHRS unit:
  - the yaw angle ψ_{MAG} from the magnetometer
  - the yaw rate Ω
  - the longitudinal and lateral accelerations A_X and A_Y
- from the odometers:
  - the common-mode angular velocity ω_{CM} of the wheels

The measures vector is constituted by the positions, the heading and yaw angles, the absolute velocity and the wheels angular velocity:

$$\boldsymbol{y}^T = [X, Y, \psi_{GPS}, \psi_{MAG}, V, \omega_{CM}] \tag{5.14}$$

The components of the inputs vector are instead the accelerations and the yaw rate:

$$\boldsymbol{u}^T = [A_X, A_Y, \Omega] \tag{5.15}$$

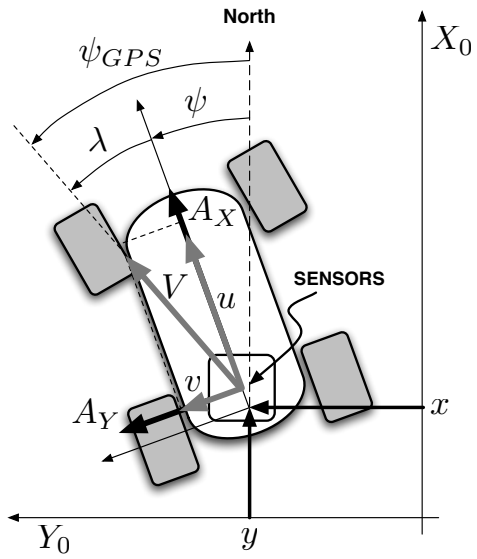

Figure 5.11: Main states and variables of the model. The vehicle is modelled as a rigid body moving on a flat road and the relations between different kinematic variables constitute the models of the system and of the measures.

Finally, the states vector is constituted by the vehicle positions, the yaw angle and the velocity components w.r.t. the vehicle-fixed frame:

$$\boldsymbol{x}^T = [x, y, \psi, u, v] \tag{5.16}$$

With these choices, it is possible to write the system in a non-linear state-space form, where the ODE system that describes its evolution is:

$$\frac{dx}{dt} = u\cos(\psi) - v\sin(\psi) + \Omega l_{SEN}\sin(\psi) \tag{5.17}$$
$$\frac{dy}{dt} = u\sin(\psi) + v\cos(\psi) - \Omega l_{SEN}\cos(\psi) \tag{5.18}$$
$$\frac{d\psi}{dt} = \Omega \tag{5.19}$$
$$\frac{du}{dt} = A_X + \Omega v \tag{5.20}$$
$$\frac{dv}{dt} = A_Y - \Omega u \tag{5.21}$$

The relations between the measures and the states are instead the following:

$$X = x + l_{SEN}\cos(\psi) \tag{5.22}$$
$$Y = y + l_{SEN}\sin(\psi) \tag{5.23}$$
$$\psi_{GPS} = \psi + \arctan\left(\frac{v}{u}\right) \tag{5.24}$$
$$\psi_{MAG} = \psi \tag{5.25}$$
$$V = \sqrt{u^2 + v^2} \tag{5.26}$$
$$\omega_{CM} = \frac{u}{R} \tag{5.27}$$

where R is the tyre radius. Obviously, each of the shown variables is affected by noise and other errors: this is the reason for which the noise vectors, in terms of the standard deviations computed by the Preprocessing algorithm, represent inputs to the filter.

The equations (5.17)-(5.27) give a non-linear continuos representation of the system, while a linear discrete representation is requested by the filter [2]. By applying a linearization of the system w.r.t. the previous time-step is equivalent to computing a backward Euler discretization. The matrices of the

[2] At least concerning the evaluation of the state transition and the state-measures matrices.

equivalent linearized discrete system are the following:

$$\boldsymbol{A} = \boldsymbol{I} + \begin{bmatrix} 0 & 0 & -u\mathrm{S}(\psi) - v\mathrm{C}(\psi) + \Omega l_{SEN}\mathrm{C}(\psi) & \mathrm{C}(\psi) & -\mathrm{S}(\psi) \\ 0 & 0 & u\mathrm{C}(\psi) - v\mathrm{S}(\psi) + \Omega l_{SEN}\mathrm{S}(\psi) & \mathrm{S}(\psi) & \mathrm{C}(\psi) \\ 0 & 0 & 0 & 0 & 0 \\ 0 & 0 & 0 & 0 & \Omega \\ 0 & 0 & 0 & \Omega & 0 \end{bmatrix} \tag{5.28}$$

$$\boldsymbol{H} = \begin{bmatrix} 1 & 0 & -\mathrm{S}(\psi) l_{SEN} & 0 & 0 \\ 0 & 1 & \mathrm{C}(\psi) l_{SEN} & 0 & 0 \\ 0 & 0 & 1 & -\frac{v}{u^2+v^2} & \frac{u}{u^2+v^2} \\ 0 & 0 & 1 & 0 & 0 \\ 0 & 0 & 0 & \frac{u}{\sqrt{u^2+v^2}} & \frac{v}{\sqrt{u^2+v^2}} \\ 0 & 0 & 0 & \frac{1}{R} & 0 \end{bmatrix} \tag{5.29}$$

where $\boldsymbol{I}$ is the identity matrix and the operators $\mathrm{S}(\cdot)$ and $\mathrm{C}(\cdot)$ represent, respectively, the sine and cosine functions.

Fig. 5.12 shows the estimated trajectory during a triangular-like manoeuvre covered on the balcony of the Engineering Faculty building in Mesiano - Trento. The understanding of the trajectory estimate quality is rather complex, since a comparison with the actual positions should be carried out and high-quality satellite images of the test track are not available. Nevertheless from the figure it is possible to appreciate the trajectory shape, which coincides with that of the track. Moreover the repetition of the path is captured with precision: the drift effects due to the numerical integration is avoided, mainly thanks to a good satellite constellation.

Interesting results are achieved also for the yaw angle: Fig. 5.13 compares the raw measures from magnetometer (yaw angle) and GPS (heading angle) with the estimated yaw angle during a sine-like manoeuvre [3]. A first observation can be done about the improving effect of the Preprocessing on the state estimation. During the first 5 seconds the vehicle stood still, and the heading measure is then unreliable: the assignment - by the Preprocessing - of a large standard deviation to such a measure induces the Filter to trust in magnetometer signal, yielding a good estimation even in this condition. After that interval, the vehicle moves on a sine-like track, and both the raw measures become reliable. Nonetheless a difference can be recognized between

[3]The observations about this and the next estimates refer to this sine-like manoeuvre, since the variables are better excited than not during the triangular-like manoeuvre, allowing more interesting discussions.

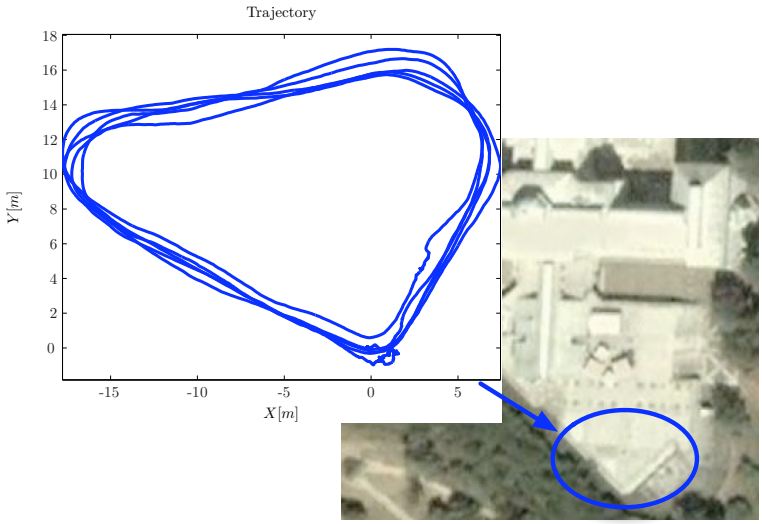

Figure 5.12: Estimated trajectory covered on Mesiano balcony. A triangular-like trajectory has been covered on the balcony of the Engineering Faculty in Mesiano - Trento. The satellite comparison shows the right shape of the trajectory, even if a better comparison can be achieved just on longer paths.

the estimate and the raw measures, and in particular the heading measure: this difference is not an error, since it constitutes the sideslip angle, which varies during the whole manoeuvre and can be thus estimated as shown in Fig. 5.14. In the end, the vehicle is turned in opposite direction and stopped, and the Preprocessing again forces the Filter to trust in magnetometer signal, neglecting the heading information.

Fig. 5.15 show instead the velocities profile. In particular, Fig. 5.15(a) demonstrates that a good estimate of the velocity components can be obtained, even if no direct measures of the lateral one are available: this result is of particular interest for two reasons. First of all, a good estimate of the longitudinal component of velocity is fundamental for the yaw rate control strategies discussed in Chapter 6. Secondly, a good estimate of the velocity components allows the derivation of additional information about important variables like the vehicle sideslip angle and the tyres slip ratios. Moreover both the figures show a good estimation when the vehicle stood still: this behaviour is achieved again thanks to the definition of the reliability indexes during the measures preprocessing. Stand-still condition is recognized thanks

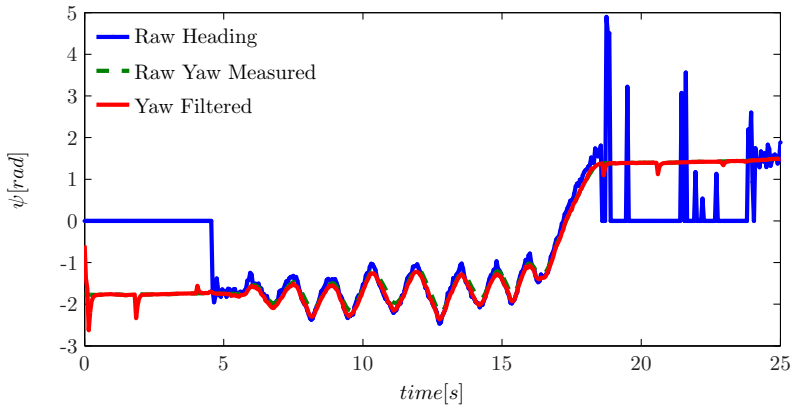

Figure 5.13: Comparison of measured and filtered yaw angle. The picture shows the effect of both the Preprocessing and the Filter. In the first interval the vehicle stands still and the heading measure is unreliable, but its estimation is anyway good thanks to the preprocessing. The sine-like shape of the central interval highlights instead a small difference between the estimated yaw and the measured heading, representing the sideslip angle.

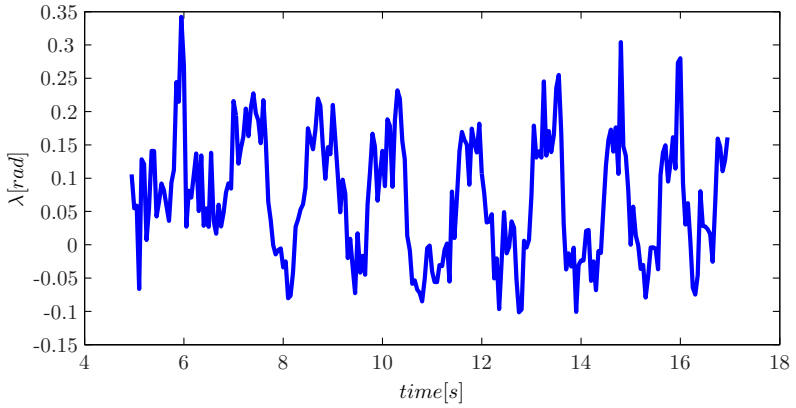

Figure 5.14: Detail of estimated sideslip angle. The picture shows the sideslip angle computed as the difference between the raw heading angle and the estimated yaw angle, during the sine-like manoeuvre: with the proposed architecture, also this variable (that is not a state) can be derived with a good reliability.

to both the measures from GPS and odometers, and thus a large standard deviation is assigned to the GPS raw velocity: the filter is then forced to trust in odometers signals (that say the wheels and the vehicle stand still). At the

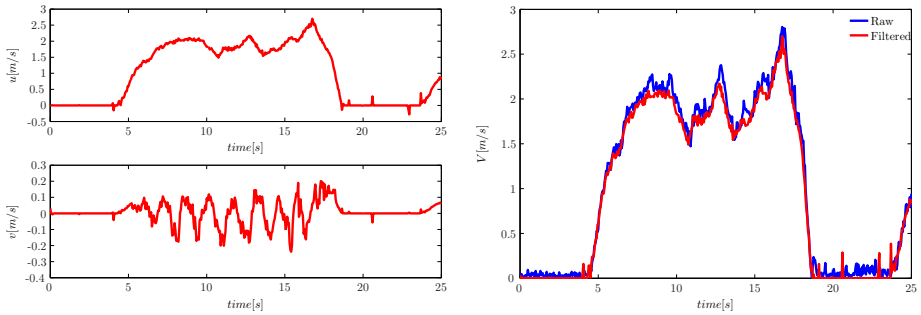

Figure 5.15: Estimated longitudinal and lateral velocities (*left*) and Comparison of measured and filtered absolute velocity (*right*). The filtered velocity is smoother than the measured one, and the noise present in stand-still condition is correctly cancelled. Moreover the filter allows the estimation of the components separately.

time the vehicle starts to move, both the measures are instead "considered" and fused together.

Even if the whole set of estimated states have been shown and discussed, attention must be paid to another important variable: the yaw rate. The control strategies discussed in Chapter 6 aim at controlling the vehicle yaw rate, and a good estimate of such a variable becomes then mandatory. Fig. 5.16 shows the comparison between the raw measure, provided by the AHRS, and the profile obtained by numerically differentiating the estimated yaw angle of Fig. 5.13. In spite of the fact that the estimated values come from a numerical differentiation, they present a profile smoother than the measured one. As will be shown in Chapter 6 this smoothness represents a particularly important result, because of the fact that a further differentiation of the yaw rate will be required by the control strategies.

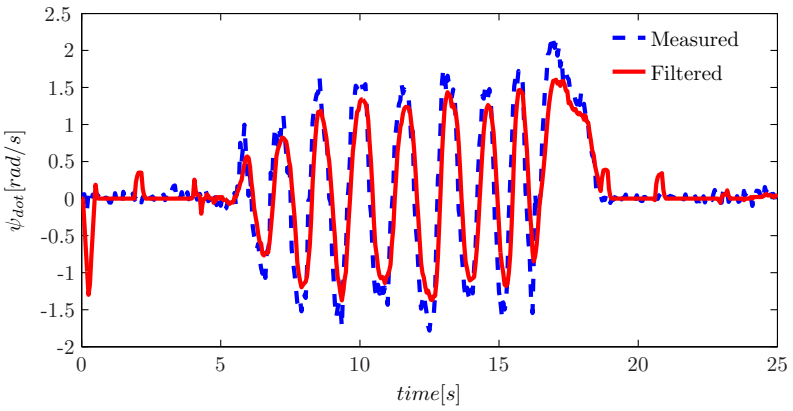

Figure 5.16: Comparison of measured and estimated yaw rate. By differentiating the estimated yaw angle, a smooth estimation of the yaw rate is obtained. Such a variable is of particular interest for the control strategies discussed in Chapter 6

Chapter 6

Yaw Rate Control

In the automotive control field strong efforts have been done mainly to design driving assistance systems that aid the driver to stabilize the vehicle lateral and yaw dynamics. Two main ways are available to control the vehicle yaw dynamics, that differ on the control inputs: steering angle or left/right differential wheel torque. A comparison of these two approaches is discussed in this chapter. In particular two yaw rate control strategies, differing on the control input, are here presented and compared by means of a simulation campaign.

The last decades have seen strong efforts on the development of safety systems oriented to aid the driver in critical driving condition. The most famous safety system is undoubtedly the Antilock Braking System, commercialized by Bosch since 1978, which prevents the wheels from locking up while braking. Other examples of safety systems are available on vehicles, like the Bosch Electronic Stability Program (ESP) that exploits the ABS to introduce a differential braking and stabilizes the yaw dynamics, or, recently, the Volvo City Safety, that autonomously brakes in presence of obstacles.

Moreover, Advanced Driving Assistance Systems (ADAS) are strongly studied in the last years. While driving, the pilot indeed carries out two main operations: path following and disturbance rejection. The goal of ADAS is to leave to the driver the only path following task, by rejecting disturbances and by aiding him/her to take future decisions (by means of warning messages) or by taking such decisions when it is too late to warn (*e.g.* active braking). In order to do that the ADAS have obviously to estimate the surrounding scenario, by means of different sensors and information, like video cameras, radar

and laser systems, digital maps and so on. For instance, Adaptive Cruise Control (ACC) and Frontal Collision Warning (FCW) systems are well known in the literature and are mature technologies already on the market (Bengtsson , 2001, Vahidi and Eskandarian , 2003). ACC and FCW systems autonomously adapt vehicle speed and distance from foregoing vehicles, reducing the collision risk.

Nevertheless the main driving disturbances affect the yaw dynamics, and this chapter treats precisely this problem. In this case a wider definition of disturbance is required, since it is intended as the difference between the desired and the actual behaviour, collecting both the unforeseen phenomena (*e.g.* loss of adherence, side-wind effects, and so on) and the undesired behaviours (*i.e.* vehicle under- or over-steering). Therefore, a yaw dynamics control strategy must relieve the driver of the operation of following a yaw-rate profile, living him more "intelligent" tasks. This statement involves an interesting consideration. In fact, by following longitudinal velocity and yaw rate profiles also the vehicle trajectory can be controlled. Consequently, in the perspective of decoupling longitudinal and lateral dynamics, the yaw rate control strategies discussed in this chapter might join already existing velocity control systems, in a trajectory following architecture.

Based on the control input, two main kind of control strategies can be recognized: those acting on the steering angle and those based on the application of a left/right differential wheel torque. The approaches are discussed in general terms in § 6.1, with a comparison of the advantages/disadvantages of each one. § 6.2 presents instead two specific controllers, charaterized by the same architecture (based on a disturbance observer) but acting on different control inputs. Finally, the results of a simulation campaign carried out to compare the effects of the control strategies is presented in § 6.3.

6.1 Available approaches for the control of the yaw dynamics

The yaw dynamics can be controlled by acting on the steering angle or by applying different torques at the right and left wheels. Hence, four main kind of yaw dynamics control systems can be discerned:

- **Differential Braking**: systems that utilize the ABS[1] to apply different

[1] ABS - Antilock Braking System, a safety system that prevents the wheels from locking up and guarantees the vehicle handling while braking.

braking torques at the right and left wheels.

- **Active Front Steering**: systems that use Steer-by-Wire architectures in order to modify the steering angle commanded by the pilot, adding a suitable correction.

- **Active Torque Distribution**: technologies that exploit electronic differential gears on 4WD vehicles in order to independently control the driving torque acting on each wheel, contemporarily stabilizing both the yaw dynamics and the driving/braking traction.

- **Active Rear Steering**: for vehicles equipped with Steer-by-Wire technologies for both the front and rear wheels, the system works in the same way as the Active Front Steering.

In the last years the problem of vehicle dynamics control has been strongly analysed by the automotive companies, that have also commercialized some systems like BMW DSC3 and Mercedes ESP (1995), Cadillac Stabilitrak System (1996) and Chevrolet C5 Corvette Active Handling System (1997). Many names have been used by companies to identify their own yaw dynamics control systems: Vehicle Stability Assist (VSA), Vehicle Dynamics Control (VDC), Vehicle Stability Control (VSC), Electronic Stability Program (ESP), Electronic Stability Control (ESC), Direct Yaw Control (DYC) and so on.

The differential braking systems are undoubtedly the most studied and commercialized, also because they can be easily installed on ABS-equipped vehicles: it is sufficient to add a gyroscope and a microcontroller that compensates undesired yaw dynamics by opportunely distributing -through the ABS- the braking torque on the four wheels. The last decade has witnessed a strong improvement of Steer-by-Wire and active torque distribution systems, mainly thanks to the availability of new on-board technologies. For instance, Audi proposed an ADAS that combines the effects of a steer-by-wire technology with those of an active distribution torque: in case of manoeuvres close to handling limits, the system brings the vehicle close to the adherence peak (Schwarz et al., 2008) avoiding potentially hazardous situations. Some active rear steering are also available. For instance, BMW proposed an active four-wheel-steering system that strongly improves the vehicle manoeuvrability, and allows the development of innovative driver assistance systems (Schuster et al., 2008).

The effectiveness of the above mentioned active systems can be evaluated on the base of different criteria, like comfort, manoeuvrability, safety, etc.

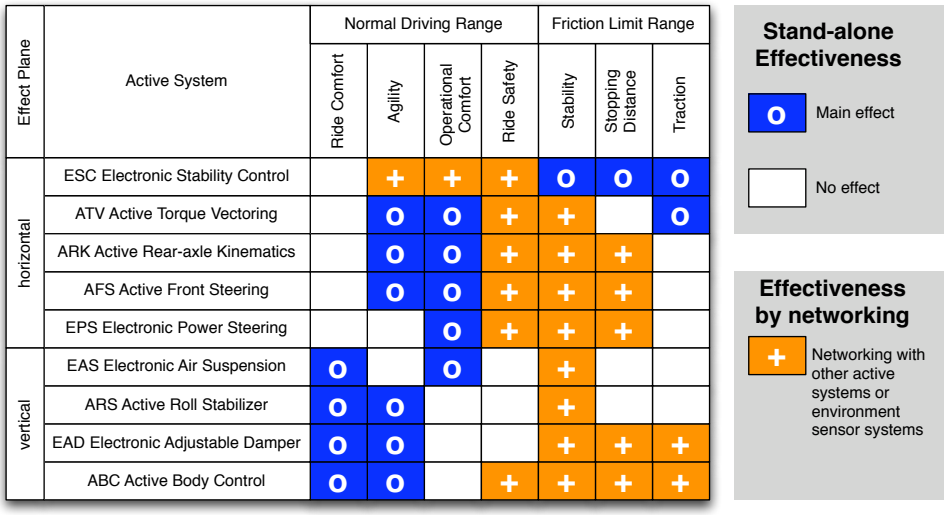

Figure 6.1: Portfolio of active systems and their effectiveness in the regions of normal driving and at the friction limit. The effectiveness of the individual stand-alone systems can be extended significantly by networking with other active systems or environment sensor systems.

An interesting analysis about this topic is presented in (Raste et al., 2008). The authors discuss the benefits of a range of active safety systems, analysing their effectiveness in stand-alone and networking configurations (Fig. 6.1). In fact, in the last years there has been the tendency to combine different systems together. In particular, two main approaches to the problem can be distinguished:

- different assistance systems are designed separately, and a supervision unit manages the activation of each one of them;
- the systems are designed and work together in a unique architecture.

From the actuation point of view, the yaw dynamics can be thus controlled acting on two inputs: the steering angle and the torque (for instance, the braking torque) acting at each wheel. Even so, the efficiency of braking and steering is not equal (Ackermann et al., 1999). In order to demonstrate this, three simplifying assumptions are made:

- The total force F_{max} transmittable by the tyres does not depend on the

direction in which the force acts - Kamm's circle (Kiencke and Nielsen , 2000).

- The Centre of Mass is assumed to be midway between the front and rear axles of the vehicle.

- The wheelbase L is twice the track-width t.

Fig. 6.2 compares the yaw torques due to front wheel braking and front wheel steering. In case of differential braking the maximum available yaw moment is $M_{brake} = F_{max}t/2$, while from front wheel steering it is $M_{steer} = 2F_{max}t$. In other words, steering requires only one fourth of the front wheel tyre force, compared to asymmetric braking of the front wheels, to generate the same yaw moment.

A further advantage of active steering is that it allows for a compensation of torques caused by asymmetric braking. An extreme μ-split braking situation ($\mu = 0$ under the right tyres) is shown in Fig. 6.3. The combination of braking and steering allows for a balance of the yaw moments $M_{brake} - M_{steer} = 1.6F_{max}t/2 - 0.8F_{max}t = 0$ and there still remains $1.6F_{max}$ for deceleration. An ABS (left hand side of the figure) would produce a deceleration force $2F_{max}$ and therefore a disturbance moment $M_{brake} = F_{max}t$.

Even if the major effectiveness of the active steering has been demonstrated, both the architectures have a beneficial effect on the vehicle manoeuvrability, and this is the main topic discussed in next sections.

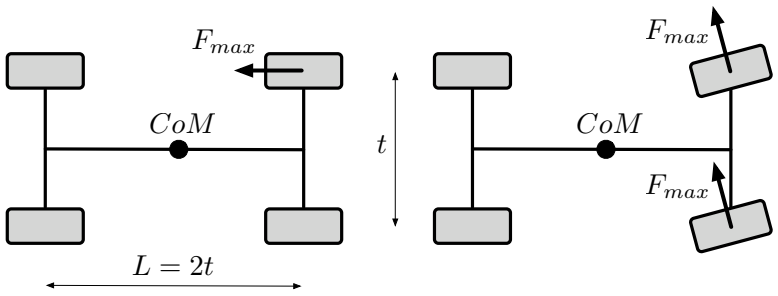

Figure 6.2: Yaw moments from front wheel braking (*left*) and front wheel steering (*right*). Steering requires only one fourth of the front wheel tyre force, w.r.t. asymmetric braking, to generate the same yaw moment.

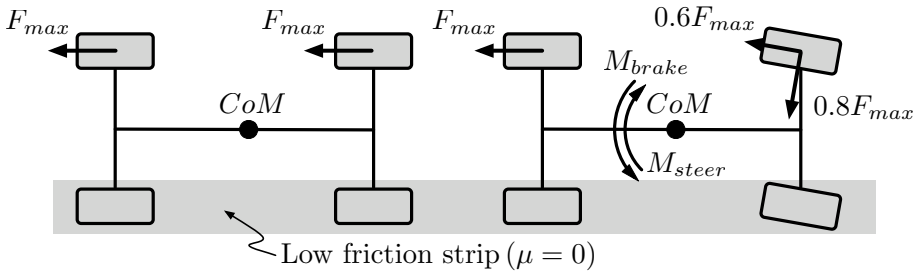

Figure 6.3: For extreme μ-split braking the balance of moments yields zero brake force $F = 0$ for braking only (*left*) and $F = 1.6F_{max}$ brake force for combined braking and steering (*right*).

6.2 Yaw rate control strategies based on Disturbance Observer

As explained, two different yaw rate control strategies are presented and compared in this chapter. The common denominators of these yaw rate control strategies are a) the control architecture and b) the model used for their design. In spite of the fact that the strategies act on different vehicle inputs, both are based on a disturbance observer architecture, that is thought for estimating and compensating all the unmodeled -and undesired- phenomena acting on the yaw dynamics. The disturbance observer is additionally coupled with a feedback architecture, in order to force the system (*i.e.* the vehicle) to the nominal behaviour. Concerning the model adopted for the control synthesis, a linearized version of the bicycle model described in § 3.2.1 has been used.

In the following two sections these common denominators are discussed, focusing on the assumed simplification and their effects. After that the control strategies are discussed, with emphasis on the architecture and the system plant used for their synthesis.

6.2.1 Introduction to the Disturbance Observer

The Disturbance Observer (commonly denoted DOB) is a particular architecture that allows, under certain hypothesis, the estimation of additional disturbances acting on a system. In Fig. 6.4 a schematic representation of the observer is shown.

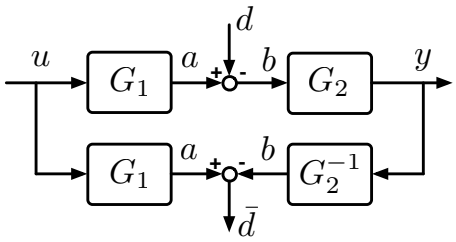

Figure 6.4: Generic architecture of the disturbance observer. Under the hypothesis that the sensor transfer function G_2 can be inverted, the additional disturbance d acting between the system and the sensor can be estimated.

It is supposed that the system transfer function $G(s)$ is a factorization of two terms:

$$G(s) = G_1(s)G_2(s) \tag{6.1}$$

such that the disturbance can be represented as an additional contribution acting between $G_1(s)$ and $G_2(s)$. It is assumed besides that $G_2(s)$, commonly describing the sensor measuring the output, is an invertible transfer function.

Using the same symbols adopted in Fig. 6.4, the system output y can be computed as:

$$\begin{aligned} y &= G_2 b \\ &= G_2(a-d) \end{aligned} \tag{6.2}$$

Is then possible to demonstrate that the disturbance estimate $\bar{d}$ is:

$$\begin{aligned} \bar{d} &= a - b \\ &= a - G_2^{-1} y \\ &= a - G_2^{-1} G_2 (a-d) \\ &= a - a + d \\ &= d \end{aligned} \tag{6.3}$$

The described architecture concerns the most generic representation of the DOB. Nevertheless, the one adopted in this chapter is based on a couple of assumptions. First of all, the sensor is supposed to be ideal ($G_2(s) = 1$). Moreover, once the additional disturbance is estimated, an architecture for its compensation is introduced.

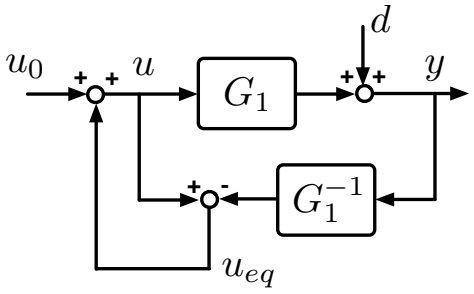

Figure 6.5: Disturbance observer with compensation. If the nominal plant G_1 is invertible, the architecture allows the estimate of u_{eq}. This term is the equivalent input responsible of the additional disturbance d, which can be thus compensated.

In other words, the desired response of the system $G_1(s)$ to a generic input u_0 is:

$$y = G_1 u_0 \tag{6.4}$$

Supposing that the system transfer function G_1 is invertible, the compensation can be achieved with the architecture shown in Fig. 6.5. The term u_{eq} can be interpreted as the equivalent input that would be responsible of the additional disturbance d, and its formulation is the following:

$$\begin{aligned} u_{eq} &= u - G_1^{-1} y \\ &= u - G_1^{-1} G_1 u - G_1^{-1} d \\ &= -G_1^{-1} d \end{aligned} \tag{6.5}$$

Thus, by substituting the (6.5) in the formulation of the system response, it is immediate demonstrated that the desired behaviour (6.4) is achieved.

$$\begin{aligned} y &= G_1 u + d \\ &= G_1 \left(u_0 + u_{eq}\right) + d \\ &= G_1 u_0 + G_1 \left(-G_1^{-1} d\right) + d \\ &= G_1 u_0 \end{aligned} \tag{6.6}$$

6.2.2 Vehicle Model

The purpose of Model-Based Design is to formulate a mathematical model of the control plant, that allows the synthesis of a control system. The model

obviously gives a reduced description of the actual system, since it has to trade off the representativeness for the simplicity.

Both the control architectures described in this chapter are based on a very simple vehicle model: a linearization of the bicycle model shown in Fig. 6.6. The characteristics and the equations of motion of the model are the same described in § 3.2.1, with the sole exception of the yaw moment input N_z due to a differential driving/braking torque: the possibility to apply a yaw moment is necessary to compare the control strategies. To avoid an over-complication of the model, the yaw moment N_z is considered as an external action. From an applicative point of view, the yaw moment can be obtained based on the following equations:

$$N_z = \frac{t}{2}\left(F_{Xr} - F_{Xl}\right) \tag{6.7}$$

$$F^*_{ac} = F_{Xr} + F_{Xl} \tag{6.8}$$

where t is the trackwidth. By simultaneously solving (6.7) and (6.8), the force command signals F_{Xl} and F_{Xr} on, respectively, left and right wheels can be determined from the desired yaw moment N_z and acceleration command F^*_{ac}. Thus, the torque to be applied by the in-wheel motors can be determined as:

$$T^*_r = RF_{Xr}\,, \qquad T_l = RF^*_{Xl} \tag{6.9}$$

Since no anti-skid systems are introduced, the wheels dynamics is neglected. Additionally, vehicle speed V is considered constant[2] and the yaw rate is considered to be linearly dependant on the control inputs via proper transfer functions. Finally, it is assumed that the rejection of unmodeled phenomena, *e.g.* disturbances or undefined dynamics, is guaranteed by control robustness.

Under the described assumptions, the vehicle maintains just two Degrees Of Freedom - the yaw rate ψ_{dot} and the sideslip angle λ - and the linear equations of motion are the following:

$$MV\left(\frac{d\lambda}{dt} + \psi_{dot}\right) = F_{Yf} + F_{Yr} + F_{Yd} \tag{6.10}$$

$$I\frac{d\psi_{dot}}{dt} = N_z - N_t + N_d \tag{6.11}$$

[2]The control system is designed for a generic constant velocity V: the extension to a wide range of vehicle velocities is achieved employing look-up tables of the control parameters, where this is necessary.

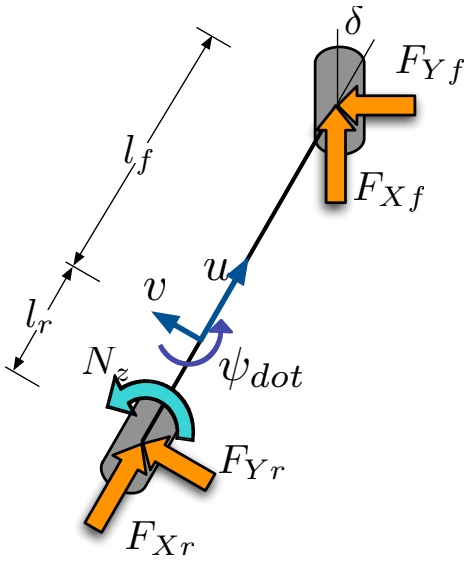

Figure 6.6: The bicycle model. The model presents an additional control input: the yaw moment N_z. This allows the direct yaw moment control, and can be achieved opportunely distributing the torque between the left and right in-wheel motors.

where M is the vehicle total mass, I is the vehicle yaw inertia and N_t is the yaw moment generated by tyres lateral forces. F_{Yd} and N_d are the disturbance lateral force and the disturbance yaw-moment, respectively, which are caused by side wind and other unmodeled phenomena.

As described on the right of (6.11), yaw-moment generated by tyres is defined as $N_t := F_{Yf} l_f - F_{Yr} l_r$. l_f and l_r are the distances between the centre of mass and the wheels, and F_{Yf} and F_{Yr} are the lateral forces of the front and rear wheels. Under linear hypothesis the forces may also be written as follows:

$$F_{Yf} = C_f \left(\delta - \lambda - \frac{l_f}{V} \right) \tag{6.12}$$

$$F_{Yr} = C_r \left(-\lambda + \frac{l_r}{V} \right) \tag{6.13}$$

where C_f and C_r are the cornering stiffnesses at front and rear axis, respectively, and δ is the steering angle. Let's notice that the cornering stiffness' of (6.12)-(6.13) comprise even the normal loads acting at the tyre-ground

contact point. In order to maintain the model simplicity, load transfers are neglected, and the normal loads assume the following formulations:

$$F_{Zf} = \frac{Mgl_r}{L} \tag{6.14}$$

$$F_{Zr} = \frac{Mgl_f}{L} \tag{6.15}$$

It is worth noting that the model fulfils the purpose it has been designed for, *i.e.* a linear dependence can be written between the yaw rate ψ_{dot} and both the yaw control inputs N_z and δ.

6.2.3 Direct Yaw-moment Control

In this section, a robust Direct Yaw-moment Control (DYC) is discussed. The system aims at controlling the vehicle yaw rate acting on the differential braking/driving, and is based on the dynamics equations described by (6.10)-(6.11). From such equations it is easy to note that the actual speed vector (*i.e.* lateral and forward velocities) is needed to measure λ and V, but its evaluation is particularly hard. Moreover, measurement and estimation of cornering forces are difficult because they are non-linear variables. Thus, it is assumed that the effect of these variables is an additional disturbance moment about the vertical axis. In (Sakai et al., 1999, Fujimoto et al., 2004) novel direct yaw-moment control was proposed, based on a disturbance observer that compensates these immeasurable terms as the lumped disturbance $N_{td} = -N_t + N_d$.

This specific disturbance observer is called Yaw-Moment Observer (YMO), and its architecture is shown in Fig. 6.7. By using the moment N_z as the control input and the yaw rate ψ_{dot} as the measured signal, the YMO can compensate the lumped disturbance and nominalize the system as:

$$\psi_{dot}(s) = \frac{1}{Is} N_z(s) \tag{6.16}$$

As described in § 6.2.1, the architecture allows the estimate and compensation of additional disturbances linearly acting on the system. Nevertheless, the vehicle plant of Fig. 6.7 gives just a simplified representation of the complex non-linear system "vehicle", affected by both linear and non-linear disturbances. For this reason, the full architecture of the DYC is the one shown in Fig. 6.8. The vehicle plant is substituted by a non-linear complex vehicle model - or the actual vehicle in experimental phase - and presents two inputs:

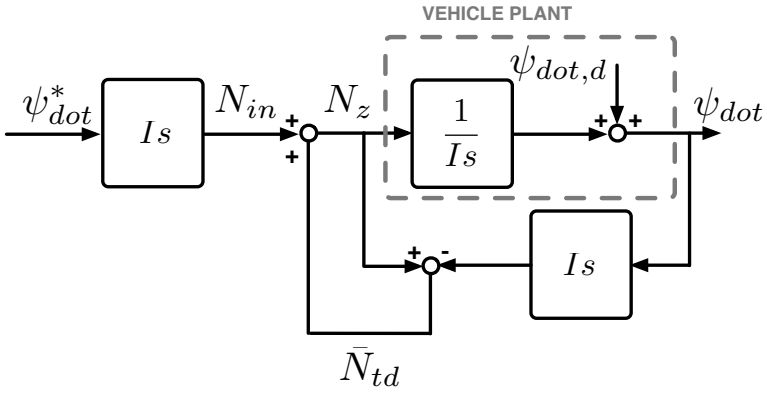

Figure 6.7: Block diagram of the Yaw-Moment Observer with disturbance compensation. Given a desired yaw rate ψ^*_{dot}, the yaw moment input N_{in} can be evaluated from the nominal plant. All the additional disturbances can be estimated and compensated thanks to the feedback structure of the system.

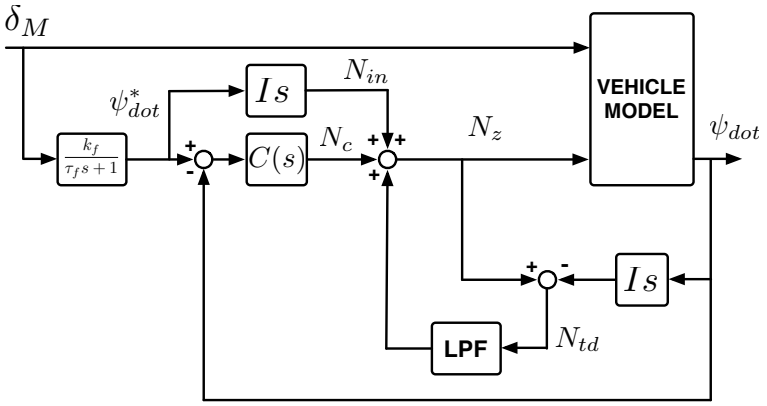

Figure 6.8: Block diagram of the Direct Yaw-moment Control. the internal loop, comprising the DOB, allows the compensation of the additional yaw-moment disturbances. Anyway an outer feedback loop is added to compensate the non-linear disturbances and nominalize the system.

the steering angle, from the driver, and the yaw-moment, from the control. Moreover, an outer yaw rate feedback loop is added, for the non-linear disturbance compensation. As said, a steering angle δ is introduced by the driver:

from such an input, the desired yaw-rate profile is computed as

$$\psi^*_{dot} = \frac{k_f}{\tau_f s + 1}\delta \tag{6.17}$$

where τ_f and k_f are vehicle characteristic parameters, that can be experimentally evaluated or derived from the mathematical representation of the yaw rate dynamics of a neutral vehicle[3]. Given the desired yaw rate, the control input N_{in} can be computed inverting the nominal plant (6.16). Additionally, the desired yaw rate is compared to the measured one, in order to evaluate the error for the controller $C(s)$ and compute the controller yaw moment N_c. The yaw moment N_z is therefore the sum of three contribution: the nominal moment N_{in}, the controller moment N_c and the estimated lumped disturbance $\bar{N}_{td}$. Supposing a proportional controller ($C(s) = K$), the yaw moment becomes:

$$\begin{aligned} N_z &= N_{in} + N_c + \bar{N}_{td} \\ &= I\psi^*_{dot}s + K\left(\psi^*_{dot} - \psi_{dot}\right) + \left(N_z - I\psi_{dot}s\right) \end{aligned} \tag{6.18}$$

which yields $\psi_{dot} = \psi^*_{dot}$, *i.e.* the desired behaviour.

Concluding, two considerations of practical nature have to be done. First of all, the presence of a Low Passing Filter (LPF) after the disturbance estimation is necessary to eliminate spikes due to the derivation of the measured noisy signal ψ_{dot}. Moreover, the controller $C(s)$ is designed using the Ackermann's pole-placement method (Ackermann , 1980). The Ackermann's algorithm allows to evaluate the gain of a closed-loop proportional controller, given the open-loop system dynamics equation and the desired position of the closed-loop pole.

6.2.4 Active Front Steering

The second control strategy discussed is the Active Front Steering (AFS) control. This architecture aims at stabilizing the vehicle yaw dynamics and assisting the user during the remote control operations, and has been studied explicitly for the vehicle RUMBy. The AFS control is the only way possible to implement a yaw rate control in the adopted vehicle, since independent wheel braking/driving is not available.

[3]Vehicles can be classified, based on their yaw dynamics, in under-steering, neutral and over-steering: the best response is the neutral one, thus the goal of yaw rate control is forcing the vehicle to have such a behaviour.

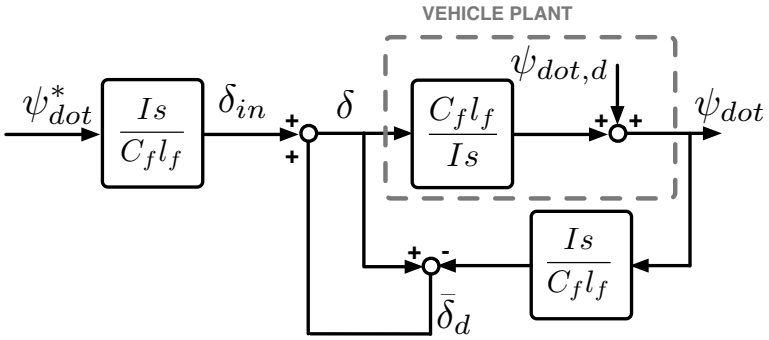

Figure 6.9: Block diagram of the Yaw-Moment Observer with disturbance compensation. Given a desired yaw rate ψ^*_{dot}, the steering input δ_{in} can be evaluated from the nominal plant. All the additional disturbances can be estimated and compensated thanks to the feedback structure of the system.

For the same reasons described in the previous section, this control strategy is even based on the Yaw-Moment Observer, and the vehicle model adopted as nominal plant for the control synthesis is the linear 5DOF described in § 6.2.2. The main difference w.r.t. the previous case is that the direct yaw control by means of differential braking/driving is not allowed ($N_z = 0$). Therefore, neglecting the yaw moment N_z, and substituting the linearized forces (6.12)-(6.13), the yaw dynamics (6.11) becomes:

$$I\frac{d\psi_{dot}}{dt} = C_f\left(\delta - \lambda - \frac{l_f}{V}\right)l_f - C_r\left(-\lambda + \frac{l_r}{V}\right)l_r + N_d \tag{6.19}$$

As described in § 6.2.1, the disturbance observer (and the compensation) works well on additional disturbances, thus (6.19) can be written as

$$I\psi_{dot}s = C_f l_f \delta + N'_d \tag{6.20}$$

where N'_d collects the disturbance N_d and all the terms that do not directly depend on the input δ. (6.20) can be thus written in terms of the yaw rate as:

$$\psi_{dot} = \frac{C_f l_f}{Is}\delta + \psi_{dot,d} \tag{6.21}$$

where the first term represents the nominal plant and $\psi_{dot,d}$ is the equivalent yaw rate due to disturbance. With the same approach adopted in the previous

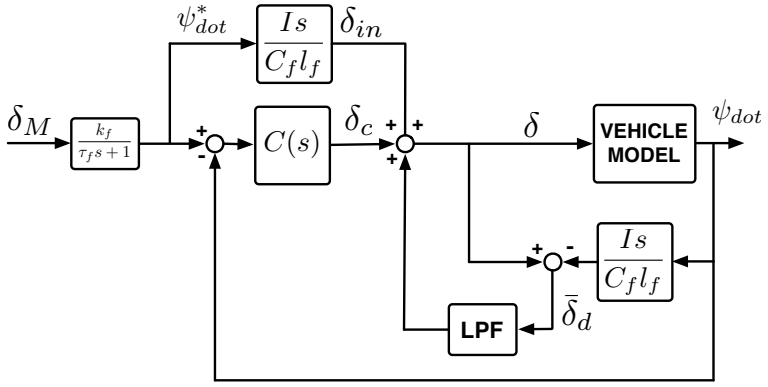

Figure 6.10: Block diagram of the Active Front Steering control. By means of the driver input signal δ_M, the reference yaw rate is computed. This value is then followed thanks to the disturbance compensation and the outer feedback loop, that respectively compensate the additional and non-linear disturbances.

case, the Yaw-Moment Observer has the architecture shown in Fig. 6.9. Such architecture allows estimating the equivalent steering angle $\bar{\delta}_d$ responsible of the disturbance on the yaw-rate, that can be then compensated.

Again, as discussed in the previous section, the disturbance rejection has to be coupled with an outer feedback loop in order to compensate the non-linear disturbances. The full architecture of the AFS control becomes then the one represented in Fig. 6.10. The system effectiveness can be mathematically demonstrated again computing the system input:

$$\begin{aligned} \delta &= \delta^* + C\left(\psi^*_{dot} - \psi_{dot}\right) + \delta_d \\ &= \frac{Is}{C_f l_f}\psi^*_{dot} + C\left(\psi^*_{dot} - \psi_{dot}\right) + \left[\delta - \frac{Is}{C_f l_f}\psi_{dot}\right] \end{aligned} \tag{6.22}$$

that again yields $\psi_{dot} = \psi^*_{dot}$.

As for the DYC, the low-passing filter is necessary to eliminate spikes in $\bar{\delta}_d$ due to differentiation and the controller $C(s)$ is designed by pole-placement with the Ackermann's method.

6.3 Strategies Comparison

As explained in the introduction of the chapter, a simulation campaign has been carried out in order to compare the yaw rate control strategies. Differen-

tial braking/driving is not possible with the vehicle RUMBy, and experimental tests of the Direct Yaw Control were therefore unfeasible. § 6.3.1 describes then the vehicle simulator developed for this purpose, while § 6.3.2 shows and discusses the results obtained comparing the control strategies during simple manoeuvres.

6.3.1 Virtual Environment Simulator

The comparison of the control strategies has been carried out by means of a static simulator, in a virtual environment like the one shown in Fig. 6.11. The system has been developed in the Mechatronics Laboratory, with the purpose of testing path planning algorithms and control strategies generated for the vehicle RUMBy.

In particular, the vehicle dynamics is modelled with the 14 Degrees of Freedom representation discussed in § 3.2.3. Moreover, the first order lag model of § 3.1.1 is adopted to describe the slips dynamics, while the tyre-ground interaction is represented by means of the non-linear Dugoff model explained in § 3.1.2. The mathematical model is written in C language in a Matlab Simulink S-function, that allows the development of purpose-made Simulink blocks for real-time simulations. The virtual environment has been created in VRML language, by means of the Matlab Virtual Reality Toolbox. Such a package allows the creation of a 3-D representation of virtual environments, running in real-time. In particular, the virtual driving point of view simulates

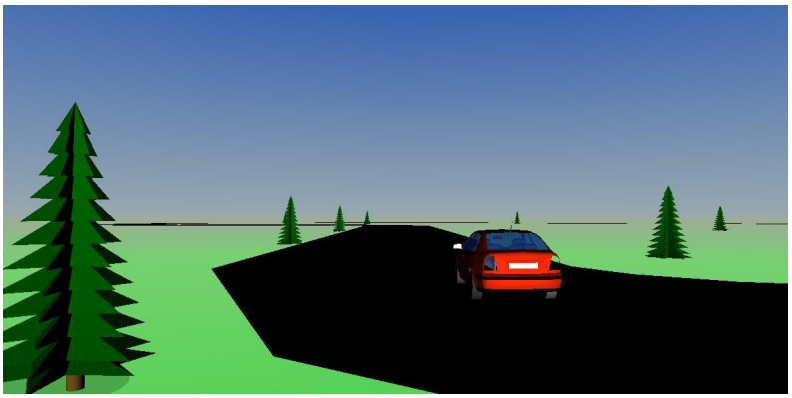

Figure 6.11: Example of the virtual environment created in VRML language by means of the Matlab Virtual Reality Toolbox.

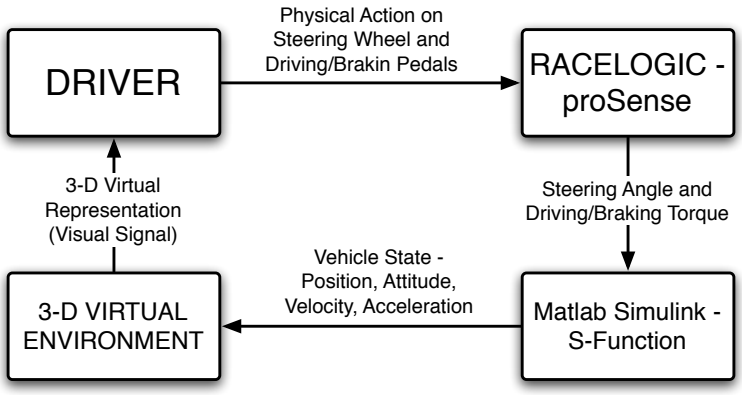

Figure 6.12: Loop of the simulation. The driver physically turns the steering wheel and pushes the pedals. These signals are transmitted to Simulink and translated in terms of steering angle and wheel torques. These represent the inputs to the S-function, which integrates the dynamics equation and computes the vehicle states. The vehicle states are then read by the Virtual Reality toolbox, which updates the virtual environment and transmits the visual signal to the driver.

the images that would come from an on-board camera, installed on the frontal part of RUMBy. Finally, a Force-feedback Racelogic platform -steering wheel and driving/braking pedals- has been used for the driving interface. The platform signals are transmitted to Simulink by a proSense block, that allows the real-time reading of the commands. The driving simulation runs then the loop of Fig. 6.12, at a frequency of 1 kHz.

It is important to notice that the driving on a static simulator is a completely different experience w.r.t. the actual one. The accelerations perceptible while driving a real car represent useful feedback information to the driver to understand vehicle behaviour and actual state: the static simulator does not yet give such sensations, making the driving particularly difficult. Moreover, because of the chosen point of view, the velocity perception is strongly reduced. While driving a real vehicle, the velocity is mainly perceived thanks to the peripheral vision: the chosen forward point of view strongly reduces the visual field, specially on the lateral boundaries. These effects make the simulator driving a very complex activity, hence attention will be paid to the effects of the controllers on easing the driving experience.

6.3.2 Simulation Results

This section discusses the effect of Direct Yaw Control and the Active Front Steering control on the vehicle dynamics, and in particular on disturbance rejection and on making the driving easier. In the previous section it has been explained that the driving of the vehicle with the simulator is particularly difficult, because of the bad longitudinal velocity perception and the absence of accelerations. A long simulation campaign, with several drivers and different tracks, has demonstrated that both the control strategies make the driving much easier in many conditions, and specially in curve entrance. In order to make the comparison more comprehensible, disturbance rejection and driving ease are discussed separately by analysing two simplified manoeuvres.

Before discussing the results of the comparison, a couple of comments are necessary. In case that the vehicle moves at the velocity V along a curve of radius R, its theoretical yaw rate is

$$\psi_{dot,\mathrm{th}} = \frac{V}{R} \tag{6.23}$$

Once the velocity V and the curvature R are known, (6.23) allows to directly compute the theoretical yaw rate profile of a curve/manoeuvre.

It is worth noting that, while driving, the theoretical yaw rate cannot be taken as reference for the controller, since it neglects the slips. Nevertheless

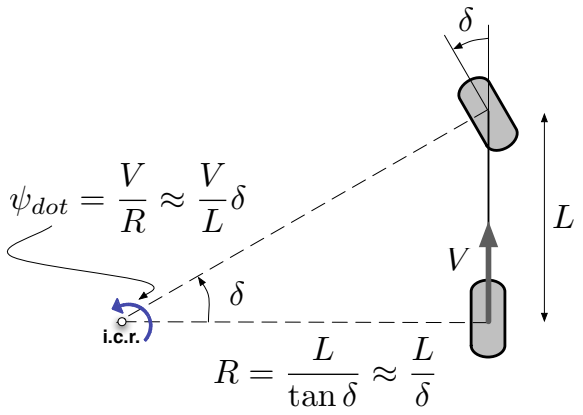

Figure 6.13: Kinematic linearized bicycle. The kinematic representation of the bicycle model allows the immediate evaluation of the reference yaw rate, based on the vehicle velocity and the steering angle applied by the driver.

the linearized kinematic bicycle model of Fig. 6.13 allows to compute the reference yaw rate from the driver steering angle. Given a certain steering angle δ, the curve radius can be geometrically evaluated from the figure as

$$R = \frac{L}{\tan\delta} \approx \frac{L}{\delta} \tag{6.24}$$

where L is the vehicle wheelbase. Therefore, by substituting the (6.24) in (6.23), the yaw rate value for steady state condition can be computed at any instant from the steering angle, that constitutes the reference for the control strategies:

$$\psi^*_{dot} = \frac{V}{L}\delta \tag{6.25}$$

Moreover, it is evident that by inverting (6.24) it is possible to compute the theoretical steering angle necessary to cover a curve of radius R with a vehicle of length L. This consideration results particularly useful to analyse the effect of control strategies on driving ease, that will be discussed in § 6.3.2.

Control strategies comparison: disturbance rejection

In order to make the disturbance rejection evaluation more comprehensible, a simplified manoeuvre has been tested along the circuit schematically shown in Fig. 6.14. The manoeuvre consists of a single clockwise lap along the oval track at the constant velocity of $V = 5$ m/s, and the driver should maintain the vehicle in the middle of the lane (the dashed line of Fig. 6.14). At the half

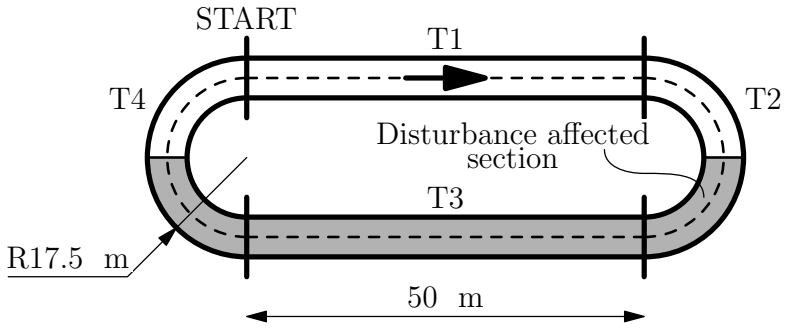

Figure 6.14: Test track. The driver has to maintain the vehicle on the middle of the lane (dashed line) at a constant velocity of $V = 5$ m/s. At the half of the first curve an external yaw-moment of amplitude $N_d = 10$ N m is added as disturbance, that is then taken off at the half of the second curve.

of the first curve, after about 15 seconds, an external step-like yaw-moment of amplitude $N_d = 10$ N m is added as a disturbance. The driver has then to drive in presence of such a disturbance as far as the middle of the second curve, after about 35 seconds, when the disturbance is taken off.

In the present case the velocity V is constant and the test track can be divided in 4 segments (the straights T1 and T3 and the curves T2 and T4) of constant radius ($R = \infty$ for T1-T3 and $R = 17.5\ m$ in segments T2-T4). This means that the theoretical yaw rate of the test track should have a square-wave profile, with amplitude $\psi_{dot,\mathrm{th}} = 5/17.5 = 0.286$ rad/s.

Figures 6.15-6.16-6.17 show the comparison between the theoretical yaw rate, computed with the (6.23), and the recorded yaw rate, respectively without control, with the DYC and the AFS control. In spite of the fact that $\psi_{dot,\mathrm{th}}$ is not the controllers' reference but just a comparison value, the efficiency of both DYC and AFS is absolutely evident. The yaw rate recorded for test without active control systems shows a continuous correction by the driver to keep the vehicle on the track and the disturbance effect (both when added and removed) is highlighted by yaw rate jumps (after about 15 and 35 seconds respectively). In presence of the controllers, the manoeuvres present instead smoother yaw rates, with profiles that are very similar to the theoretical one.

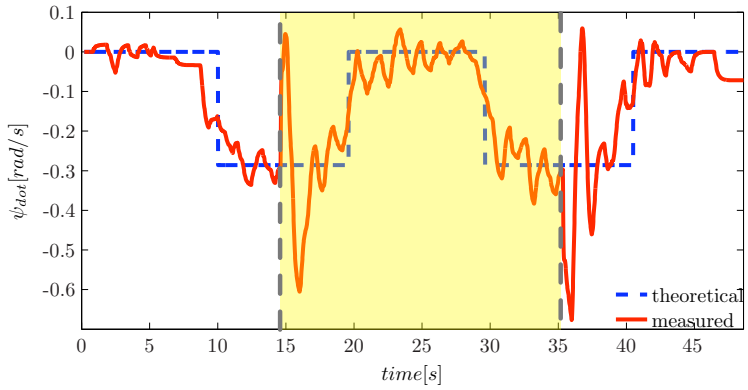

Figure 6.15: Comparison of theoretical and measured yaw rate profiles without control - The interval subject to the disturbance is highlighted.

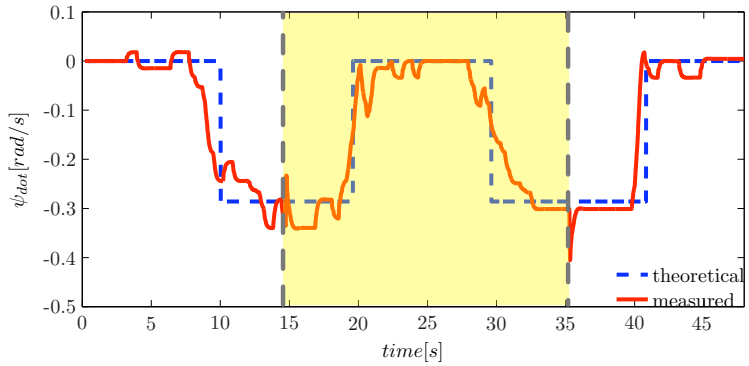

Figure 6.16: Comparison of theoretical and measured yaw rate profiles with the Direct Yaw Control - The interval subject to the disturbance is highlighted.

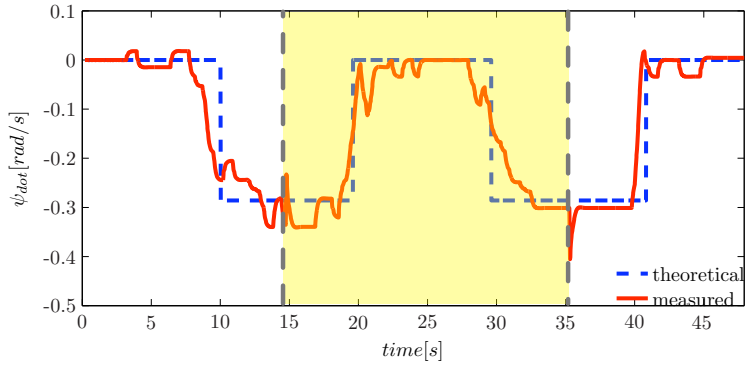

Figure 6.17: Comparison of theoretical and measured yaw rate profiles with the Active Front Steering control - The interval subject to the disturbance is highlighted.

A quantitative evaluation of the controllers efficiency can be instead done by observing Figures 6.18-6.19-6.20. The graphs show

- the comparison between the reference yaw rate, computed with (6.25) and the measured one (top plot),
- the yaw rate error (centre plot),
- and the driver steering angle (bottom plot)

obtained, respectively, without the control, with Direct Yaw Control and with the Active Front Steering control.

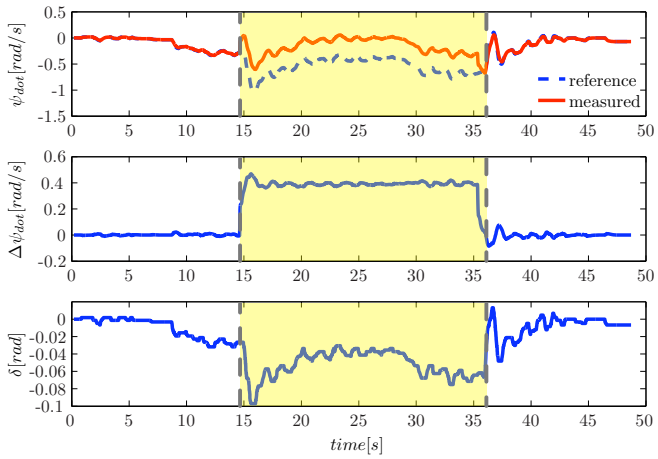

Figure 6.18: Yaw rate profiles (*top*), yaw rate error (*centre*) and driver steering angle (*bottom*) without control - The interval subject to the disturbance is highlighted.

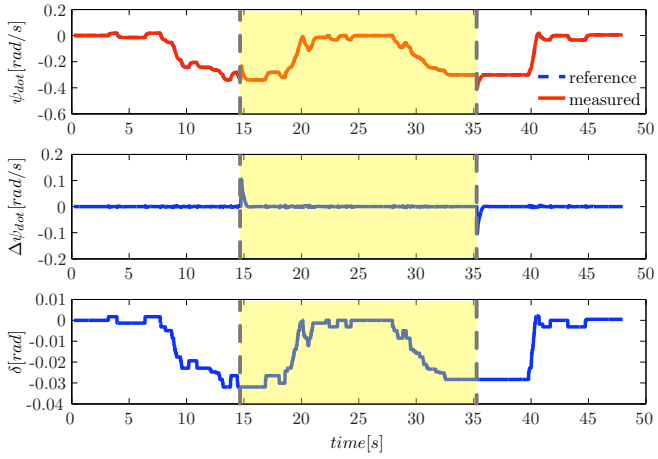

Figure 6.19: Yaw rate profiles (*top*), yaw rate error (*centre*) and driver steering angle (*bottom*) with the Direct Yaw Control - The interval subject to the disturbance is highlighted.

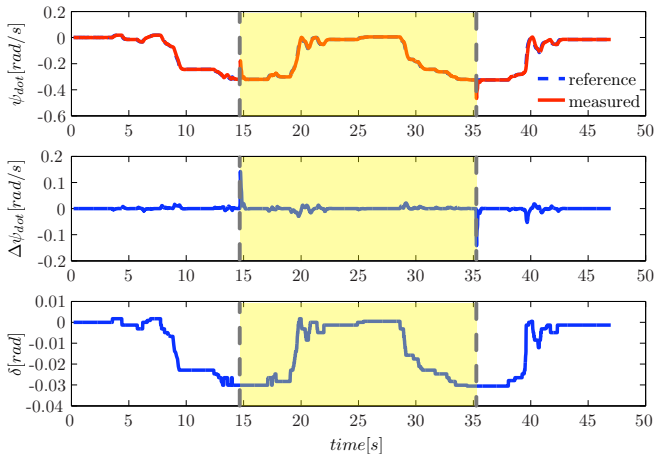

Figure 6.20: Yaw rate profiles (*top*), yaw rate error (*centre*) and driver steering angle (*bottom*) with the Active Front Steering control - The interval subject to the disturbance is highlighted.

The first observation is about the profiles obtained while driving without controllers (Fig. 6.18). Since the disturbance introduces an undesired yaw rate, the driver is forced to counter steering, as shown in bottom plot, in order to maintain the desired attitude. Nevertheless the reference value of the yaw rate is computed from the steering angle, and this introduces the error evident in the central part of the manoeuvre (centre plot). This problem is instead efficiently compensated by both the controllers, as shown in Fig. 6.19 and Fig. 6.20. The good matching between the reference and measured yaw rate profiles is clear, with very small errors. Moreover the yaw rate profiles (top plots) assume shapes absolutely similar to those of the respective steering angle (bottom plots). This means that the yaw rate assumes the nominal behaviour described by (6.25), *i.e.* the yaw rate equals the driver steering angle times the constant scaling factor V/L.
Another interesting comment can be done by observing the steering angle profiles when the disturbance is taken off (after about 35 seconds): a strong counter-steering can be seen when driving without control, that is not present when the controllers are active. Such a phenomenon is due to the fact that, in absence of the controllers, the driver experiences a strong increase of the yaw rate at the instant the disturbance is removed, feeling the need of counter-

steering in order to follow the reference path. Nevertheless tests carried out with several drivers has demonstrated that the driver reaction is almost always too strong, involving then a sequence of corrections that yields a discontinuous yaw rate profile. This particular effect is instead absent in presence of either the DYC or the AFS control, thanks to the fact that the disturbance compensation is not perceived by the driver. In general terms, it can then be said that the control strategies give comparable results in terms of yaw rate: both the architectures force the system to the nominal behaviour, compensating the undesired disturbances and making the driving easier (less correction necessary by the driver).

In Fig. 6.21 the trajectories recorded during the tests are compared: the external thin lines represent the track boundaries. Even if a too internal trajectory is maintained in the first curve in all the cases, the advantages introduced by the control strategies are evident. Either with the DYC or the AFS control, the trajectories do not show all the correction that are present instead when the controllers are off. This effect is particularly evident in the second curve, when the disturbance is removed and, in absence of assistance, the driver counter-steers for the reasons above discussed. In general terms it can be then said that the architectures give comparable advantages in terms

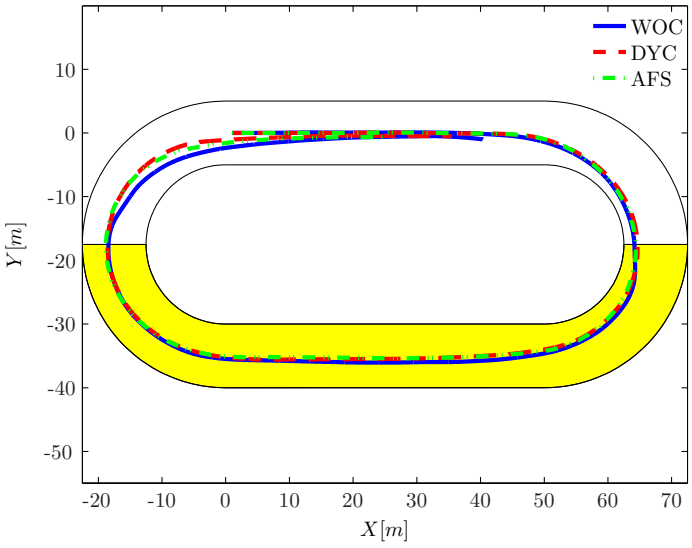

Figure 6.21: Trajectories comparison - The interval subject to the disturbance is highlighted.

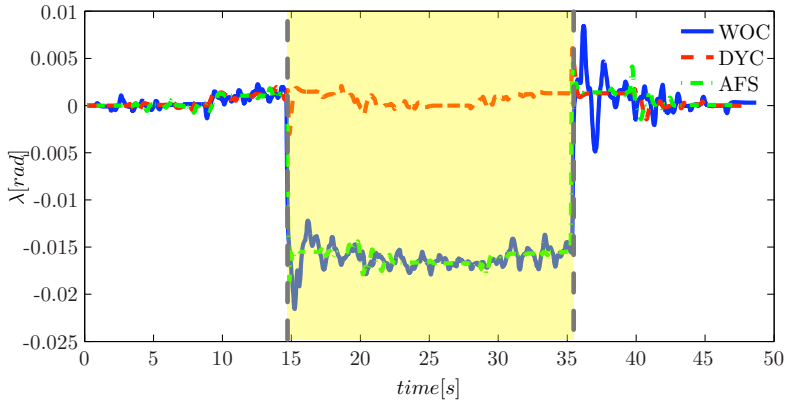

Figure 6.22: Sideslip angle profiles - The interval subject to the disturbance is highlighted.

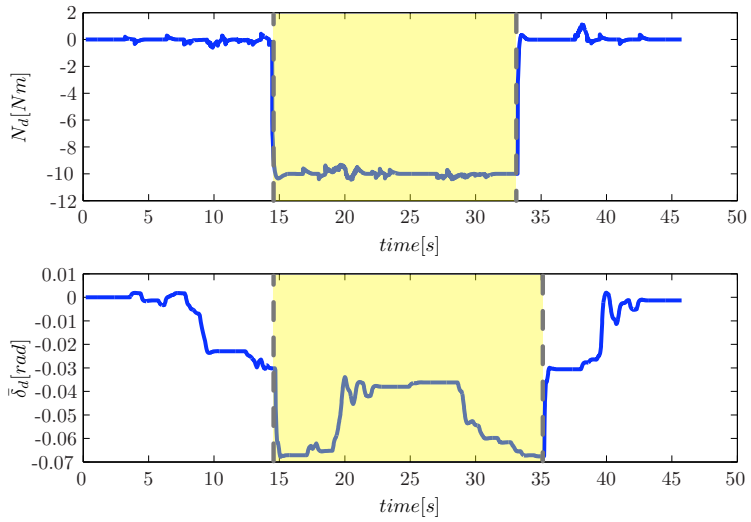

Figure 6.23: Corrections profiles - DYC yaw moment N_z (*top*) and AFS steering angle δ (*bottom*) - The interval subject to the disturbance is highlighted.

of trajectory.

Fig. 6.22 compares instead the vehicle sideslip angles during the tests. It is evident that the Direct Yaw Control presents the best behaviour in terms of

this variable, and the result is not surprising. Thanks to the direct application of a yaw moment, the DYC forces the vehicle to maintain the right attitude during the whole motion. In the two other cases, the disturbance compensation (by the driver or the controller) is instead achieved by (counter-)steering, affecting then the vehicle orientation: such a misalignment involves thus the presence of a sideslip angle when the disturbance is active.

Finally, Fig. 6.23 shows the corrections applied by the controllers. More precisely, the top plot represents the yaw-moment correction N_z introduced by the Direct Yaw Control, while the bottom one shows the steering angle δ applied by the Active Front Steering: the difference between the strategies is particularly evident from such a graph. Because of the fact that the DYC directly acts on the yaw dynamics by means of the yaw-moment N_z, the compensation of non-linearity is nearly imperceptible and the correction profile appears like that of the disturbance. This is not true for the AFS: by acting on the steering angle, the controller is forced to compensate even the large non-linearities, that are proper of the vehicle dynamics and comparable in magnitude to the introduced linear disturbance.

Control strategies comparison: driving ease

In order to evaluate the effect of controllers on driving ease, another simplified manoeuvre is defined, on the track shown in Fig. 6.24. The curve is covered at a constant velocity $V = 10\ m/s$ and the driver should maintain the vehicle in the middle of the lane. Nevertheless, in this case no disturbances are added, in order to focus the analysis on driving ease.

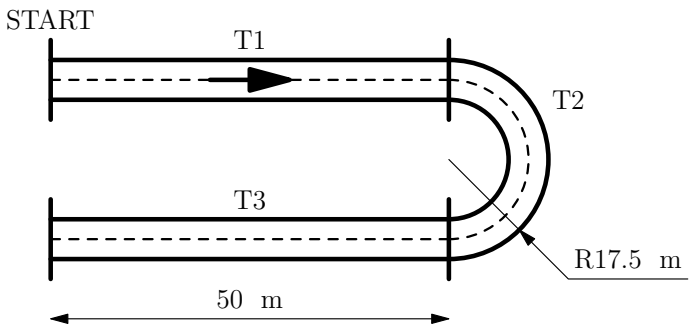

Figure 6.24: Test track for the analysis of the effect of controllers on driving ease. The curve is covered at a constant velocity $V = 10\ m/s$ and no external disturbances are added, in order to focus the analysis on the effect of controllers on driving ease.

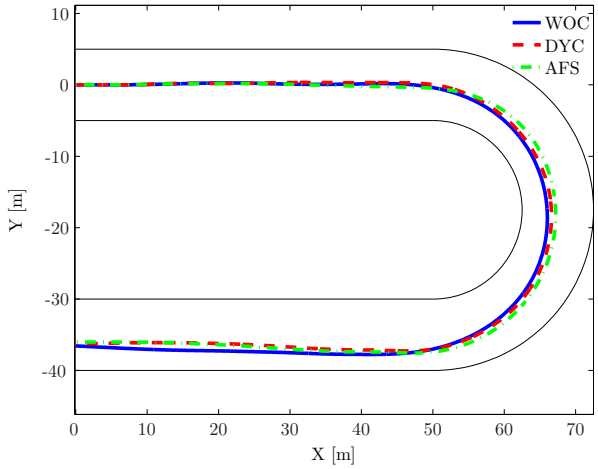

Figure 6.25: Driving ease - Typical trajectories.

Fig. 6.25 shows the typical trajectory profiles recorded during the test, respectively, without control, with DYC and AFS. The effect of active systems is not particularly evident from such variables, even if small corrections can be seen during curve exit when the controllers are taken off.

More interesting comments can instead be done by observing Figures 6.26-6.27-6.28, that show the typical driver steering angle profiles, compared to the theoretical one computed by inverting (6.24). Such plots clearly show the beneficial effect of either DYC or AFS strategies, since the number and the amplitude of the driver's correction on the steering angle are strongly decreased when the controllers are active.

A long simulation campaign has also allowed a quantitative evaluation of the effect of the controllers on the driving ease. In particular, the drivers's corrections have been evaluated as the absolute value of the difference between the actual and the theoretical steering angle:

$$\epsilon_\delta = |\delta - \delta_{th}| \tag{6.26}$$

Tab. 6.1 collects the average values μ and the standard deviations σ of such corrections recorded during the tests: the beneficial effect of the controller is evident. In particular, the introduction of either the DYC or the AFS controllers yields a reduction of about the 53 % of the average values of the corrections, meaning that the driver's task of path following is extremely facilitated. A reduction is evident also on the corrections' standard deviations,

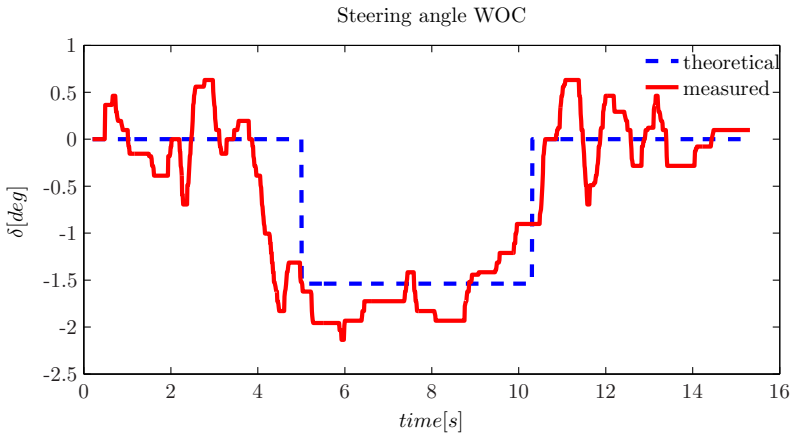

Figure 6.26: Driving ease - Typical steering angle profile without control.

even if smaller w.r.t. the averages' one: such a stochastic variable depends, in fact, mainly on the driver ability, that is not improved by the the controllers.

	$\mu_{\Delta\delta}$ $[deg]$	$\sigma_{\Delta\delta}$ $[deg]$
WOC	0.21	0.36
DYC	0.10	0.32
AFS	0.10	0.28

Table 6.1: Average values and standard deviation of the correction applied by the driver.

Resuming, the simulation campaign has highlighted the beneficial effects of both the control strategies on disturbance rejection and driving ease. The Direct Yaw Control presents better effects on some other variable (*e.g.* the sideslip angle), which are yet in contrast with the advantages of the Active Front Steering discussed in § 6.1. Moreover both the strategies make the remote drive easier, strongly reducing the need of corrections from the driver.

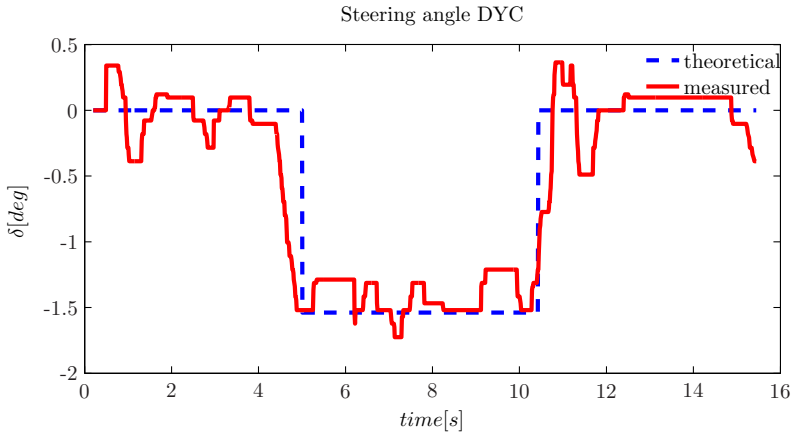

Figure 6.27: Driving ease - Typical steering angle profile with the Direct Yaw Control.

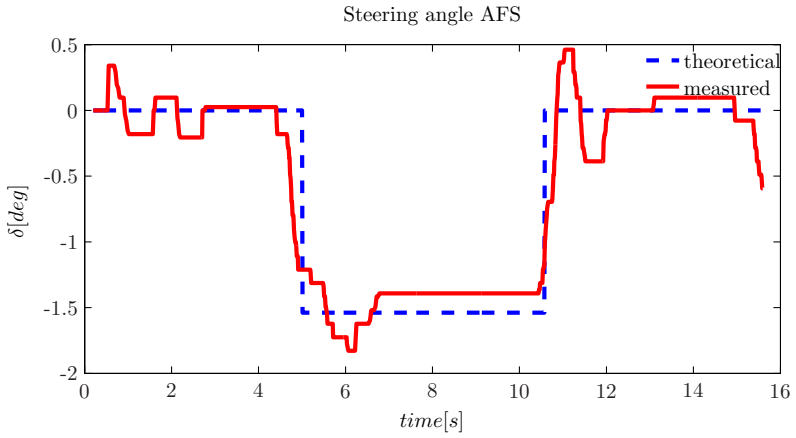

Figure 6.28: Driving ease - Typical steering angle profile with the Active Front Steering control.

Chapter 7

Conclusions

7.1 Summary Conclusion

The researches carried on in the last years by the members of the Mechatronics Research Group on autonomous driving have disclosed the need of an experimental platform to test path planning, state estimation and control algorithms. For this reason in 2006 the Reduced-size UnManned Buggy (RUMBy) Project is started, aiming at develop such a kind of test platform. The primary objective of this thesis has been then coping with the problems proper to the design of an experimental vehicle able to perform autonomous manoeuvres and/or to be remotely driven.

The work started from the definition of the system requirements, both in terms of hardware and software architectures. Because of economical constraints and hardware requirements, in regard of the vehicle the choice has fallen on a radio-controlled, 1:6 scale model (about 680 mm long and 510 mm wide) equipped with a 26 cm^3 two-strokes engine. Moreover, due to the limited load capacity of the vehicle, only the sensing and the sensor fusion instrumentation have been on-board installed, while the heavy and energy-consuming computer needed for the control and actuation is instead remotely connected to the vehicle via radio communication channels. These choices constitutes a key point of the research for several reasons. Firstly this represents a novelty element, since all the autonomous driving projects present in literature employ common vehicles (cars and even trucks) and middle/large investments. Moreover, the vehicle reduced-size has forced the use of compact and low power consumption systems, that could be directly installed on actual cars (at least regarding the sensing part). At the same time, the

software framework design has constituted a challenging activity, since radio-communication is involved and because modularity and safety requirements were enforced. These constraints have compelled to the drawing of a purpose-made radio-communication loop (comprising the vehicle radio-controls and a UDP protocol for the transmission of the sensor signals), and to the choice of a Manager Unit state-machine architecture.

Some models describing the behaviour of the vehicle and of its subsystems are proposed. Mathematical representations are powerful tools for both behaviour prediction, state estimation and control synthesis. Attention has been paid to the modelling of tyres, that constitute crucial elements of cars, and to different multibody descriptions of the vehicle itself, focusing on the effect of introducing simplifications. Furthermore, whereas mathematical models always contain system characteristic parameters, the problems of system identification and model validation are discussed. Identification aims at evaluating the parameters of a system, while validation centres on the evaluation of models representativeness. Two ways are available for parameters identification -measurement and estimation- that have been analysed and discussed in detail, presenting some experimental results. Validation has been instead carried on with a novel approach: despite the common method in mechanical systems validation dealt only with time domain, both time and frequency domain responses have been verified, with qualitative and quantitative methods.

Additionally, the efficiency of the state estimation architecture generated for RUMBy is discussed. Control of a dynamic system requires reliable knowledge of the system state, which besides is not always measurable/observable. Consequently the state must be estimated from the measurable quantities onboard acquired. A modular architecture has been proposed, coupling preprocessing and sensor fusion algorithms: preprocessing aims at making measures suitable for sensor fusion, that yields the out-and-out state estimation. The modularity shown strong advantages thanks to its flexibility: different state estimator can be combined with the same preprocessing algorithm, depending on adopted measures and interesting states.

Finally, the problem of the yaw rate control has been addressed. Two control strategies are proposed: the Direct Yaw-moment Control (DYC) and the Active Front Steering (AFS) control. Both the strategies present a disturbance observer architecture and their design is based on the same linearized model, but differ on the control input: the DYC generates the corrective yaw-moment by means of a differential torque (generation of different torques at right and left wheels), while the AFS acts on the steering angle. Because of the fact that

independent wheel braking/driving is not available on RUMBy, the strategies have been compared by means of a simulation campaign. A static simulator is proposed, that allows for reproduce the driving of RUMBy in a virtual environment. The comparison has highlighted advantages and disadvantages of each control architecture: both the strategies have anyway demonstrated beneficial effects in driver assistance, improving vehicle manoeuvrability and making the driving safer and easier.

7.2 Further Work

As it often happens in research, the results presented in this thesis can only mark a milestone within a work in progress. In spite of the efforts done to thoroughly treat each problem, some details have been of course neglected or studied not in details. Moreover the same nature of the work, *i.e.* the development of a test platform, opens the doors to a wide range of analyses and experimental activities. Consequently it is difficult to identify which aspects could mainly give rise to future works.

In regard of the vehicle itself, hardware and software reviews are not to be excluded. For instance, the continuous availability of new electronic devices could suggest to re-designing the whole system architecture or part of it. Furthermore it could become interesting to measure further vehicle states and variables (*e.g.* engine revs per minute or struts extension), disclosing thus the need of equipping the vehicle with additional sensors and re-designing hardware and software interfaces.

At the present time, the modelling activity does not highlight particular needs of extension. Substantial room for improvement are instead evident for vehicle identification and validation. The same activities presented about identification and validation of Kanon roll motion could be either applied to RUMBy or extended to the whole vehicle dynamics and to its subsystems. By studying the time and frequency responses of a larger set of degrees of freedom, more efficient identifications can be achieved, yielding models more and more representative. In addition, since some vehicle parameters change during a manoeuvre, the on-line identification by means of recursive algorithms could represent an interesting investigation field.

Also the state estimation presents large improvement margins. In the present work a version of the Extended Kalman Filter (EKF) has been discussed for the state estimation. Nevertheless, the large set of on-board sensors makes that the measures can be combined in different manners so that to cre-

ate various sensor fusion algorithm version. It could be besides interesting to apply state estimation algorithms different from the EKF, like fuzzy logics, neural networks or other observers.

Finally, the dynamics control is doubtless the widest subject of further works, properly due to the reasons that have brought to start the project. In the present work just a couple of yaw rate control architectures based on disturbance observer have been proposed. The proposed controls are building blocks for autonomous manoeuvre execution and/or remote driving assistance. Consequently, further steps in control topic could be the development of longitudinal dynamics control strategies, the test of longitudinal and lateral dynamics controller performances in reference manoeuvre tracking (*e.g.* in terms of longitudinal velocity and yaw rate) and the test of overall performances of a system that on-line re-plans the reference manoeuvre (*e.g.* the Optimal Manoeuvre Method), which is tracked by the above "low level" controllers.

Appendix A

List of Symbols

δ : steering angle

θ : pitch angle

κ : longitudinal slip ratio

λ : sideslip angle

ϕ : roll angle

ψ : yaw angle

ω : wheel spinning velocity

σ_i : theoretical slip in i-th direction

σ_{eq} : theoretical slip magnitude

k_κ : driving stiffness

k_λ : cornering stiffness

l_{ij} : ij-th strut extension

l_i : tyre relaxation length in i-th direction

F_{ij}^0 : generic force model

F_x : longitudinal forces acting at tyre-ground contact point in steered frame

F_y : lateral forces acting at tyre-ground contact point in steered frame

S : longitudinal forces acting at tyre-ground contact point in yawed frame

F : lateral forces acting at tyre-ground contact point in yawed frame

F_{aero} : drag force

N : normal loads acting at tyre-ground contact point

T : driving/braking torques acting at the wheels

M : vehicle total mass

M_s : sprung mass

m_u : generic unsprung mass

I_i : moment of inertia in i-th direction

I_{Wi} : i-th wheel moment of inertia about spin axis

$l_{r,f}$: x-distance between the CoM and rear/front wheel

L : vehicle wheelbase

$t_{r,f}$: rear/front trackwidth

R : nominal tyre radius

h_{rc} : distance between the vehicle CoM and rolling centre along z-axis

h_D : z-distance between the CoM and the drag force point of application

k_D : vehicle drag coefficient

u : longitudinal velocity

v : lateral velocity

v_S : contact point absolute velocity

w : vertical velocity

X : CoM x-position w.r.t. an inertial frame

Y : CoM y-position w.r.t. an inertial frame

Z : CoM z-position w.r.t. an inertial frame

Appendix B

Parameter Estimation by means of Recursive Least Squares

In order to adapt the vehicle model to the current conditions and, should the occasion arise, to design adaptive controllers, changing parameters must be identified online. Whilst with non-recursive methods the estimated parameter is only available at the end of the measurement time, with dynamic parameters it is the changing parameter values after each sampling instant which are of interest. In order to prevent the saving of all past measurement values, and thus save computation time, the recursive method is used for online identification.

For the recursive least squares (RLS) the following equations apply:

$$\boldsymbol{P}(k) = \left[\boldsymbol{\Psi}^T(k) \cdot \boldsymbol{\Psi}(k)\right]^{-1} \tag{B.1}$$

$$\begin{aligned} \boldsymbol{\zeta}(k) &= \boldsymbol{P}(k+1) \cdot \boldsymbol{\Psi}(k+1) \\ &= \frac{\boldsymbol{P}(k) \cdot \boldsymbol{\Psi}(k+1)}{\boldsymbol{\Psi}^T(k+1)\boldsymbol{P}(k) \cdot \boldsymbol{\Psi}(k+1) + 1} \end{aligned} \tag{B.2}$$

$$\hat{\boldsymbol{\Theta}}(k+1) = \hat{\boldsymbol{\Theta}}(k) + \boldsymbol{\zeta}(k) \cdot \left[y(k+1) - \boldsymbol{\Psi}^T(k+1) \cdot \hat{\boldsymbol{\Theta}}(k)\right] \tag{B.3}$$

$$\boldsymbol{P}(k+1) = \boldsymbol{P}(k) - \boldsymbol{\zeta}(k) \cdot \boldsymbol{\Psi}^T(k+1) \cdot \boldsymbol{P}(k) \tag{B.4}$$

The basic equation of RLS estimator represent a versatile tool for online parameter identification. Further related RLS-estimators can be developed from these equation, such as RLS with weighted memory, generalized RLS, extended RLS etc.

Via the introduction of a forgetting factor λ, which increases the elements in the covariance matrix $\boldsymbol{P}(k)$ for each iteration and thus weights the new

data higher than the older data, one is able to slowly *forget* past values. This overcomes the consistency property of least squares estimator for time variant parameters. λ should not be chosen too small, or the influence of disturbances may not be satisfactorily removed. Good results have been obtained with values of $0.95 < \lambda < 0.995$. Because a large part of the identification with RLS method is carried out with exponentially decaying memory, the corresponding equations are given.

$$\boldsymbol{\zeta}(k) = \frac{\boldsymbol{P}(k) \cdot \boldsymbol{\Psi}(k+1)}{\boldsymbol{\Psi}^T(k+1)\boldsymbol{P}(k) \cdot \boldsymbol{\Psi}(k+1) + \lambda} \tag{B.5}$$

$$\hat{\boldsymbol{\Theta}}(k+1) = \hat{\boldsymbol{\Theta}}(k) + \boldsymbol{\zeta}(k) \cdot \Big[y(k+1) - \boldsymbol{\Psi}^T(k+1) \cdot \hat{\boldsymbol{\Theta}}(k) \Big] \tag{B.6}$$

$$\boldsymbol{P}(k+1) = \big[\boldsymbol{I} - \boldsymbol{\zeta}(k) \cdot \boldsymbol{\Psi}^T(k+1) \big] \cdot \boldsymbol{P}(k) \frac{1}{\lambda} \tag{B.7}$$

Appendix C

Simplified refined instrumental-variable method for continuous-time systems identification

Consider a lumped-parameter, linear, time-invariant (LTI) continuous-time model with a single input and a single output (SISO), whose input-output dynamics is represented by the following transfer function:

$$G(s) = \frac{Y(s)}{U(s)} = \frac{b_m s^m + b_{m-1} s^{m-1} + \cdots + b_1 s + b_0}{a_n s^n + a_{n-1} s^{n-1} + \cdots + a_1 s + a_0}$$

Denote respectively with $B(s, \boldsymbol{\theta})$ and $A(s, \boldsymbol{\theta})$ the numerator and denominator of $G(s)$, both depending on the vector $\boldsymbol{\theta}$ of the unknown model coefficients; by assuming (without loss of generality) that $G(s)$ is normalized so that its denominator has a unitary constant term, i.e. $a_0 = 1$, the vector of unknown coefficients is $\boldsymbol{\theta} = [a_n, \ldots, a_1, b_m, \ldots, b_0]^T$.

Suppose that the input and output variables $u(t)$ and $y(t)$ are measured at the discrete times t_k, $k = 1, \ldots, t_N$, and denote with $u(t_k)$ and $y(t_k)$ their sampled measurements: then, the continuous-time system identification problem consists of finding an estimate $\hat{\boldsymbol{\theta}}$ of the actual value of $\boldsymbol{\theta}$ by using the input-output data record $Z^N := \{u(t_k), y(t_k)\}_{k=1,\ldots,N}$. The estimate $\hat{\boldsymbol{\theta}}$ can be determined by minimizing, in a least-square sense, the *output error* (modeling error) $\epsilon(t) := y(t) - x(t)$, namely the mismatch between the response $x(t)$ predicted by the model and the measured response $y(t)$. In order to recast the minimization problem as an ordinary (i.e. linear) least-square problem,

the following set of *state-variable filters* (SVFs) is introduced:

$$F_i(s,\boldsymbol{\theta}) := \frac{s^i}{A(s,\boldsymbol{\theta})}, \quad i = 0,\ldots,n \tag{C.1}$$

Taking the Laplace transform of the output error yields:

$$\epsilon(s) = Y(s) - \frac{B(s,\boldsymbol{\theta})}{A(s,\boldsymbol{\theta})}\,U(s)$$

By using the definitions of the SVFs, the Laplace transform $\epsilon(s)$ can be rewritten as follows:

$$\epsilon(s) = A(s,\boldsymbol{\theta})\,F_0(s,\boldsymbol{\theta})\,Y(s) - B(s,\boldsymbol{\theta})\,F_0(s,\boldsymbol{\theta})\,U(s) \tag{C.2}$$

$$= \sum_{i=0}^{n} a_i\,s^i F_0(s,\boldsymbol{\theta})\,Y(s) - \sum_{i=0}^{m} b_i\,s^i F_0(s,\boldsymbol{\theta})\,U(s) \tag{C.3}$$

$$= \sum_{i=0}^{n} a_i\,F_i(s,\boldsymbol{\theta})\,Y(s) - \sum_{i=0}^{m} b_i\,F_i(s,\boldsymbol{\theta})\,U(s) \tag{C.4}$$

$$= \sum_{i=0}^{n} a_i\,Y_{i,f}(s) - \sum_{i=0}^{m} b_i\,U_{i,f}(s) \tag{C.5}$$

where $Y_{i,f}(s) := F_i(s,\boldsymbol{\theta})Y(s)$ and $U_{i,f}(s) := F_i(s,\boldsymbol{\theta})U(s)$ are the filtered versions of the input and output variables. Back in time-domain, the output error becomes:

$$\epsilon(t) = \sum_{i=0}^{n} a_i\,y_{i,f}(t) - \sum_{i=0}^{m} b_i\,u_{i,f}(s) = y_{0,f}(t) - \boldsymbol{\varphi}_f^T(t)\,\boldsymbol{\theta} \tag{C.6}$$

where $\boldsymbol{\varphi}_f(t) = [-y_{n,f}(t),\,\ldots,\,-y_{1,f}(t), u_{m,f}(t),\,\ldots,\,u_{0,f}(t)]^T$.

The least-square (LS) estimate $\hat{\boldsymbol{\theta}}_{LS}$ of $\boldsymbol{\theta}$ is determined by minimizing the sum of the squares of the residuals $\epsilon(t_k)$, $k = 1,\cdots,N$, i.e.:

$$\hat{\boldsymbol{\theta}}_{LS} := \underset{\boldsymbol{\theta}}{\operatorname{argmin}} \sum_{k=1}^{N} \epsilon^2(t_k) = \underset{\boldsymbol{\theta}}{\operatorname{argmin}} \sum_{k=1}^{N} \left[y_{0,f}(t_k) - \boldsymbol{\varphi}_f^T(t_k)\,\boldsymbol{\theta}\right]^2 \tag{C.7}$$

or, in compact form:

$$\hat{\boldsymbol{\theta}}_{LS} := \underset{\boldsymbol{\theta}}{\operatorname{argmin}} \|\boldsymbol{\Gamma} - \boldsymbol{\Phi}\boldsymbol{\theta}\|^2 = (\boldsymbol{\Gamma} - \boldsymbol{\Phi}\boldsymbol{\theta})^T(\boldsymbol{\Gamma} - \boldsymbol{\Phi}\boldsymbol{\theta}) \tag{C.8}$$

with:

$$\boldsymbol{\Gamma} := [y_{0,f}(t_1),\, \ldots,\, y_{0,f}(t_N)]^T \tag{C.9}$$

$$\boldsymbol{\Phi} := [\boldsymbol{\varphi}_f(t_1),\, \ldots,\, \boldsymbol{\varphi}_f(t_N)]^T \tag{C.10}$$

This is a standard linear least-square problem, whose solution can be computed analytically as follows:

$$\hat{\boldsymbol{\theta}}_{LS} \;=\; \left(\boldsymbol{\Phi}^T\boldsymbol{\Phi}\right)^{-1}\boldsymbol{\Phi}^T\boldsymbol{\Gamma} \tag{C.11}$$

Although a solution to the estimation problem is apparently provided, there are two issues with the procedure described above that undermine the attainment of a consistent estimate. Firstly, the definition of the SVFs given in (C.1) depends on $A(s,\boldsymbol{\theta})$, which is not known a priori; secondly, the LS estimate is asymptotically biased whenever the measurement noise is not white **?**. In order to overcome these two issues, an iterative procedure based on the *instrumental variable* (IV) method is introduced. Its structure consists of the following steps:

1. (*Initialization*) Choose an initial estimate $A_0(s)$ of the denominator $A(s,\boldsymbol{\theta})$, which is required to form a first set of SVFs. The typical choice is:

   $$A_0(s) = (s+\lambda)^n \tag{C.12}$$

   where $\lambda > 0$ is a constant larger than the system bandwidth.

2. (*LS step*) Define the filters $F_i(s)$, $i = 0, \ldots, n$ as specified in (C.1), by using the initial estimate $A_0(s)$ defined in previous step; use them to construct the matrices $\boldsymbol{\Gamma}$ and $\boldsymbol{\Phi}$, and get the LS estimate:

   $$\hat{\boldsymbol{\theta}}_{LS} \;=\; \left(\boldsymbol{\Phi}^T\boldsymbol{\Phi}\right)^{-1}\boldsymbol{\Phi}^T\boldsymbol{\Gamma} \tag{C.13}$$

   Set $\hat{\boldsymbol{\theta}}_1 = \hat{\boldsymbol{\theta}}_{LS}$ and $k = 1$.

3. (*IV step*) Increase k by 1; then, construct the following vector of regressors (called *instruments*):

   $$\boldsymbol{\psi}_f(t) = [-\hat{y}_{n,f}(t),\, \ldots,\, -\hat{y}_{1,f}(t), u_{m,f}(t),\, \ldots,\, u_{0,f}(t)]^T \tag{C.14}$$

where the regressors $\hat{y}_{l,f}(t)$, $l = 1, \ldots, n$ are obtained by filtering, using the filters $F_l(s, \hat{\boldsymbol{\theta}}_{k-1})$, the output $\hat{y}(t)$ of the noise-free model:

$$\hat{Y}(s) = \frac{B(s, \hat{\boldsymbol{\theta}}_{k-1})}{A(s, \hat{\boldsymbol{\theta}}_{k-1})} U(s) \tag{C.15}$$

The new vector of regressors can be used to compute a consistent estimate of $\boldsymbol{\theta}$, called *instrumental-variable* (IV) estimate:

$$\hat{\boldsymbol{\theta}}_{IV} \;=\; \left(\boldsymbol{\Psi}^T \boldsymbol{\Phi}\right)^{-1} \boldsymbol{\Psi}^T \boldsymbol{\Gamma} \tag{C.16}$$

where:

$$\boldsymbol{\Psi} := [\boldsymbol{\psi}_f(t_1), \ldots, \boldsymbol{\psi}_f(t_N)]^T \tag{C.17}$$

Set $\hat{\boldsymbol{\theta}}_k = \hat{\boldsymbol{\theta}}_{IV}$; repeat the IV-step until the iteration converges (typically, until the improvements in the loss function (C.7) become negligible).

Appendix D

Auto-correlation and Cross-correlation

A quantitative method for the validation of a model consists of the residual analysis. Residuals $\epsilon(t)$ are differences between the predicted output from the model $\hat{y}(t)$ and the measured output $y(t)$ from the validation data set. In particular, two tests have to be done on the residuals: "independence test" and "whiteness test". The independence test demonstrates if the residual error $\epsilon(t)$ is uncorrelated with $u(t)$ (*i.e.* if the model is capable of reproducing the whole portion of the output $y(t)$ affected by the input $u(t)$) and is carried out by computing the cross-correlation between $\epsilon(t)$ and $u(t)$. The whiteness test shows instead if the model provides a correct prediction of the equivalent disturbance affecting the output measurements, hence the residual error should be a white noise: this is verified by studying the auto-correlation of the residual $\epsilon(t)$.

Generally speaking, the correlation $\rho_{X,Y}$ can be thought as a normalized measure of covariance, and constitutes a dimensionless index of the similarity between two random variables X and Y:

$$\rho_{X,Y} = \frac{\mathrm{cov}(X,Y)}{\sigma_X \sigma_Y} = \frac{E[(X-\mu_X)(Y-\mu_Y)]}{\sigma_X \sigma_Y} \tag{D.1}$$

where μ indicates the average value of a variable and σ is its standard deviation, "E" is the expected value operator and "cov" means covariance. Note that this expression is not well-defined for all processes, because the variance may be zero (for a constant process) or infinite. If the function is well-defined, its value must lie in the range [-1, 1], with 1 indicating perfect correlation and -1 indicating perfect anti-correlation.

Going back to the residual analysis, the independence test consists then of compute the cross-correlation between the residuals $\epsilon(k)$ and the input

$u(k)$ measured at the generic sample time k. Therefore (D.1) becomes the following:

$$\rho_{\epsilon,u} = \frac{E[(\epsilon_k - \mu_\epsilon)(u_k - \mu_u)]}{\sigma_\epsilon \sigma_u} \tag{D.2}$$

and indicates, at any time, if the model captures the whole dynamics of the system. On the contrary, the whiteness test is done by computing the residuals auto-correlation. Auto-correlation describes the correlation between values of the same variable (in this case, the residual ϵ) at different instants, as a function of the two times. Let t_1 and t_2 be two generic points in time, the auto-correlation of the residuals between any these times is

$$\rho_\epsilon(t_1, t_2) = \frac{E[(\epsilon_{t_1} - \mu_{t_1})(\epsilon_{t_1} - \mu_{t_1})]}{\sigma_{t_1} \sigma_{t_2}} \tag{D.3}$$

This test allows then to determine if the model correctly predicts the disturbance affecting the outputs.

Bibliography

M. Abe. *Vehicle Handling Dynamics: Theory and Application*. Butterworth-Heinemann, 2009.

J. Ackermann, D. Odenthal, and T. Buente (1999). Advantages of active steering for vehicle dynamics control. In *Proc. 32nd International Symposium on Automotive Technology and Automation*, pages 263–270, Vienna, 1999. Citeseer.

J. Ackermann (1980). Parameter space design of robust control systems. *IEEE Transactions on Automatic Control*, 25(6):1058–1072, 1980.

J.S. Albus (2002). A reference model architecture for intelligent unmanned ground vehicles. In *Proceedings of the SPIE 16th Annual International Symposium on Aerospace/Defense Sensing, Simulation and Controls*, pages 303–310. Citeseer, 2002.

K. B. Arkan, Y. S. Ünlüsoy, İ. Korkmaz, and A. O. Çelebi (2008). Identification of linear handling models for road vehicles. *Vehicle System Dynamics: International Journal of Vehicle Mechanics and Mobility*, 46(7):621 – 645, 2008.

E. Bakker, L. Nyborg, and H.B. Pacejka (1987). Tire modeling for use in vehicle dynamics studies. *SAE Paper*, 1987.

R. Behringer, S. Sundareswaran, B. Gregory, R. Elsley, B. Addison, W. Guthmiller, R. Daily, and D. Bevly (2004). The DARPA grand challenge-development of an autonomous vehicle. In *IEEE Intelligent Vehicles Symposium, Parma Italy*, 2004.

J. Bengtsson (2001). *Adaptive Cruise Control and Driver Modelling*. PhD thesis, Lunds Tekniska hoegskola, Sweeden, 2001.

E. Bertolazzi, F. Biral, and M. Da Lio (2005). Symbolic-numeric indirect method for solving optimal control problems for large multibody systems - the time-optimal racing vehicle example. *Vehicle System Dynamics*, 13(2): 233–252, March 2005.

E. Bertolazzi, F. Biral, and M. Da Lio (2006). Symbolic-numeric efficient solution of optimal control problems for multibody systems. *Journal of Computational and Applied mathematics*, 185(2):404–421, January 2006.

E. Bertolazzi, F. Biral, and M. Da Lio (2007). Real-time motion planning for multibody systems. *Multibody System Dynamics*, 17(2):119–139, April 2007.

E. Bertolazzi, F. Biral, P. Bosetti, M. De Cecco, R. Oboe, and F. Zendri (2008). Development of a reduced size unmanned car. In *Advanced Motion Control, 2008. AMC '08. 10th IEEE International Workshop*, pages 763–770, Trento, Italy, March 2008a.

E. Bertolazzi, F. Biral, M. Da Lio, A. Saroldi, and F. Tango (2008). Supporting drivers in keeping safe speed and safe distance: the saspence subproject within the european framework program 6 integrating project prevent. In *Proc. 15th World Congress on Intelligent Transport Systems*, New York City (NY), USA, 2008b.

I. J. M. Besselink (2000). *Shimmy of Aircraft Main Landing Gears*. PhD thesis, Technische Universiteit Delft, September 2000.

O.M.J. Carsten and F.N. Tate (2005). Intelligent speed adaptation: accident savings and cost-benefit analysis. *Accident Analysis and Prevention*, 37(3): 407 – 416, 2005. ISSN 0001-4575. doi: DOI: 10.1016/j.aap.2004.02.007.

J. C. Dixon (1996). *Tires, Suspensions and Handling*. Society of Automotive Engineers Inc., Warrendale, PA, USA, 1996.

C. Doniselli, M. Gobbi, and G. Mastinu (2003). Measuring the inertia tensor of vehicles. In *The Dynamics of Vehicles on Roads and on Tracks: Proceedings of the 17th IAVSD Symposium Held in Lyngby, Denmark, August 20-24, 2001*, volume 37, pages 301–313. Taylor & Francis, 2003.

H. Dugoff, P. Francher, and L. Segel (1970). An analysis of tire traction properties and their inluence on vehicle dynamic performance. Technical Report 700377, Society of Automotive Engineers, 1970.

E. Frazzoli, M.A. Dahleh, and E. Feron (2000). Robust hybrid control for autonomous vehicle motion planning. In *Proceedings of the 39th IEEE Conference on Decision and Control*, volume 1, pages 821–826. Citeseer, 2000.

H. Fujimoto, T. Saito, A. Tsumasaka, and T. Noguchi (2004). Motion control and road condition estimation of electric vehicles with two in-wheel motors. In *Control Applications, 2004. Proceedings of the 2004 IEEE International Conference on*, volume 2, pages 1266–1271 Vol.2, Sept. 2004.

H. Garnier and W. Liuping (2008). *Identification of Continuous-time Models from Sampled Data*. Advances in Industrial Control . Springer-Verlag, London, 2008.

G.J. Heydinger, N.J. Durisek, D.A. Coovert, D.A. Guenther, and S.J. Novak (1995). The design of a vehicle inertia measurement facility. 1995.

Y. H. Hsu and J. C. Gerdes (2006). A feel for the road: A method to estimate tire parameters using steering torque. In *Proceedings of the Symposium on Advanced Vehicle Control (AVEC)*, 2006.

R. E. Kalman (1960). A new approach to linear filtering and prediction problems. *ASCE Journal of Basic Engineering, D*, 82(1):35–45, 1960. URL `http://ci.nii.ac.jp/naid/10019323334/en/`.

U. Kiencke and L. Nielsen (2000). Automotive control systems: for engine, driveline, and vehicle. *Measurement Science and Technology*, 11:1828, 2000.

TW Kim and J. Yuh (2004). Development of a real-time control architecture for a semi-autonomous underwater vehicle for intervention missions. *Control Engineering Practice*, 12(12):1521–1530, 2004.

E. Liebermann (2004). Safety and Performance Enhancement: the Bosch Electronic Stability Control(Esp). 2004.

L. Ljung (1999). *System Identification: Theory for the user - 2nd ed*. Prentice Hall, 1999.

H. B. Pacejka and H.S. Radt (1963). Analysis of the steady-state turning behavior of an automobile. In *Proceedings of the Symposium on Control of Vehicles*, London, 1963. Institute of Mechanical Engineers.

H. B. Pacejka (1958). Study of the lateral behaviour of an automobile moving upon a flat level road. Technical Report YC-857-F-23, Cornell Aeronautical Laboratory, 1958.

H. B. Pacejka (1996). The tyre as a vehicle component. In M. Apetaur, editor, *Proceedings of XXVI FISITA Congress*, Prague, 1996.

H. B. Pacejka (2005). *Tyre and Vehicle Dynamics*. Number ISBN-13: 980-0-7506-6918-4. Elsevier, Oxford, UK, 2nd edition, 2005.

G.R. Potts (2007). Methods and systems for measurement of tire rolling resistance, November 20 2007. US Patent App. 11/943,582.

T. Raste, R. Bauer, and P. E. Rieth (2008). Global chassis control: Challenges and benefits within the networked chassis. In *Proc. of FISITA 2008 World Automotive Congress*, Munich, September 2008. International Federation of Automotive Engineering Societies, Springer Automotive Media.

J. M. Roberts, E. S. Duff, and P. I. Corke (2002). Reactive navigation and opportunistic localization for autonomous underground mining vehicles. *Information Sciences*, 145(1-2):127 – 146, 2002. ISSN 0020-0255. doi: DOI: 10.1016/S0020-0255(02)00227-X.

M. Russo, R. Russo, and A. Volpe (2000). Car parameters identification by handling manoeuvres. *Vehicle System Dynamics: International Journal of Vehicle Mechanics and Mobility*, 34(6):423 – 436, 2000.

S. Sakai, H. Sado, and Y. Hori (1999). Motion control in an electric vehicle with four independently driven in-wheel motors. *Mechatronics, IEEE/ASME Transactions on*, 4(1):9–16, Mar 1999. ISSN 1941-014X. doi: 10.1109/3516.752079.

A. Saroldi (2008). Saspence final report. Technical report, European Framework Project 6, 2008.

AJC Schmeitz, IJM Besselink, J. De Hoogh, and H. Nijmeijer (2005). Extending the Magic Formula and SWIFT tyre models for inflation pressure changes. *VDI BERICHTE*, 1912:201, 2005.

G. Schmidt and F. Freyberg (1996). *Autonome Mobile Systeme*. Springer, 1996.

M. Schuster, P. Herold, M. Wallbrecher, and T. Thalhammer (2008). The new steering system of bmw - the integral active steering. synthesis of agility and souvereignty. In *Proc. of FISITA 2008 World Automotive Congress*, Munich, September 2008. International Federation of Automotive Engineering Societies, Springer Automotive Media.

R. Schwarz, W. Dick, T. Meissner, U. Pinschmidt, and F. Martin (2008). Dynamic steering and quattro with sport differential - two perfect partners for highest agility and active safety. In *Proc. of FISITA 2008 World Automotive Congress*, Munich, September 2008. International Federation of Automotive Engineering Societies, Springer Automotive Media.

T. Shim and C. Ghike (2007). Understanding the limitations of different vehicle models for roll dynamics studies. *Vehicle System Dynamics: International Journal of Vehicle Mechanics and Mobility*, 45(3):191 – 216, 2007.

A.L. Svenson, V.J. Gawron, and T. Brown (2005). Safety Evaluation of Lane Change Collision Avoidance Systems Using the National Advanced Driving Simulator. In *19th International Technical Conference on the Enhanced Safety of Vehicles, Washington, DC*. Citeseer, 2005.

g. J. Thaler and R. G. Brown (1960). *Analysis and design of feedback control systems*. McGraw-Hill Electrical and Electronic Engineering series. McGraw-Hill, 2nd edition, 1960.

S. Thrun, M. Montemerlo, H. Dahlkamp, D. Stavens, A. Aron, J. Diebel, P. Fong, J. Gale, M. Halpenny, G. Hoffmann, K. Lau, C. Oakley, M. Palatucci, V. Pratt, P. Stang, S. Strohband, C. Dupont, L.E. Jendrossek, C. Koelen, C. Markey, C. Rummel, J. van Niekerk, E. Jensen, P. Alessandrini, G. Bradski, B. Davies, S. Ettinger, A. Kaehler, A. Nefian, and P. Mahoney (2006). Stanley: The robot that won the darpa grand challenge. *Journal of Field Robotics*, 23(9):661–692, June 2006.

B. Touchton, T. Galluzzo, D. Kent, and C. Crane (2006). Perception and planning architecture for autonomous ground vehicles. *Computer*, 39(12): 40–47, 2006.

A. Vahidi and A. Eskandarian (2003). Research advances in intelligent collision avoidance and adaptive cruise control. *Intelligent Transportation Systems, IEEE Transactions on*, 4(3):143–153, Sept. 2003. ISSN 1524-9050.

J. Wang, L. Alexander, and R. Rajamani (2004). Friction estimation on highway vehicles using longitudinal measurements. *Journal of Dynamic Systems, Measurement, and Control*, 126(2):265–275, 2004. doi: 10.1115/1.1766028.

D. Wesemeier and R. Isermann (2008). Identification of vehicle parameters using stationary driving maneuvers. *Control Engineering Practice*, In Press, Corrected Proof:–, 2008. ISSN 0967-0661. doi: DOI: 10.1016/j.conengprac.2008.10.008.

P. W. A. Zegelaar (1998). *The dynamic response of tyres to brake torque variations and road uneveness*. PhD thesis, Technische Universiteit Delft, March 1998.

F. Zendri, F. Biral, R. Antonello, and H. Fujimoto (2010). Modelling, identification and validation of an electric vehicle for model-based control design. In *To be published on the Proc. of the Advanced Motion Control, 2010. AMC '10. 11th IEEE International Workshop*, Nagaoka, Japan, March 2010.